Visualization of Chiral Superconductivity in UPt3

Pablo Garcia-Campos

THÈSE

Pour obtenir le grade de

DOCTEUR DE L'UNIVERSITÉ GRENOBLE ALPES

Spécialité : Physique de la Matière Condensée et du Rayonnement

Arrêté ministériel : 25 mai 2016

Présentée par

Pablo GARCIA CAMPOS

Thèse dirigée par **Klaus HASSELBACH**, Université Grenoble Alpes

préparée au sein du **Laboratoire Institut Néel**
dans **l'École Doctorale Physique**

Visualisation de la Supraconductivité Chirale en UPt3

Visualization of Chiral Superconductivity in UPt3

Thèse soutenue publiquement le **20 décembre 2021**,
devant le jury composé de :

Madame BEENA KALISKY
Professeur associé, Bar-Ilan University, Rapporteure
Monsieur HERMANN SUDEROW
Professeur associé, Universidad Autónoma de Madrid, Rapporteur
Monsieur THIERRY KLEIN
Professeur des Universités, UNIVERSITE GRENOBLE ALPES, Examinateur
Monsieur MANUEL HOUZET
Ingénieur HDR, CEA CENTRE DE GRENOBLE, Examinateur
Monsieur YANN GALLAIS
Professeur des Universités, UNIVERSITE DE PARIS, Président

Remerciements/Acknowledgments

Le travail effectué pendant les 3 ans de ma thèse n'aurait pas été possible sans la contribution de certaines personnes ni sans le soutien des autres.

Tout d'abord je voudrais remercier les sources de financement pour les deux demi bourses de thèse: Fondation Nanoscience et GreQue. I'm thankful to Beena Kalisky and Hermann Suderow for taking part in my thesis jury, and being reporters of the work reflected in this manuscript. Je rémercie également Thierry Klein, Manuel Houzet et Yann Gallais d'avoir accepté de faire partie de ce jury.

Klaus mérite aussi un gros merci, il m'a donné la possibilité d'utiliser le microscope (son *microenfant*) et d'arriver aux résultats obtenus. Son expérience dans le domaine a été toujours de grande utilité dans le progrès des travaux, ainsi que la liberté qu'il m'a donné, ce qui m'a permit d'obtenir les résultats présentés dans la suite et arriver jusqu'a ici.

Même si je n'ai pas discuté avec des exthesard.e.s de Klaus, les ouvrier.e.s qu'on construit le microscope qui méritent aussi un petit mot dans les remerciements: Cecile Veauvy (premiers pas dans la microscopie SQUID), Voicu Dolocan (étude de Sr_2RuO_4 et UPt_3), Danny Hykel (développement du microscope et du software de mesure). En plus, des createurs du cryostat A. Benoit, M. Caussignac and S. Pujol, merci.

I must thank also Alexandra Elbakyan for the free and accessible knowledge that she shares with me and everyone. This manuscript would be half empty if it wasn't by her.

Je remercie énormément Thierry Crozes pour l'effectivité dans la construction et développement de scanning and shunted SQUIDs, sans lui cette thèse n'aurait pas avancé comment elle l'a fait. Merci aussi à Arnaud Barbier et Karl Schuster pour la *misse en pointe* des SQUIDs, et Johannes Goupi pour la découpure des chips. I'm also thankful to Dai Aoki for growing the UPt_3 crystal, cutting, polishing and annealing it again. For both samples.

Je remercie Edward, Pierre, Olivier, Panayothis et Julien qui ont pris un moment de ses remplis agendas pour discuter avec moi. Et aussi les personnes avec lesquelles j'ai partagé

la salle de manip: Sébastien, Simon, Federico, ...

Un grand merci à Thibaut, Anne et Gilles pour usiner des pièces pour la manip. Et aussi au reste des voisins du pôle cryogenie, qui font vivre le couloir autour la salle de manip. Un mot pour remercier aussi Pascal et Elise pour les diffractions de rayon X et Joël qui a toujours un mot a échanger. Christine et Elodie méritent aussi un merci, pour leur gentillesses et humanités en l'administration, que c'est pas toujours facile.

Je voudrais remercier aussi des autres non permanents qui lesquels j'ai partagé joies et soucis: Victor (collegue et coloc), Vadim (voisin et copain de repas), Alex (cobureaux en fin de thèse), Etiennet (procastinateur officiel du bureau), Jérémy (toujours près à discuter), les collègues du Master 2 (Tristan, Loïc, Gregory, Melanie,...), et des autres .

Je voudrais remercier également beaucoup des personnes qui m'ont faire vivre hors laboratoire: Lise (soutenante indispensable), Simon (working coacher et organisateur de p'tit dej), Aurelie et Vincent (pour tous les moments en terre et en mer), Yvon (pour autres moments plutôt en terre), ma famille (pour son soutien dès loin), Daniela (una amiga de Madrid en Grenoble), le Folk et ses gens (un autre monde), ... et beaucoup des autres personnes que je laisse sans mentionner (desole!).

Resumé

Les travaux présentés dans cette thèse portent sur l'étude de la nature de l'état supraconducteur dans les composés UPt_3 et $PdTe_2$. A cette fin j'ai entrepris des mesures locales de champ magnétique la surface des composés à l'aide d'un microscope à SQUID (SSM). Celui-ci et les échantillons sont situés dans un cryostat, en nous permetant les refroidir jusqu'à 0.2 K. J'étais amené à explorer des voies pour améliorer la sensibilités des sondes SQUID déployées dans notre microscope.
Ci-dessous un résumé des différents chapitres.

Chapitre 1: introduction à la supraconductivité

Dans ce chapitre introductive je présente le phénomène de la supraconductivité et en quelques lignes les modèles théoriques. La supraconductivité est un état quantique macroscopique qui se distingue par une résistance électrique nulle et un diamagnétisme parfait en dessous d'une température critique T_c. Le comportement électromagnétique des supraconducteurs est décrit par les équations des frères London. La théorie BCS (appelée d'après ses auteurs Bardeen Cooper Schrieffer) décrit à l'échelle microscopique la supraconductivité: des phonons permettent à deux électrons de spin et moment opposé de former des paires de Cooper. Leur énergie est abaissée et un gap s'ouvre au niveau de la surface de Fermi. La théorie de Ginzburg-Landau utilise une fonction d'onde macroscopique pour traiter la dépendance spatiale du champ magnétique et des courants supraconducteurs. Cet état macroscopique quantique est à l'origine de la quantification du flux magnétique traversant un anneau supraconducteur en multiples entiers $\Phi_0 = 2.07 \cdot 10^{-15}$ Wb. Ceci est ce qu'on appelle un vortex.

Il existe deux échelles de longueur characteristiques: profondeur de pénétration (des champs magnétiques), λ, et longueur de cohérence (des électrons), ξ. Leur ratio définit le comportement du matériau sous champ magnétique: pour $\lambda/\xi < 1/\sqrt{2}$ ils expulsent tout champ magnétique à l'intérieur, ils s'agissent des supraconducteurs type I, et pour $\lambda/\xi >$

$1/\sqrt{2}$ ils permettent le flux de pénétrer en forme de vortex, on les appelle supraconducteurs de type II.

Jusqu'à ici, on a parlé de la supraconductivité qui est bien décrite par la théorie BCS, on l'appelle supraconductivité conventionnelle. Par contre, il existe des autres supraconducteurs qui ne peuvent pas être décrits par cette théorie. L'interaction électrons-phonons est remplacé par d'autres mécanismes comme des fluctuations magnétiques et des symétries additionnelles à celle de la symétrie de jauge peuvent être brisées. On parle dans ce cas d'un supraconducteur non conventionnel.

Dans la supraconductivité non-conventionelle, les paires de Cooper peuvent avoir des moments orbitaux no nuls et le spin peuve être singulet ou triplet. Les supraconducteurs à base de cuprates, les fermions lourds ou pnictides sont quelques familles des supraconducteurs non-conventionels.

En particulier, UPt_3 est un composé à fermions lourds qui s'ordonne antiferromagnétiquement avec un faible moment à 5 K avant de transiter à $T_c = 550$ mK dans l'état supraconducteur.

Ce composé présente 3 phases supraconductrices différentes dans le diagramme de phase (T-H). Pour chaque phase le paramètre d'ordre change de symétrie. Le champ critique supérieur est large comparé avec T_c et montre une large anisotropie. Par contre, il n'y a pas de consensus sur l'anisotropie du champ critique inférieur. En plus, il présente normalement une cassure de pente aux alentours de la deuxième transition. Des mesures de susceptibilité de spin ne montrent pas de changement entre avant et après la transition, ce qui illustre des paires de Cooper avec spin triplet.

Des mesures de transport (chaleur, son ou électrique) avec une résolution angulaire montrent différentes symétries du paramètre d'ordre. La symétrie du paramètre d'ordre est importante pour déduire la représentation théorique. En consequence, plusieurs scénarios sont proposés avec les cas de spin singulet/triplet ou couplage spin-orbite faible/fort, mais, il n'y a pas de consensus.

Chapitre 2: dispositif experimental

Ici, je présente les moyens mis en oeuvre pour l'étude des supraconducteurs à très basses températures. Pour cela, un cryostat à dilution (mélange de ^{3}He et ^{4}He) est utilisé, avec lequel on peut refroidir jusqu'à 200 mK. La sonde magnetique du microscope est un SQUID (Superconducting Quantum Interference Device). Ceci est une boucle supraconductrice avec deux jonctions Josephson en parallèle. La quantification s'applique et le flux à l'intérieur de la boucle doit être toujours un multiple entier du quantum de flux, donc le courant circulant a aussi une periodicité de Φ_0, ainsi que le courant critique que l'on mesure.

L'imagerie à SQUID est possible grâce à la régulation en champ proche. Elle fait appel à un résonateur piézoélectrique (un diapason en quartz) portant le SQUID chip et un actuateur piézoélectrique portant le diapason. Une régulation sur la phase et la fréquence de résonance du diapason commande le piézo-actuateur en vue de maintenir le *contact* entre la pointe du SQUID et la surface de l'échantillon lors de l'imagerie.

Le balayage de l'échantillon sous la boucle du SQUID est fait par un *scanner*, consistant en quatre bimorphes piézoélectriques qui fléchissent dans une direction (deux pour l'axe x et deux pour l'axe y) pour déplacer finement l'échantillon. Le mouvement est de grand précision ($<$1 nm) et d'une portée de l'ordre de 50 micromètres. Le microscope est également équipé de trois moteurs piézoélectriques (déplacement par une alternance de coller-glisser) permettant des déplacements grossiers de 5 mm environ. Le champ magnétique appliqué sur l'échantillon est généré par une bobine résistive située à l'extérieur du cryostat.

Chapitre 3: état intermédiaire en $PdTe_2$

$PdTe_2$ devient supraconducteur à une température de 1.6 K. Des mesures thermodynamiques et des expériences de rotation de spin de muons proposent une supraconductivité de type I, qui n'est pas courante pour des composés binaires. Par contre, les mesures de microscopie tunnel à balayage et de spectroscopie à contact sur point ont montré des vortex, qui est une signature de supraconductivité de type II.

Le microscope de SQUID à balayage (SSM) a été utilisé pour des mesures de piégeage de flux et d'imagerie de structures de flux suite à des refroidissements sous champ magnétique ou à champ nul. La coexistence de régions normales et de régions supraconductrices nous a permis de mettre en évidence l'état intermédiaire qui est révélateur d'une supraconductivité de type I. Les régions normales contenaient plusieurs quantum de flux magnétique. En appliquant le champ magnétique dans l'état supraconducteur, le flux pénètre d'abord sous forme de tubes, qui s'arrangent en un réseau régulier de tubes avant de fusionner en laminae. Sous champ magnétique croissant, les laminae normaux s'élargissent au détriment des laminae supraconductrices jusqu'à la disparition des dernières lorsque le champ critique est atteint. On a aussi souvent observé des zones supraconductrices enfermées par zones normales, cela s'appelle de branchement. Les résultats de nos expériments sur $PdTe_2$ mettent en évidence de la supraconductivité de type I à travers de l'existence de l'état intermédiaire.

Chapitre 4: supraconductivité chirale en UPt_3

Le diagramme de phase d'UPt_3, avec multiple phases, est fréquentement comparé au celui du ^{3}He. Cet élément présente une phase superfluide avec spin triplet et un état fondamental dégénéré et chiral. Sur UPt_3, la phase à basse température et bas champ (phase B) semble avoir un état fondamental dégénéré par rapport à la chiralité des paires de Cooper.

Sur un matériau, ceci peut être représente comme un domaine chiral, qui occupe tout le cristal ou plusieurs domaines de chiralités opposées, séparés par des parois. La distribution des champs magnétiques aux alentours des parois devraient en témoigner par la présence des structures portant des fractions du quantum de flux, et/ou d'accumulation et l'absence de flux d'un coté et de l'autre de la paroi.

J'ai utilisé le SSM pour chercher et mettre en évidence ces structures. Au cours de ma thèse, j'ai imagé les deux phases à bas champ ($H \parallel c$) sur la face ab du cristal. Dans la phase B et à très bas champ, j'ai quantifié le flux d'un vortex et analysé la longueur de pénétration en fonction de la temperature, en comparant avec les valeurs reportés dans la

littérature et avec la valeur estimée à partir de H_{c1}. La quantification de ce vortex et le suivi en température m'a permis d'identifier des structures portant la moitié d'un quantum de flux dans cette phase. La division d'un vortex en ces structures fractionnaires et leur recombinassion montrent leur proximité énergetique.

Dans cette même phase, des domaines supraconducteurs ont été révélés, avec des parois de domaines décorés par le flux magnétique. En particulier, on a mis en évidence l'accumulation et l'absence de flux d'un coté et de l'autre de la paroi. En plus, les domaines semblent se fermer à plus basses temperatures. L'analyse des courants à l'origine de cette distribution de flux inusuelle montre qu'il y existe des autres courants que ceux d'écrantage: des courants chiraux, qui circulent en sens opposés de chaque coté de la paroi. Cela démontre l'état chiral de cette phase et l'interaction entre les états chiraux des domaines.

Chapitre 5: SQUIDs shuntés

J'ai travaillé sur l'amélioration des sondes SQUID. Les SQUIDs actuels sont hystérétiques à cause d'un échauffement local au niveau des micro-ponts lorsque le courant de polarisation atteint leur courant critique (I_c). Pour recommencer une mesure le SQUID doit redevenir supraconducteur. Ceci ralenti la vitesse des mesures et limite la résolution. Les nouveaux SQUIDs ont une couche métallique en parallèle à la couche supraconductrice: SQUIDs shuntés. Cela réduit la résistance à la transition et permet une mesure continue. En partant des résultats antérieurs sur des SQUIDs bicouche Nb/W ($dV/d\Phi_0 \mid_{max}= 1.5$ mV/Φ_0), j'ai rendu le dessin compatible avec le SSM. Comme nous avons préservé entièrement la couche de W les résistances du shunt étaient faibles et la tension aux bornes du SQUID basse, la meilleure sensibilité mesuré est $dV/d\Phi_0 \mid_{max}= 1.5$ μV/Φ_0. Le bruit en flux de ces SQUIDs est comparable à celui-ci des SQUIDs hystérétiques en aluminium. Des possibilités d'amélioration sont la réduction de l'épaisseur du shunt, la polarisation du SQUID en tension et l'utilisation d'un amplificateur de courant cryogénique.

Mots clés

Microscopie, SQUID, supraconductivité, UPt_3, $PdTe_2$, supraconductivité chirale, état intermédiaire, vortex fractionaire.

Abstract

The work presented in this manuscript focuses on the nature of the superconducting state realized in the compounds UPt_3 and $PdTe_2$. For this objective I employed spatially resolved local magnetization measurements at the surface of the samples by means of a Scanning SQUID Microscope (SSM). The microscope and the samples are placed in a cryostat and they can be cooled down to 200 mK. During my thesis I was also worked in view of improving the sensitivity of our SQUIDs.

In the following I will present a synopsis of the following chapters.

Chapter 1: introduction to superconductivity

Superconductivity is a macroscopic quantum state distinguished by zero electrical resistance and a perfect diamagnetic behavior below a critical temperature Tc. Microscopically superconductivity is described by the BCS theory (named after its authors Bardeen, Cooper and Schrieffer), which considers an attractive electron-phonon interaction to couple two electrons of opposite spin and momentum to lower their energy. Thus an energy gap in the density of states forms. The Ginzburg-Landau theory uses a macroscopic wave-function, breaking the gauge symmetry, to calculate the spatial dependence of magnetization and superconducting currents. Due to the phase coherence of the wavefunction the magnetic flux threading a superconducting ring is quantized in entire multiples of the quantum of flux: $\Phi_0 = 2.07 \cdot 10^{-15}$ Wb. This is called a vortex.

There are two characteristic length scales: the penetration depth (of magnetic fields), λ, and the coherence length (of the electrons), ξ. Their ratio defines the magnetic behavior of the material: for $\lambda/\xi < 1/\sqrt{2}$ they expel all the magnetic field inside of the superconductor and are called type-I superconductors, and for $\lambda/\xi > 1/\sqrt{2}$ they allow the penetration of the magnetic field in form of vortices above a given field, they are called type-II superconductors.

So far, the presented superconductivity is well described by the BCS theory, this is called conventional superconductivity, however, there are other superconductors that cannot

be explained by this theory. For example magnetic fluctuations may replace the electron-phonon interaction and other symmetries in addition to the gauge symmetry may be broken. These are called unconventional superconductors.

The Cooper pairs of these superconductors may have larger orbital moments, and the spin is not restricted to the singlet state, but the triplet state is also possible. Cuprate-based superconductors, heavy fermions or pnictides are some families of unconventional superconductors.

In particular, UPt_3 is a heavy fermion compound that orders weakly antiferromagnetically at $T_N = 5$ K before it becomes superconducting at $T_c = 550$ mK.

UPt_3 presents 3 different superconducting phases in the T-H phase diagram. For each of these phases, the symmetry of the order parameter changes.

The upper critical field is large compared to the T_c and it shows an important anisotropy. However, there's no consensus about the anisotropy of the lower critical field. In addition, it usually presents a kink around the second transition. Measurements of spin susceptibility don't show any change between before and after the transition, supporting spin-triplet Cooper pairs.

Angle-resolved transport measurements (heat, sound or electric) show different symmetries of the order parameter. This symmetry is important in order to choose the right theoretical representation. Various scenarios have been proposed with spin-singlet/triplet or strong/weak spin-orbit coupling, however, there's still no consensus.

Chapter 2: experimental setup

In this chapter I describe the tools employed for the low temperature superconductors I studied. A dilution refrigerator (mixture of ^{3}He and ^{4}He) was used for cooling down to 200 mK. The SQUID is the probe sensitive to magnetic flux. The Josephson effects and the quantification of flux are the basis of the SQUIDs (Superconducting Quantum Interference Device). The SQUIDs used in our microscope have two Josephson junctions in parallel

forming a superconducting loop. The quantification applies thus the flux inside the loop must be an integer number of Φ_0, therefore, the critical current of the SQUID is also Φ_0-periodic.

Scanning is possible thanks to the near-field regulation, consisting of a piezo actuator carrying the piezo electric resonator (quartz tuning fork) on to which the SQUID chip is glued, the sample and the regulation loops. A regulation based on frequency and phase of the tuning fork resonance maintains the *contact* between chip tip and the sample's surface during scanning.

The sample displacement under the SQUID tip is realized by a scanner consisting of 4 bimorph piezoelectric bending elements, two for the x direction and two for the y direction. The movement is of high precision (< 1 nm) and covers an area of about 50 x 50 micrometers. The long range movements are carried out with piezoelectric slip stick motors one for each of the three axis. These displacements are quite irregular but allow us to move up to 5 mm. A resistive copper coil situated outside of the cryostat applies a homogenous magnetic field to sample and SQUID.

Chapter 3: intermediate state in $PdTe_2$

$PdTe_2$ becomes superconducting at 1.6 K. Thermodynamic and muon spin rotation experiments proposed type-I superconductivity, which is unusual for binary compounds. On the other hand scanning tunnel microscopy and point contact spectroscopy observed vortices supporting the existence of type-II superconductivity.

The SSM allowed me to undertake flux pinning measurements and to image the different flux patterns after cooling under (zero) magnetic field. The visualization of coexisting superconducting and normal regions is proof of the intermediate state constituting a hallmark of type-I superconductivity. The normal regions carried more than one quantum of flux. When the magnetic field enters the sample, the magnetic flux is arranged in more or less tubular structures that tend to form a lattice. When increasing the applied field, these structures

fuse and form laminae, that increase in size until the superconducting regions disappear. We observed quite often superconducting regions enclosed by normal regions, the so-called branching. The results of these experiments show unambiguous type-I superconductivity with the presence of intermediate state.

Chapter 4: chiral superconductivity in UPt_3

The multiple-phase phase diagram of UPt_3 is often compared to the one of ^3He. This element presents a superfluid phase with spin triplet and a degenerate ground state. In UPt_3, the low temperature and low field phase (B-phase) is expected to have a degenerate ground state with respect to the chirality of the Cooper pairs.

In a material, this may be represented as a single chiral domain, which occupies the whole crystal, or multiple domains with opposed chiralities and separated by domain walls. The magnetic flux distribution around the domain walls should reveal it by the presence of flux structures holding a fraction of the quantum of flux, and/or the accumulation and absence of flux in each side of the domain wall.

I used the SSM for exploring and revealing these structures. I imaged the field distribution above the *ab* face of the crystal in the low field phases with $H \parallel c$. In the B-phase and at very low fields, I quantified the flux of a vortex and analyzed the penetration depth as a function of the temperature, comparing it with the values reported in the literature and the estimate obtained from H_{c1}. Thanks to them, I was able to identify structures with half a quantum of flux. I also observed the division of a vortex into two of these structures and their recombination, deducing a small energy difference between them.

In this same phase, superconducting domains were revealed, with domain walls decorated by magnetic flux. In particular, I show the accumulation and absence of flux in each side of the domain wall. Moreover, the domains seem to close up at lower temperatures. The analysis of the currents at the origin of the unusual flux distribution shows the existence of other currents than the screening ones: chiral currents, which flow in opposite directions

in each side of the domain wall. These results show the chiral state and the interaction between the domains of the B-phase in UPt_3.

Chapter 5: shunted SQUIDs

I worked on the improvement of the SQUID detector. Our currently SQUIDs are hysteretic due to the local heating at the narrow microbridges when their critical current (I_c) is reached. Before the next Ic measurement the SQUID has to be become superconducting again, which implies a slow measurement cycle. The new SQUIDs have a metallic layer shunting the superconducting layer. reducing the normal state resistance of the SQUID and allows for a continuous measurement method. Based on prior results on Nb/W SQUIDs ($dV/d\Phi_0\mid_{max}$= 1.5 mV/Φ_0) I adapted the layout for the SSM. As we took care to leave the W layer unetched the shunt resistance was low and the voltage signal weak ($dV/d\Phi_0\mid_{max}$= 1.5 μV/Φ_0). The measured flux noise was comparable to the noise of the present hysteretic SQUIDs. Possible routes to higher sensitivity are reduction of the shunt thickness, voltage biasing and the installation of a cryogenic current amplifier.

Keywords

Microscopy, SQUID, superconductivity, UPt_3, $PdTe_2$, chiral superconductivity, intermediate state, fractional vortices.

Index

List of Figures

List of Tables

Chapter 1

Introduction to superconductivity

In this chapter I will briefly discuss some aspects of conventional superconductivity which are important for the understanding of the experimental setup and our measurements. First I will recall the historical key events, then introduce the London model. After a brief introduction of Landau's theory of second order phase transitions and the Ginzburg-Landau theory, I will talk about to some properties of conventional superconductors. I will follow with the key points of our microscope: superconducting quantum interference devices and I will conclude with a small introduction to unconventional superconductivity, presenting some families of unconventional superconductors such as the heavy fermions.

1.1 Discovery of superconductivity

In 1911, Kamerlingh Onnes and Gilles Holst found that the resistance of mercury is zero below T_c, its critical temperature [1].

In 1933, Meissner and Ochsenfeld discovered the perfect diamagnetism of superconductors, the Meissner-Ochsenfeld effect [2]. The magnetic field is excluded from the interior of the superconductor in the two following cases: when the field is applied after cooling below T_c and when the field is applied before cooling. The Meissner-Ochsenfeld effect demonstrates that the superconducting state is a thermodynamic ground state.

In 1935, Fritz and Heinz London created a simple model describing the zero resistivity and perfect diamagnetism of superconductivity [3]. They made the following two assump-

tions: (i) there is a density n_s of electrons moving without resistance and (ii) n_s is zero at T_c and grows steadily as the temperature lowers. In combination with Maxwell's equations the London equations establish the electrodynamics of superconductors.

It took another 15 years and Landau's theory of phase transitions [4] to develop a phenomenological theory of superconductivity: the Ginzburg-Landau theory [5]. One of the most famous result is the flux quantification of a vortex and their arrangement in a lattice, which were first described by Abrikosov in 1957 [6].

By that time, several authors worked on the underlying physics, culminating the BCS theory, named after its inventors Bardeen, Cooper and Schrieffer [7, 8]. BCS theory considers an attractive potential between electrons in addition of the Coulomb repulsion. An example of the origin of an attractive potential are phonons, predicted in 1950 by Fröhlich [9] and probed experimentally the same year by Maxwell [10] and Reynolds [11]. One of the most important predictions made by this theory is the relationship between the energy gap, Δ, and the superconducting temperature: $\Delta = 1.76 k_B T_c$. The energy gap governs the low temperature behavior of several physical properties, for example, the specific heat of a BCS superconductor with isotropic gap diminishes exponentially with lowering temperature.

In 1956, Cooper showed that the attractive interaction, even if arbitrarily weak, would lead to an instability of the Fermi sea and would create a bound state of two electrons called Cooper pairs [12].

W. Little and R. Parks measured, 6 years later, a periodicity in the electrical resistance of an empty and thin-walled superconducting cylinders subjected to a parallel magnetic field. The period was always $\Phi_0 = \hbar/2e = 2.07 \cdot 10^{-15}$ Wb, the quantum of flux. The Little-Parks effect is a result of collective quantum behavior of superconducting electrons, which reflects that flux is quantized in superconductors. This effect also demonstrates that the magnetic vector potential couples to an observable, such as the superfluid density [13].

In the same year, B. D. Josephson suggested the new effects of superconducting pairs tunnelling a barrier [14]. The barrier or weak link can consist of a thin insulating barrier

(known as a superconductor-insulator-superconductor junction, or S-I-S), a short section of non-superconducting metal (S-N-S), or a physical constriction that weakens the superconductivity at the point of contact (S-s-S). P. Anderson and J. Rowell succeeded the measurement of Josephson's effect [15].

In 1979, F. Steglich *et al.* showed that some compounds with large renormalized electron masses also presented superconductivity. These are the so-called heavy fermion systems [16].

In 1986, J. Georg Bednorz and K. Alex Mueller discovered superconductivity in a lanthanum-based cuprate compound, which had a transition temperature of 35 K. This was the first high-temperature superconductor. Shortly afther, C.-W. Chu found that replacing the lanthanum with yttrium, i.e. making YBCO, raised the critical temperature to 92 K, which is above the boiling point of nitrogen at atmospheric pressure. Many other cuprate superconductors have been discovered since then. The theory of superconductivity in these materials is one of the major outstanding challenges of theoretical condensed-matter physics nowadays.

More superconductors and of different kinds were discovered as presented in fig. 1.1. Recently, highly pressurized compounds such as lanthanum decahydride (LaH_{10}) [18, 19], carbonaceous sulfur hydride (CH_8S) [20] or layered yttrium-palladium-hydron [21], reached critical temperatures around room temperature.

1.2 Conventional superconductivity

1.2.1 London equations

As mentioned in the historical introduction, the brothers Fritz and Heinz London developed a simple model to describe the electromagnetic properties of a superconductor [3], using as starting point the equation of electron's motion in the Drude model:

$$m\frac{d\mathbf{v}}{dt} = q\mathbf{E} - m\frac{\mathbf{v}_{drift}}{\tau} \tag{1.1}$$

with τ being the time between collisions ($\tau \to \infty$ for an ideal conductor) and m and q

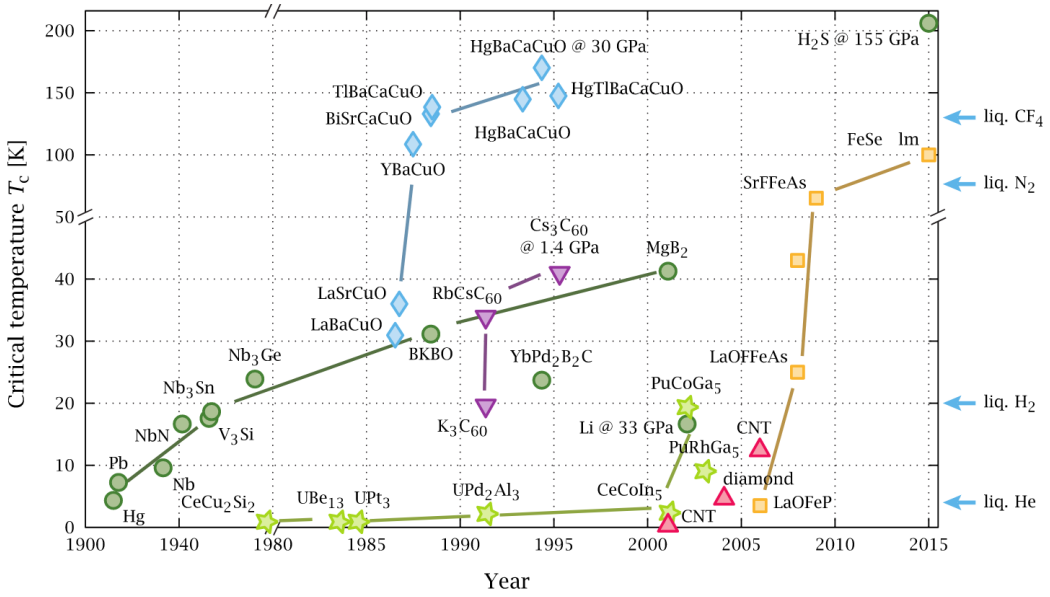

Figure 1.1: *Overview of superconducting critical temperatures and discovery of various superconducting materials. Color code: dark green circles are BCS-like, light green star are heavy-fermions, blue diamonds are cuprates, purple inverted triangles are Buckminsterfullerene-based (C_{60}-based), red triangles are other carbons-based, and pnictides are represented in orange squares. Figure reused from ref. [17].*

corresponding to the mass and charge of the superconducting particles. They used the two-fluid model to describe the superconductivity: the total charge density n is the sum of normal and superconducting charge densities, n_n and n_s respectively. In the normal state $n = n_n$ and $n = n_s$ at $T \to 0$.

Considering $\tau \to \infty$ and using $\mathbf{j_s} = q_s n_s \mathbf{v}$, the superconducting current can be rewritten as the so-called first London equation[1]:

$$\frac{\partial \left(\frac{m_s}{n_s q_s^2} \right) \mathbf{j_s}}{\partial t} = \mathbf{E} \tag{1.2}$$

The Ohm's law $\mathbf{j} = \sigma \mathbf{E}$ arises from the same model considering no time dependence and a finite τ: $\mathbf{j} = q^2 n \tau / m \cdot \mathbf{E}$. In a perfect conductor the electric field $\mathbf{E}$ is proportional to the time derivative of the current whereas in a resistive material, it is proportional to the

[1] The total derivative becomes partial derivative after solving the system for one solution of the magnetic field.

current itself. The physical meaning of eq. 1.2 is the zero resistivity of a superconductor ($\tau \to \infty$).

Applying the Maxwell-Faraday equation ($\nabla \times \mathbf{E} = -\frac{\partial \mathbf{B}}{\partial t}$) to eq. 1.2 yields:

$$\frac{\partial}{\partial t}\left[\nabla \times \frac{m_s}{n_s q_s^2}\mathbf{j_s} + \mathbf{B}\right] = 0 \tag{1.3}$$

These equations apply for all perfect conductors. A superconductor must expel the magnetic field as sketched in fig. 1.2, i.e. the Meissner-Ochsenfeld effect. For this, the material spontaneously creates supercurrents so that the corresponding field compensates the external field well inside of the superconductor ($\mathbf{B} = 0$). Thus, applying the Ampère's circuital law to eq. 1.3 leads to the second London equation:

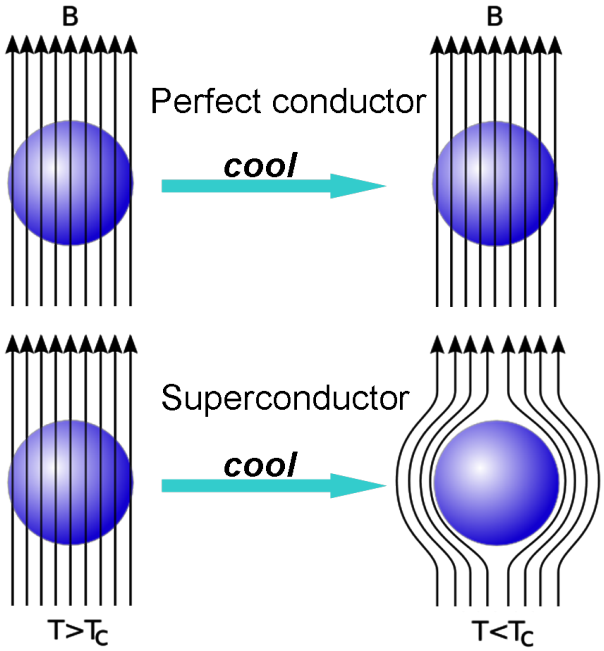

Figure 1.2: *Schema of a superconductor and a perfect conductor that are cooled in magnetic field. The superconductor expels the internal magnetic field but the perfect conductor is permeable to it. This image comes from Wikipedia.*

$$\nabla \times \frac{m_s}{n_s q_s^2}\mathbf{j_s} + \mathbf{B} = 0 \tag{1.4}$$

In the case of a superconductor in the $x > 0$ half space with an applied field $\mathbf{B} = B_0\mathbf{z}$

the solution of eq. 1.4 is:

$$B_z(x) = B_0 e^{-x/\lambda_L}$$

$$j_{s,y}(x) = j_{s,0} e^{-x/\lambda_L}$$

where λ_L is the London penetration depth, given by:

$$\lambda_L = \sqrt{\frac{m_s}{\mu_0 n_s q_s^2}} \tag{1.5}$$

with μ_0 being the vacuum permeability. The decay of the magnetic field that penetrates the superconductor and the supercurrents that screen it happens exponentially with a characteristic length scale λ_L.

1.2.2 The Ginzburg-Landau theory

In the previous section, London equations consider that the density of superconducting carriers is constant in space. This is not the case in the proximity of normal/superconducting interface, such as at surface of a superconducting sample.

In 1950, Vitaly L. Ginzburg and Lev D. Landau (GL) developed a phenomenological theory that describes superconductivity and can take into account the spatial dependence of n_s [5]. As the superconducting state is macroscopic and coherent, it can be expressed by a complex wavefunction, called order parameter [4, 22].

Landau theory

The Landau theory is a phenomenological description of a system, which is based on the minimization of the energy functional of the system. The functional has one (or more) parameter, called order parameter, which evolve from one phase (higher symmetry), where it is zero, to the other phase (lower symmetry), where it is finite.

The free energy functional, F, is written in terms of the order parameter, ψ. This theory describes successfully continuous and discontinuous phase transitions, like paramagnetic-ferromagnetic or liquid-gas transitions. The free energy $F(\psi)$ is developed in terms of ψ

(close to the transition temperature so that ψ is small). The expansion has to preserve the symmetry of the system (same symmetry that the corresponding Hamiltonian), and thus some terms of the Taylor expansion won't appear in the expansion of the free energy.

In a continuous transition, the free energy expansion (in absence of fields) yields:

$$F = a\,|\psi|^2 + \frac{1}{2}b\,|\psi|^4 + constant \tag{1.6}$$

with ψ being the order parameter of the system and a and b are functions of temperature. Because of the symmetry of this kind of transition (invariance under $\psi \to -\psi$), only even power terms appear. By minimizing this free energy with respect to $|\psi|$ we obtain:

$$2a\,|\psi_0| + 2b\,|\psi_0|^3 = 0 \;\rightarrow\; |\psi_0| = 0 \text{ or } |\psi_0|_s = \pm\sqrt{\frac{-a}{b}} \tag{1.7}$$

where b must be positive to assure the stability of the system. For a qualitative behavior we can consider that a is proportional to $T - T_c$ at first-order expansion, therefore the critical temperature, T_c, is given by the condition $|\psi_0(T_c)| = 0$. Above this temperature, the lowest free energy state is obtained for $\psi_0 = 0$. As one crosses T_c two absolute minimas appear at finite values of ψ_0.

One example of continuous phase transition is the ferromagnetic/antiferromagnetic. In this case the order parameter is the magnetization ($\psi \to M$), which is finite in the ferromagnetic phase ($M_s = \pm\sqrt{-a/b}$) and zero in the antiferromagnetic phase ($M_0 = 0$).

In figure 1.3 the free energy for this case is depicted. Above the transition temperature the lowest free energy is obtained for zero magnetization. As one crosses the transition temperature (T_{Curie}) two absolute minima appear at finite magnetization values. These two values correspond to a spontaneous magnetization (without the influence of an external magnetic field, the system has the magnetization $+M_s$ or $-M_s$).

Once the system is in the state $-M_s$, one has to overcome the local maxima of the free energy curve in order to drive the system into the M_s state. An external field would add a

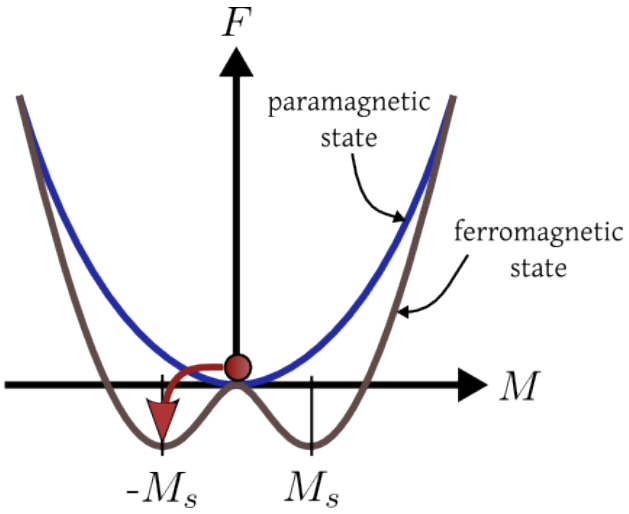

Figure 1.3: *The free energy as a function of the magnetization for the paramagnetic (blue line) and the ferromagnetic state (black line). The ground state (represented by the red circle)implies a spontaneous magnetization as the transition is crossed. Note that constant contributions are neglected.*

linear offset to this curves. If the magnetic field is strong enough, the system will overcome the barrier and change of state. This effect is called hysteresis.

Ginzburg-Landau theory

Inspired by the quantum nature of the superconductivity, Ginzburg and Landau proposed a complex order parameter: $\psi \rightarrow \psi(\mathbf{r}) = |\psi(\mathbf{r})| \exp(i\theta(\mathbf{r}))$. The density of states is given by $n_s(\mathbf{r}) = |\psi(\mathbf{r})|^2$. The order parameter is non-zero in the superconducting state, therefore it has lower symmetry than the normal state. Normal electrons are totally incoherent and a phase shift in their wavefunctions does not change the macroscopic state. In the case of superconducting electrons, they behave coherently, with a common phase, thus, a phase shift of one electron wavefunction is not possible. This is the gauge symmetry that is broken in the superconducting state.

Given the macroscopic coherence, the existence of a magnetic field, $\mathbf{B}$, originated by the vector potential, $\mathbf{A}$, will couple to the order parameter. The resulting GL functional can be

written as follows:

$$F = F_n + \alpha \left|\psi(\mathbf{r})\right|^2 + \frac{1}{2}\beta \left|\psi(\mathbf{r})\right|^4 + \frac{\left|\mathbf{B}\right|^2}{2\mu_0} + \frac{1}{2m_s}\left|(-i\hbar\nabla - q_s\mathbf{A})\,\psi\right|^2 \tag{1.8}$$

where m_s and q_s are the mass and charge of the superconducting particle (we indicate the subindex s knowing beforehand that the superconducting quasiparticles will be Cooper pairs). The critical field is given by the condition $F(H_c) = F_n$, where the superconducting energy and normal-state energy are equals. When the system crosses the superconducting transition the former minimum becomes unstable and the system finds another minimum with a random phase. This rotation symmetry will be important when we will talk about SQUIDs in sec. 1.2.3. The free energy can be minimized with respect ψ and $\mathbf{A}$, which yields the first and second Ginzburg-Landau equations respectively:

$$\alpha\psi(\mathbf{r}) + \beta\left|\psi(\mathbf{r})\right|^2\psi(\mathbf{r}) + \frac{1}{2m_s}\left(-i\hbar\nabla - q_sA\right)^2\psi(\mathbf{r}) = 0 \tag{1.9}$$

$$\mathbf{j}_s(\mathbf{r}) = \frac{i\hbar q_s}{2m_s}\left(\psi^*(\mathbf{r})\nabla\psi(\mathbf{r}) - \psi(\mathbf{r})\nabla\psi^*(\mathbf{r})\right) + \frac{q_s^2}{m_s}\left|\psi(\mathbf{r})\right|^2\mathbf{A} \tag{1.10}$$

In the case of homogeneous n_s and the absence of magnetic field, the solution to the first GL equation (eq. 1.9) becomes $\left|\psi_s\right|^2 = -\alpha/\beta$ for the superconducting phase. The value of α changes of sign depending on the phase, however, $\alpha < 0$ in the superconducting phase. Considering that the order parameter has spatial dependence as $\psi(r) = \sqrt{n_s}e^{i\theta(r)}$, the second GL equation (eq. 1.10) results in:

$$\mathbf{j}_s(\mathbf{r}) = \frac{-q_s}{m_s}\frac{\left|\alpha\right|}{\beta}\left[\hbar\nabla\theta(\mathbf{r}) - q_s\mathbf{A}(\mathbf{r})\right] \tag{1.11}$$

Characteristic lengths

Comparing this expression with the second London equation (eq. 1.4) yields a characteristic length called penetration depth, which takes the form of

$$\lambda = \sqrt{\frac{m_s\beta}{\mu_0 q_s^2\left|\alpha\right|}} = \sqrt{\frac{m_s}{\mu_0 q_s^2 n_s}} \tag{1.12}$$

thus the penetration depth for London description and for Ginzburg-Landau theory are equivalents.

Now, we will consider the spatial dependence of ψ with no magnetic field in an one spatial dimension for simplicity. Introducing the adimensional function $f(x) = \psi(x)/\psi_\infty$ (ψ_∞ represents the value of ψ infinitely deep in the superconductor and it's given by the non-zero solution of eq. 1.9), the first GL equation can be rewritten as follows:

$$\frac{\hbar^2}{2m_s\alpha}\frac{d^2f(x)}{dx^2} - f(x) + f^3(x) = 0$$

By dimensional analysis we find another characteristic length, called coherence length, which is given by:

$$\xi = \sqrt{\frac{\hbar^2}{2m_s\,|\alpha|}} \tag{1.13}$$

This length represents the distance over which $\psi(\mathbf{r})$ can vary without importantly modify the energy. We can also imagine it as the distance between the electrons of a Cooper pair [23].

The ratio of these two characteristic lengths is the Ginzburg-Landau parameter:

$$\kappa = \frac{\lambda}{\xi} \tag{1.14}$$

and it determines the behavior of the superconductivity under magnetic field:

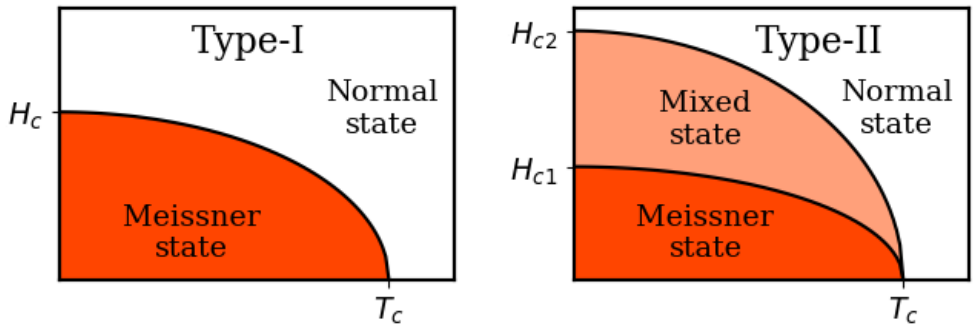

Figure 1.4: *T-H phase diagram of type-I and type-II superconductors. In the Meissner state the magnetic field is totally expelled from inside. In the mixed state, it's more energetically stable to let the magnetic flux penetrate in form of vortices. In the normal state, there's no superconductivity.*

- $\kappa > 1/\sqrt{2}$: The system gains condensation energy while minimizing the interfaces between superconducting-normal domains [23]. If the applied field exceeds H_c, the superconductivity is broken in the whole system. These superconductors are called type-I superconductors.

- $\kappa < 1/\sqrt{2}$: The interfaces becomes energetically more favorable. Under magnetic field, the system maximizes them by creating normal-state tubes, called vortices, each of them holding a single flux quanta (Φ_0). Because of the magnetic field, a vortex is enclosed by superconducting currents, similarly that the screening currents in the sample edges. At $H_{c2} \approx \Phi_0/2\pi\mu_0\xi^2$ the magnetic field will destroy the superconducting state. These superconductors are the so-called type-II superconductors.

The frontier at $\kappa = \frac{1}{\sqrt{2}}$ arises from taking both lengths into account in the energetic analysis [24].

Flux quantization

A vortex is a magnetic structure in a superconductor containing exactly Φ_0 of flux. To deduce this phenomena, we will suppose that the superconducting density is constant and the spatial dependence comes only from the phase of the order parameter, as presented in eq. 1.11. This equation can be related to the particles speed, using the canonical momentum deduced from the eq. 1.8 by dimensional analysis: $\mathbf{p} = (\hbar\nabla\theta - q_s\mathbf{A})$:

$$\mathbf{j}_s(\mathbf{r}) = \frac{-q_s n_s}{m_s}\left[\hbar\nabla\theta(\mathbf{r}) - q_s\mathbf{A}(\mathbf{r})\right] = -q_s n_s \mathbf{v}_s(\mathbf{r}) \tag{1.15}$$

Let us imagine a superconducting loop. By applying a magnetic field $\mathbf{B}$ perpendicular to the loop, we induce a stationary supercurrent. As the superconducting state is a macroscopic quantum state, the stationary states are described by quantum numbers, thus we expect a quantization. By integrating eq. 1.15 along the considered loop and using the Stokes theorem, we obtain the flux of the system:

$$\Phi = \frac{\hbar}{q_s}\oint_C \nabla\theta \cdot d\mathbf{l} = \int_A \mathbf{B}\cdot d\mathbf{S} - \oint_C \frac{m_s}{n_s q_s^2}\mathbf{j}_s \cdot d\mathbf{l} \tag{1.16}$$

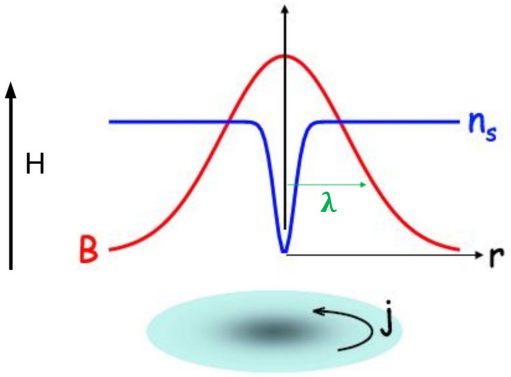

Figure 1.5: *Schema of a vortex. The density of superconducting particles, n_s, diminishes inside the vortex. The magnetic field, $\mathbf{B}$, is screened from entering into the superconducting state by the screening currents, $\mathbf{j}$, indicated in the image [25].*

with A being the area inside the closed loop C. The left-term integral has infinite solutions of the form $2\pi n$ as the wavefunction has to be single-valued. Hence, the equation 1.16 can be rewritten as following:

$$\Phi = \frac{\hbar}{q_s} 2\pi n = n\Phi_0 = \int_A \mathbf{B} \cdot d\mathbf{S} - \oint_C \frac{m_s}{n_s q_s} \mathbf{j}_s \cdot d\mathbf{l} \tag{1.17}$$

with $\Phi_0 = h/q_s = h/2e \approx 2.07 \times 10^{-15}$ Wb being the quantum of flux. As the phase integral has a quantized solution, the magnetic flux through the sample (term of the magnetic field minus the term of the shielding field created by the supercurrent) is quantized. This result is easily seen for a sample with no holes, nevertheless, taking into account the London equation (eq. 1.4) it follows that this result is still true for any path of integration around a given hole [23]. Inside the sample the magnetic field is bundled into vortices. In the radial direction the magnetic field is attenuated by superconducting screening currents around the vortex, resulting in a magnetic vortex size of the order of the penetration depth, $2\lambda_L$. This is schematically shown in the fig. 1.5.

So far, a magnetic structure may contain any integer number of Φ_0. From eq. 1.8, we can easily deduce that the energy of two Φ_0 structures is lower than the energy of a $2\Phi_0$ structure, therefore, a vortex must hold $1\Phi_0$. The type-II superconductors minimize their energy by allowing the magnetic field in single flux-quantified structures called vortices. Hence, the

most stable flux distribution for a flux $n\Phi_0$ is n vortices (with a single Φ_0) distributed, in general, in a triangular lattice [26].

1.2.3 SQUIDs

In this section I give a brief introduction to direct current Superconducting QUantum Interference Devices (dc-SQUID). A SQUID (all the SQUIDs in this thesis are dc-SQUIDs, so I will omit the dc from here on) consists of a superconducting loop with two weak links called Josephson junctions, as depicted in fig. 1.6. The critical current of this devices depends on the magnetic flux going through the loop, which is Φ_0-periodic.

For introducing this device, I will first introduce the Josephson effect and then the SQUID itself.

Josephson effect

B. D. Josephson predicted that Cooper pairs could tunnel a energy barrier. In particular, when this barrier is the junction between two superconductors, the penetrating wavefunctions of the two superconductors interfere defining the critical current of the junction [14]:

$$j = j_c \sin(\Delta\varphi) \tag{1.18}$$

where j_c is the characteristic critical current of the junction and $\Delta\varphi$ is the phase difference between the wavefunctions of the superconductors on either side of the junction. Thus, even when no voltage V is applied across the junction, the electric current can pass the barrier, and its magnitude depends on the phase difference between the two superconductors. This is the so-called DC Josephson effect. If there is a finite and constant voltage difference V applied across the junction, the phase difference $\Delta\varphi$ would follow:

$$\frac{d\Delta\varphi}{dt} = \frac{2eV}{\hbar} \tag{1.19}$$

therefore, the current would oscillate with frequency $\omega = 2eV/\hbar$. This is the so-called AC Josephson effect.

The Josephson junction is a weakness in the superconducting density, which can be achieved in different ways. An insulating layer between the superconductors was originally proposed, but a normal metal layer weakens the superconductivity too by the so-called proximity effect[2], as it does narrow constriction in the superconducting material [27].

The Josephson junctions have been used in ultrasensitive voltmeters and magnetometers [23].

The SQUID

As already mentioned, a SQUID consists of a superconducting loop with two Josephson junctions as depicted in figure 1.6. In this schema, the Josephson junctions are constrictions in the superconductor, like the scanning SQUIDs used in the following chapters. In a

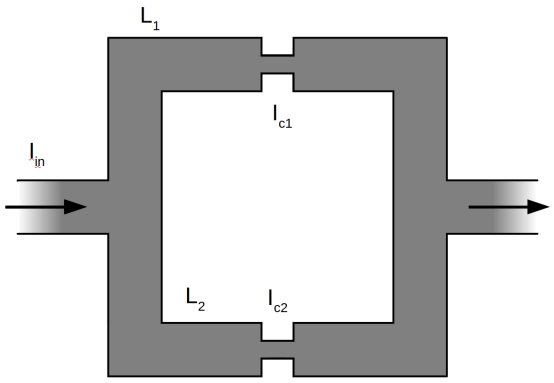

Figure 1.6: *Schema of a SQUID: there are two branches (top and bottom), each has a constriction which acts as Josephson junction with a critical current I_{ci} and an inductance L_i.*

SQUID, we have always two branches and each of them has a Josephson junction with a critical current I_{ci} and an inductance, L_i. Therefore, the current going through a Josephson junction is given by eq. 1.18: $I_i = I_{ci} \sin(\varphi_i)$, where φ_i now means the difference of phase in each junction. Then we can express the total current as:

$$I_{total} = I_1 + I_2 = I_{c1} \sin \varphi_1 + I_{c2} \sin \varphi_2 \tag{1.20}$$

[2] When a superconductor is in contact with a metal layer, Cooper pairs diffuse into the normal metal.

and the total flux of the device as:

$$\Phi = \Phi_{ext} - L_1 I_1 + L_2 I_2 \tag{1.21}$$

where $\Phi_{ext} = B_{ext} S_{SQUID}$ is the external field through the SQUID loop. Using eq. 1.17, we obtain the following phase relationship:

$$\underbrace{\varphi_2 - \varphi_1}_{Josephson\ term} + \frac{2\pi}{\Phi_0}(\Phi_{ext} + L_2 I_2 - L_1 I_1) = 2\pi n \tag{1.22}$$

where we have added the Josephson current term.

Now, we can set a global inductance $L = L_1 + L_2$ and consider that both junctions are identical: $I_{c1} = I_{c2} = I_{c0}$. Plugging this into eq. 1.22 yields

$$2\pi n = \varphi_2 - \varphi_1 + f + g \sin\varphi_2 - h(\sin\varphi_2 + \sin\varphi_1) \tag{1.23}$$

with $f = 2\pi\Phi_{ext}/\Phi_0$, $g = 2\pi L I_{c0}/\Phi_0$ and $h = 2\pi L_1 I_{c0}/\Phi_0$. In the symmetric case ($L_1 = L_2$), $h/g = 1/2$.

In order to obtain the critical current of our SQUID, eq. 1.23 has to be solved for one variable. Plugging the result into eq. 1.20 and maximizing the allowed current yields $I_c(\Phi_{ext})$. In the case of negligible inductance, we obtain the famous equation:

$$I_c(\Phi_{ext}) = 2I_{c0} \left| \cos \pi \frac{\Phi_{ext}}{\Phi_0} \right| \tag{1.24}$$

The results for the symmetric case are traced in fig. 1.7 for different g values. The $I_c(\Phi)$ modulation is maximized for a SQUID with no inductance. As we will see later, the scanning SQUID is asymmetric: $L_1 \neq L_2$. The arcs are tilted to one side so that one side is longer than the other one.

In this section I deduced the modulation of the critical current of a SQUID from superconducting basics. This shows that $I_c(\Phi)$ is periodic and depends on the symmetry of the SQUID.

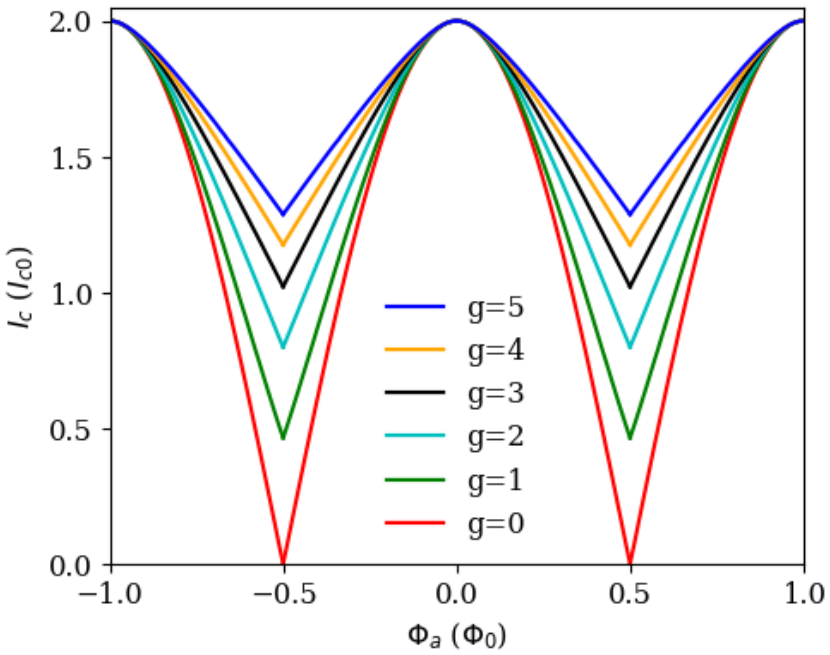

Figure 1.7: *Results of the numerical calculations of the I_c over Φ characteristics for symmetric SQUIDs ($g = 2h$), identical junctions $I_{c1} = I_{c2} = I_{c0}$ and $g = 2\pi L I_{c0}/\Phi_0$. Maximal modulation is achieved for $g = 0$, when neglecting the inductance of the SQUID.*

1.2.4 BCS

Up to now, many aspects of superconductivity have been solely explained by the existence of a macroscopic wavefunction. This assumes that the superconducting state is coherent, however in order to understand its origin, a microscopic understanding of the underlying principles needs to be developed. This was achieved in 1957 by Bardeen, Cooper and Schrieffer who presented a microscopic theory of superconductivity [7, 8]) in which electron pairs (Cooper pairs [12]) play the role of the superconducting charge carrier.

The base of this theory is the existence of an attractive potential, which will create an instability in the Fermi sea. Within the picture of the BCS theory, the electron-phonon interaction is usually considered as the attractive potential: an electron interacts with the nearby positive charges of the lattice, which will modify the potential that another electron feels. Thus, this phonon-mediated interaction couples two electrons: the Cooper pair. This

pair of electrons will break and reform other pairs with other electrons continuously, so electrons can be considered permanently paired. The Cooper pair electrons, $\Psi_{\mathbf{k},\sigma}$, with opposite momentum and spin couple and create a new state with lower energy than the Fermi energy [23], separated from the Fermi level by $\Delta(\mathbf{k})$ as sketched in fig. 1.8 left:

$$\Delta_{\downarrow\uparrow}(\mathbf{k}) \propto \langle \Psi_{\mathbf{k},\downarrow} \Psi_{-\mathbf{k},\uparrow} \rangle \tag{1.25}$$

$$E(\mathbf{k}) = \sqrt{\epsilon^2(\mathbf{k}) + \Delta^2_{\downarrow\uparrow}(\mathbf{k})} \tag{1.26}$$

where $E(\mathbf{k})$ is excitation energy for a given $\mathbf{k}$. As this gap interferes with any electron excitation, several macroscopic physical properties depend on the form of this gap in the $\mathbf{k}$-space at low temperatures. An exponential behavior of these properties, e.g. the specific heat and transport measurements (current, sound, heat), indicates an isotropic and non-zero gap: $\Delta = \Delta(\mathbf{k}) \neq 0$ (see fig. 1.8 right). In the weak coupling limit, BCS theory predicts that $\Delta(T \to 0) = 1.76 k_B T_c$.

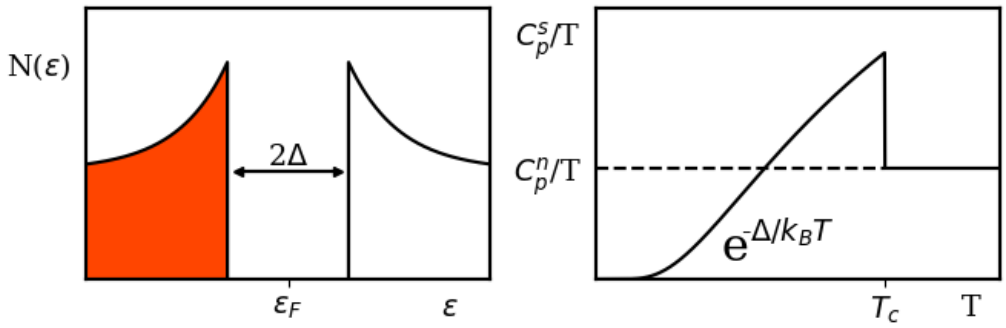

Figure 1.8: *Schema of the particle densities in a superconductor on the left. Between the occupied states (below the Fermi level, ε_F) and the unoccupied states (above ε_F), there exits the superconducting gap, Δ. On the right, a schema of the specific heat of a conventional superconductor, with exponential behavior at low temperatures and no phonon contribution.*

In 1959 Gor'kov showed that the GL theory can be derived from a constrained form of BCS theory that is well suited for the description of spatial variations [28].

The BCS theory describes many superconductors, however, there are still some that cannot be explained, such as Pb or Hb, which present $\Delta(0)/k_B T_c > 1.76$ [29]. This theory

considers several assumptions, such as a constant electron-phonon interaction, spherical Fermi surface, etc. Eliashberg considered a more realistic situation with an electron-phonon spectral function non necessarily small [30]. The original BCS theory only discusses the situation in which the density of states is fully gapped, also called s-wave, thus, Eliashberg theory can be considered as an extension of BCS theory. He also extended the BCS theory to the d-wave case. In 1968, McMillan predicted that for a phonon interaction, the highest T_c is about 30 K [31], called the McMillan limit. Now materials that display superconductivity as described by BCS theory or its extensions are called conventional superconductors, otherwise they are called unconventional superconductors [32].

1.3 Unconventional superconductivity

With the advent of BCS theory, superconductivity was considered understood (conventional superconductivity), but this changed with the discoveries of high-T_c cuprates, heavy fermion superconductors and other materials which cannot be described with BCS theory. Experimentally, they present the superconducting properties: zero resistivity, Meissner effect, critical fields H_{c1} and H_{c2}, penetration depth, flux quantification and Josephson effects. However, the electron-electron coupling is not phonon-mediated. Some material have a multiple or anisotropic gap [33]; some present coexistence of the superconducting state with magnetic fluctuations, or even with a magnetically ordered phase [34], two properties that were considered to be incompatible.

From a theoretical point of view, the Cooper pair remains the fundamental brick. The pairing is no longer mediated by phonons and several pairing mechanisms have been proposed, including magnetic fluctuations [34], but the nature of the electron-electron interaction is still an open question. These superconductors are called unconventional. They are defined as superconductors with an order parameter that has lower symmetry than the one of a conventional superconductor: $\mathcal{T} \bigotimes \mathcal{G}$ (time-reversal symmetry, $\mathcal{T}$, and point group, $\mathcal{G}$,). BCS theory does not successfully describe unconventional superconductors, therefore it's an

important research field.

1.3.1 Order parameter

Previously I introduced conventional superconductivity, where spins where always antiparallel in a singlet state. However, it is possible to consider the scenario where electrons are not necessarily in this state. For this, we have to take into account that the gap function of a Cooper pair has an orbital and a spin component:

$$\Delta_{\sigma\rho}(\mathbf{k}) \propto \langle \Psi_{\mathbf{k},\sigma} \Psi_{-\mathbf{k},\rho} \rangle \propto \mathbf{\Psi}_{\sigma\rho}(\mathbf{k})^{\dagger} \mathbf{\Psi}_{\sigma\rho}(\mathbf{k}) \tag{1.27}$$

where $\mathbf{\Psi}_{\sigma\rho}(\mathbf{k})$ is the superconducting wavefunction. Due to the fermionic nature of electrons, it must obey the Pauli's exclusion principle:

$$\mathbf{\Psi}_{\sigma\rho}(\mathbf{k}) = g(\mathbf{k})\chi_{\sigma\rho} = -g(-\mathbf{k})\chi_{\rho\sigma} \tag{1.28}$$

where $g(\mathbf{k})$ is the orbital part and $\chi_{\sigma\rho}$ is the spin part. In the case of an even (odd) orbital momentum, the spin component is antisymmetric (symmetric) under permutation of particles, thus, with odd orbital moment the spin-triplet is also possible. The BCS theory considers an angular momentum $L = 0$, which is called s-wave because of the analogy with atomic physics. The corresponding gap has a non-zero value all around the Fermi surface. In the case of higher angular momentum, the gap function has zeros for certain values of $\mathbf{k}$. These zeros are called nodes. The angular moment number, L, is related to the symmetry of the order parameter, i.e. the nodes in the gap. This is schematically presented in fig. 1.9. The existence and type of nodes define how thermodynamic properties behave at low temperatures, thus, measuring their low temperature behavior is an indirect method to measure the symmetry and nodes of the gap. The behaviors of some thermodynamic properties are given in ref. [35].

Most of the known superconductors are spin-singlet, including high-T_c cuprates and pnictides, however there exist some candidates for spin-triplet superconductivity, but none as well confirmed as ^{3}He [36]. Among the candidates for triplet pairing some are heavy fermions,

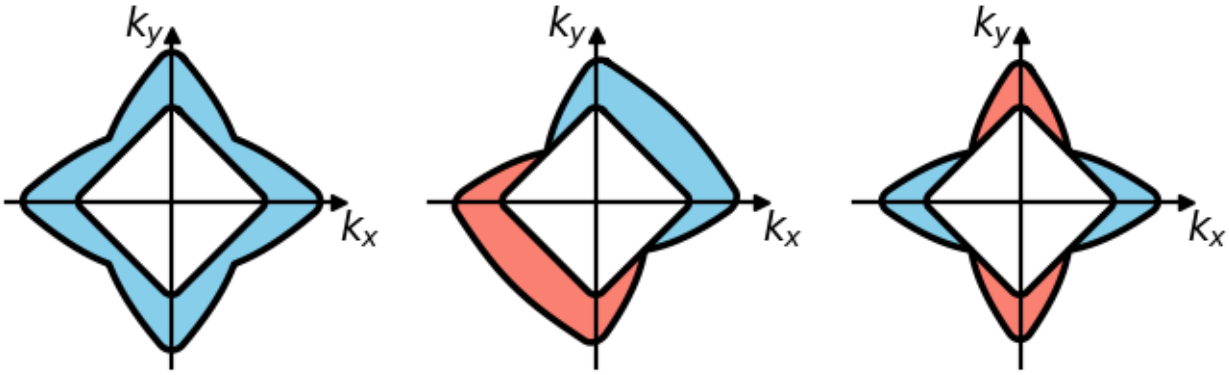

Figure 1.9: *Schemas of the gap functions for symmetries s-wave on the left, p-wave on the center and d-wave on the right. The s-wave is a conventional superconductor and the p-wave and d-wave are non-conventional superconductors. The inner rounded square is the Fermi level. The colors are the sign of the gap.*

such as UPt_3 or URu_2Si_2, others are non-centrosymmetric superconductors like Li_2Pt_3B or $CeIrSi_3$ and others are ferromagnetic superconductors such as URhGe or UCoGe [37].

In order to take into account the spin singlet and spin triplet cases, we shall rewrite the gap function in the spin space as:

$$\mathbf{\Psi}^2_{\sigma\rho}(\mathbf{k}) = \mathbf{\Psi}_{\uparrow\uparrow}(\mathbf{k}) + \mathbf{\Psi}_{\uparrow\downarrow}(\mathbf{k}) + \mathbf{\Psi}_{\downarrow\uparrow}(\mathbf{k}) + \mathbf{\Psi}_{\downarrow\downarrow}(\mathbf{k}) = \begin{pmatrix} g_1(\mathbf{k}) & g_3(\mathbf{k}) \\ g_4(\mathbf{k}) & g_2(\mathbf{k}) \end{pmatrix} \tag{1.29}$$

where $\mathbf{\Psi}_{\sigma\rho}(\mathbf{k}) = g(\mathbf{k})\,|\sigma\rho\rangle$. Then, we can simplify using eq. 1.28, so that the spin-singlet case: $g_1(\mathbf{k}) = g_2(\mathbf{k}) = 0$ and $g(\mathbf{k}) = g_3(\mathbf{k}) = -g_4(\mathbf{k})$, results in $\mathbf{\Psi}(\mathbf{k}) = ig(\mathbf{k})\sigma_y$, where σ_y is the Pauli matrix. Otherwise we can rewrite it like:

$$\mathbf{\Psi}_{singlet}(\mathbf{k}) = g(\mathbf{k})(|\uparrow\downarrow\rangle - |\downarrow\uparrow\rangle) \tag{1.30}$$

The corresponding excitation spectra is given by:

$$E_{\mathbf{k}} = \sqrt{\epsilon^2(\mathbf{k}) + |(g\mathbf{k})|^2} \tag{1.31}$$

therefore, the orbital function $g(\mathbf{k})$ holds all the information about the gap.

Using the Pauli exclusion principle (eq. 1.28), the spin-triplet case can be reduced with: $g_3(\mathbf{k}) = g_4(\mathbf{k})$, which results in:

$$\mathbf{\Psi}_{triplet}(\mathbf{k}) = g_1(\mathbf{k})\,|\uparrow\uparrow\rangle + g_3(\mathbf{k})(|\uparrow\downarrow\rangle + |\downarrow\uparrow\rangle) + g_2(\mathbf{k})\,|\downarrow\downarrow\rangle = \begin{pmatrix} g_1(\mathbf{k}) & g_3(\mathbf{k}) \\ g_3(\mathbf{k}) & g_2(\mathbf{k}) \end{pmatrix} \tag{1.32}$$

using Pauli matrices we can rewrite this equation as follows:

$$\begin{aligned} \mathbf{\Psi}_{triplet}(\mathbf{k}) &= i(\mathbf{d}(\mathbf{k})\sigma)\sigma_y = i(d_x(\mathbf{k})\sigma_x + d_y(\mathbf{k})\sigma_y + d_z(\mathbf{k})\sigma_z)\sigma_y \\ &= \begin{pmatrix} -d_x(\mathbf{k}) + id_y(\mathbf{k}) & d_z(\mathbf{k}) \\ d_z(\mathbf{k}) & d_x(\mathbf{k}) + id_y(\mathbf{k}) \end{pmatrix} \end{aligned} \tag{1.33}$$

where $\sigma = (\sigma_x, \sigma_y, \sigma_z)$ is the vector of Pauli matrices and $\mathbf{d}(\mathbf{k})$ is related to the angular parts through the equalities:

$$g_1 = -d_x + id_y \qquad g_2 = d_x + id_y \qquad g_3 = d_z$$

This vector points to the direction where the spin projection of the state is zero and the components contain the information of the orbital contribution.

The gap function from eq. 1.27 can be rewritten in terms of $\mathbf{d}(\mathbf{k})$:

$$\Delta^2_{\sigma\rho}(\mathbf{k}) \propto \mathbf{\Psi}_{\sigma\rho}(\mathbf{k})^\dagger \mathbf{\Psi}_{\sigma\rho}(\mathbf{k}) = \mathbf{d}^*\mathbf{d} + i(\mathbf{d}\times\mathbf{d}^*)\sigma \tag{1.34}$$

where * indicate the complex conjugate. Now the excitation spectra is

$$E_{\mathbf{k}} = \sqrt{\epsilon^2(\mathbf{k}) + |\mathbf{d}(\mathbf{k})|^2 \pm |\mathbf{d}^*(\mathbf{k})\times\mathbf{d}(\mathbf{k})|} \tag{1.35}$$

The term $|\mathbf{d}(\mathbf{k})|^2$ holds the information of the energetic gap. A finite value of the term $|\mathbf{d}^*(\mathbf{k})\times\mathbf{d}(\mathbf{k})|$ means a mixed state and results in two excitation branches. In the A-phase of superfluid ^{3}He, this term is finite because there is a mixture of $|\uparrow\uparrow\rangle$ and $|\downarrow\downarrow\rangle$: each pure state has a different excitation branch. This is the so-called non-unitary superfluidity. On the other hand, the A1-phase of superfluid ^{3}He is a pure state $|\uparrow\uparrow\rangle$, so this term is zero: unitary superfluidity [38].

The upper critical field H_{c2} of a spin-singlet superconductor obeys the Pauli limit. When the magnetic field is strong enough to flip a spin, spin-singlet superconductivity is broken:

$H_{c2}(T=0) = \Delta(T=0)/\sqrt{2}\mu_B$. If the superconductor does not obey this limit, then it is probably a triplet superconductor. Another technique, which measures the Pauli susceptibility of electrons, is Nuclear Magnetic Resonance (NMR). The ground state of a singlet superconductor at zero temperature has all the spins paired anti-parallel and cannot be polarized, thus the Pauli susceptibility should fall to zero as $T \to 0$ for all field directions. However, in the triplet case the spin susceptibility would be maximal when the magnetic field is aligned with the spins and zero when the magnetic field is perpendicular to them. If there is strong spin-orbit coupling, $\mathbf{d}(\mathbf{k})$ is fixed to a crystallographic axis and the susceptibility will depend on the direction of the field, however, if there is no spin-orbit coupling, spins will align with the field ($\mathbf{d}(\mathbf{k}) \perp \mathbf{H}$) and the susceptibility will be always maximal.

1.3.2 Families of unconventional superconductors

Superconductivity was considered understood by means of the successful BCS theory, at least until the discovery of unconventional superconductors such as the heavy fermion [16] or high T_c cuprates [39]. Here, I will present some families of unconventional superconductors.

The superconductivity in $CeCu_2Si_2$ was discovered in 1979 [16]. It was the first superconducting material in the heavy fermion family, which will be presented in the next section.

Before the discovery of superconductivity in $LaBaCu0_4$ in 1986 [39], oxides were not considered candidates for superconductivity. With a $T_c = 35$ K, it was the first of the so-called high-temperature superconductors. Shortly after, other cuprates superconductors were discovered with higher critical temperatures, many of them above the boiling temperature of nitrogen: $T = 77$ K [40, 41]. From a technological point of view, this was highly significant since liquid nitrogen is much cheaper than liquid helium, which is required for conventional superconductivity [40]. Up to date, $Hg_{1-x}Pb_xBa_2Ca_2Cu_3O_{8+\delta}$ holds the record of highest superconducting temperature superconductor at ambient pressure, with $T_c = 138$ K [42], and under high pressure it could go up to 164 K [43].

Unconventional superconductivity is also present in some organic materials [44]: Bechgaard salts [45], fullerenes [46], nanotubes [47], graphene [48] or the first unconventional triplet superconductor (TMTSF)2PF6[3] [45] for example.

In 2006 superconductivity was discovered in LaOFeP from the pnictide family [49]. Although their critical temperatures do not surpass 55 K, they present large critical fields [50]. It was very surprising to find that some of them contain magnetic elements, such as the iron-based superconductors.

The mechanisms leading to superconductivity in these superconductors are not yet understood, but magnetic fluctuations seem to play a major role.

1.3.3 Heavy fermions

As previously mentioned, Steglich *et al.* discovered bulk superconductivity in the first superconducting member of the heavy fermion family: $CeCu_2Si_2$. Due to magnetic correlations, the effective mass of the electrons of these materials is about 100 - 1000 times larger than the free electron mass. For the same Fermi energy, this means that the Fermi velocity is drastically reduced compared to the one of a free electron. The phonon-mediated interaction of the conventional superconductors is only possible because of a retarded interaction between the particles and the phonons, therefore heavy fermions are not fast enough for this interaction. This is why they are unconventional superconductors [23].

The heavy fermions materials are intermetallic compounds formed with heavy elements such as lanthanides (Ce, Yb, ...) or actinides (U, Pu, Np, ...). In these materials, the partly filled f-electron shells may be localized and their interaction with other electrons can be explained by the Kondo model [60]. This model describes the interaction of conduction electrons with a localized magnetic moment (originally this was an impurity, in our case it is the f-electron shell). Above the Kondo temperature, T_K, the coupling between them is weak and therefore the impurity is slightly screened giving rise to paramagnetic behaviors, below T_K the conduction electrons are strongly coupled with the localized moment, screening it

[3] (TMTSF)2PF6 stands for di-(tetramethyltetraselenafulvalene)-hexafluorophosphate.

Compound	$T_c(K)$	Comment	Reference
$CeCu_2Si_2$	0.65		[16]
UBe_{13}	0.9	spin triplet, complex phase diagram	[51, 52]
UPt_3	0.55	3 superconducting phases. AF below 5 K	[53]
URu_2Si_2	1.5	"Hidden order" magnetic phase below 17.5 K.	[54]
UPd_2Al_3	2.	AF below 14 K	[55]
UNi_2Al_3	1.	AF below 5 K	[56]
$CeCu_2Ge_2$	0.64	Under pressure. AF at p_{amb}	[57]
UCoGe	0.65	F	[58]
UGe2	<1	Under pressure. F at p_{amb}	[59]

Table 1.1: *Some heavy-fermion superconductors with the critical temperatures, a comment and their references. AF stands for antiferrromagnetic and F for ferromagnetic.*

and resulting in antiferromagnetic behaviors [61].

The f-electron states of different atoms can interact directly or indirectly depending on the overlapping of their wavefunctions (Hill's limit) [62]. Below this limit (short interatomic distances), the electronic distributions are spread (delocalized f-electrons) and may lead to direct interactions. Otherwise, the f-electron shells are well localized and the interaction may be mediated by conduction electrons. This is the so-called RKKY interaction. The resulting energy can be positive or negative depending on the value of $k_F R$, where k_F is the Fermi wavevector and R the distance between the f-electron shells, resulting in a ferromagnetic or antiferromagnetic ground state. Therefore, the chemical doping or the application of pressure could change the ground state of the material.

The competition of Kondo and RKKY interactions was first described by Doniach [63]. At $T = 0$, transitions are no longer driven by thermal fluctuation, therefore they must drive by quantum fluctuations: quantum phase transitions. These new transitions are driven by modifying other quantities than temperature, such as pressure, magnetic field or chemical doping. When quantum fluctuations overcome the thermal ones, macroscopic collective states arise, such as heavy fermion behavior or ^{3}He superfluidity.

^{3}He presents non-conventional superfluidity, which is mediated by magnetic fluctuations. By applying magnetic field, A-phase (antiferromagnetic state) can transit to the A1-phase

(ferromagnetic state) [36]. Analogously, the Cooper pairs in heavy-fermion superconductors are believed to be formed by magnetic fluctuations, as the phase diagram usually contains magnetic phases in addition of the superconductivity [53–59].

1.3.4 Unconventional superconductivity in UPt_3

The unconventional superconductivity of the UPt_3 and the underlying physics are a fascinating challenge for theorists and experimentalists. The normal state of the material appears to behave as a Fermi liquid with large renormalized effective electron masses (heavy fermion), attributed to the presence of spin fluctuations. These electrons couple in Cooper-pairs below the critical temperature $T_c = 550$ mK [53, 64, 65]. Since the discovery of its superconducting state in 1984 by Stewart *et al.* [53], a non-trivial form of the Cooper-pair wavefunction was postulated [65]. Such a wavefunction leads to a gap function that varies on the Fermi surface.

Due to the similarity of the phase diagram, the superfluid phases of ^{3}He served as reference. In the normal state, ^{3}He is paramagnetic and its specific heat has a contribution due to spin fluctuations. In the p-T phase diagram, there are two superfluid phases: the A phase (spin triplet with parallel spins) at high temperatures (2 mK) (Anderson, Brinkman and Morel) and the B-phase (spin triplet) (Balian and Werthamer) at lower temperatures. In addition, under magnetic fields the A-phase splits into the A and the A1 phase [36]. Superfluid ^{3}He has a rich phase diagram with complex patterns as presented in fig. 1.10(a), thus, the rich phase diagram of UPt_3 (see fig. 1.10(b)) is expected to have its origin in similar symmetry breaking phenomena.

Theory

The phase diagram of UPt_3 in the T-H plane consists of three superconducting phases (see figure 1.10(b)). The literature agrees that the order parameter must have multiple components in order to describe the phases [65, 68–71], but there are still open questions, such as its symmetry or the nature of the nodes. Angled-resolved experiments [72–74]

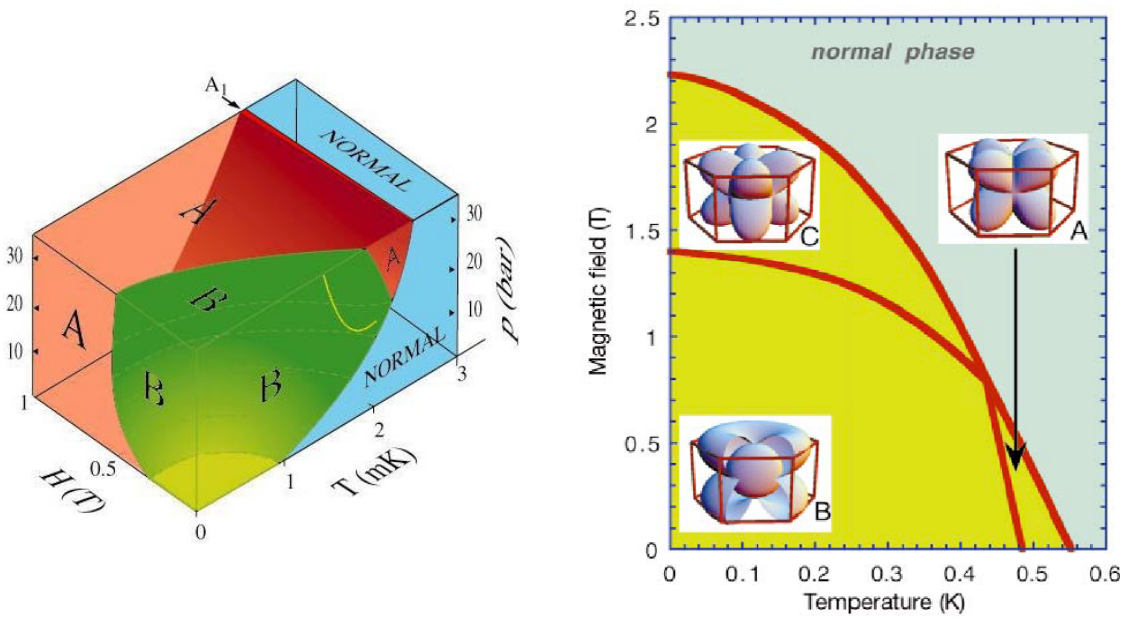

(a) (b)

Figure 1.10: *In (a), p-T-H phase diagram of ^3He. Figure reused from ref. [66]. In (b), the T-H phase diagram of UPt_3 with the three superconducting phases and their order parameters for $H \parallel c$ as presented by Huxley et al. [67].*

and power-law behavior analysis of different properties such as ultrasound attenuation [75], thermal conductivity [76], heat capacity [77] or nuclear spin relaxation rate [78] shed light onto these questions, however, no complete consensus of the theoretical description has yet been achieved.

One of the principal school of thought proposes an order parameter belonging to a strong spin-orbit coupling two-dimensional representation of the point group D_{6h} [4]. Among the possibilities (see table 1.2), the complex representations E_{1g} (spin singlet) [79–81] and E_{2u} (spin triplet) [38, 68, 82] are considered. The ground state of these descriptions is degenerate because the energy for complex conjugates is equal, therefore two possible states can be realized. As described by a single representation, the two critical temperatures should coincide, but there are three different phases, thus, the degeneracy should be lifted

[4] This representation is characterized by a weighted sum of independent gap functions: $\Delta(k) = a_1\Delta_1(k) + a_2\Delta_2(k)$. In A-phase, the coefficients (a_1, a_2)=(1, 0), in the C phase (0, 1) and in the B-phase (1, ±i).

by a symmetry breaking field [68, 83]. This role is often attributed to the antiferromagnetic ordering at $T_N = 5$ K [68, 84, 85].

d	Γ	$\Psi_i^{\Gamma_g}(\mathbf{k})$, $\mathbf{\Psi}_i^{\Gamma_u}(\mathbf{k})$
1	A_{1g}	$ak_z^2 + b(k_x^2 + k_y^2) + c(k_x^6 - 15k_x^4k_y^2 + 15k_x^2k_y^4 - k_y^6)$
1	A_{1u}	$ak_z\hat{z} + b(k_x\hat{x} + k_y\hat{y})$
1	A_{2g}	$(k_x^3 - 3k_xk_y^2)(k_y^3 - 3k_yk_x^2)$
1	A_{2u}	$ak_z(k_x^3 - 3k_xk_y^2)(k_y^3 - 3k_yk_x^2)\hat{z} + b(k_y\hat{x} - k_x\hat{y})$
1	B_{1g}	$k_z(k_x^3 - 3k_xk_y^2)$
1	B_{1u}	$a(k_x^3 - 3k_xk_y^2)\hat{z} + bk_z[(k_x^2 - k_y^2)\hat{x} - 2k_xk_y\hat{y}]$
1	B_{2g}	$k_z(k_y^3 - 3k_yk_x^2)$
1	B_{2u}	$a(k_y^3 - 3k_yk_x^2)\hat{z} + bk_z[(k_x^2 - k_y^2)\hat{y} - 2k_xk_y\hat{x}]$
2	E_{1g}	k_zk_x,k_zk_y
2	E_{1u}	$\hat{z}k_x$,$\hat{z}k_y$; $k_z\hat{x}$,$k_z\hat{y}$
2	E_{2g}	$k_x^2 - k_y^2$,$2k_xk_y$
2	E_{2u}	$\hat{z}k_z(k_x^2 - k_y^2)$,$2\hat{z}k_zk_xk_y$; $k_x\hat{x} - k_y\hat{y}$,$k_x\hat{y} + k_y\hat{x}$

Table 1.2: *Basis functions of even (S=0) and odd (S=1, strong spin-orbit coupling) representations of the point group D_{6h}. In two-dimensional states, functions are separated by commas. Semicolons separate states of the same representation.*

Another school proposed a spin-triplet scenario with weak spin-orbit coupling (see table 1.3) [74, 86, 87]. The spin vector $\mathbf{d}$ can align along any direction and the spatial part can transform according to any of the odd-parity representations of the point group (one or two dimensional). As in the strong spin-orbit scenario, the splitting of the zero field transition is addressed through a coupling of superconductivity and magnetism.

Other hypotheses involving two separate representations were also proposed [88–90]. They share the characteristic features that (i) the two superconducting transitions involve non-symmetry-related gap functions and (ii) the splitting of the A-, B-phases critical temperatures is due to an accidental degeneracy, not due to the antiferromatic ordering.

d	Γ	$\mathbf{\Psi}_i^{\Gamma_u}(\mathbf{k})$
1	A_{1u}	$k_z(k_x^3 - 3k_xk_y^2)(k_y^3 - 3k_x^2k_y)$
1	A_{2u}	k_z
1	B_{1u}	$k_y^3 - 3k_x^2k_y$
1	B_{2u}	$k_x^3 - 3k_xk_y^2$
2	E_{1u}	k_x,k_y
2	E_{2u}	$k_z(k_x^2 - k_y^2)$,$2k_xk_yk_z$

Table 1.3: *Basis functions of odd (S=1, weak spin-orbit coupling) representations of the point group D_{6h}. The vector of these basis functions is not fixed by the crystallographic axis. In two-dimensional states, functions are separated by commas.*

Normal state

UPt_3 becomes superconducting at a temperature around 550 mK [5] [53, 64, 65]. Above this temperature, the specific heat capacity can be described by the spin fluctuation form: $C = \gamma T + \beta T^3 + \delta T^3 \log(T)$ [53, 92]. The cubic term is related to phonons, with a Debye temperature of $\sim$ 210 K (close to the one of pure platinum: 230 K) [93]. The logarithmic term corresponds to the contribution of spin fluctuations. The large coefficient of the linear term, $\gamma \approx 430$ mJ/K^{2}mol (see fig. 4.2), indicates a large effective electron mass, these are the so-called heavy-fermions[6]. UPt_3 is a good example: it behaves qualitatively as a Fermi liquid, but the effective masses are much larger than the free-electron mass [65].

The energy bands of UPt_3 are composed of U $5f$ orbitals hybridized with Pt orbitals [98]. ARPES and de Haas-van Alphen experiments were performed [97–102, 102] and multiple sheets that cross the Fermi energy were found, some of them due to spin-orbit splitting [98,

[5] The superconducting critical temperature, T_c, varies 500 - 550 mK depending on the sample [53, 91], however the second transition always happens 50 mK below this temperature [65].

[6] The effective mass of the electrons of a heavy fermion system amounts to 10^2-10^3 times the free electron mass [94]. This effective mass is present in several thermodynamic variables, such as the specific heat or magnetic susceptibility [65, 95]. These compounds present a variety of ground states: superconductivity in $CeCu_2Si_2$, UBe_{13}, and UPt_3, antiferromagnetic order in U_2Zn_{17}, and UCd_{11}, and no order at all in $CeAl_3$ and $CeCu_6$ [96]. They all share heavy elements such as cerium and uranium, which suggests the importance of the interplay of f-electron bands near the Fermi surface, i.e. a strongly interacting electron system [53, 97]

103–105]. Theoretical scenarios were proposed to describe them, such as a fully itinerant 5f electron [106] or a partially localized 5f electron states [103], but none of them describes this compound satisfactorily.

In UPt_3, these heavy itinerant electrons carry charge and heat anisotropically, with conduction along the c axis always higher than perpendicular to it. The electrical resistivity for currents along each of the two high-symmetry directions, $J \parallel c$ and $J \perp c$, presents an anisotropy ratio of about 2 for temperatures up to 300 K: $\rho_\perp \approx 2\rho_\parallel$ with values of $\rho_\perp(300\text{ K}) = 240\ \mu\Omega$ cm and $\rho_\parallel(300\text{ K}) = 120\ \mu\Omega$ cm [101, 107]. The low-temperature behavior is characterized by a well-defined T^2 law for both directions up to a temperature of about 1.5 K, and for low fields ($\mu_0 H < 10$ mT and $J \parallel c$) and low temperatures, resistivity behaves linearly with the magnetic field: $\rho(T, H) = \rho_0 + aH + AT^2$, which is probably the first indicator of time-reversal symmetry breaking [65].

The AC susceptibility of this compound was measured by Frings *et al.* [108] for fields parallel and perpendicular to the c axis. The $T^3 \log(T/T^*)$ behavior indicates spin-fluctuation phenomena. Measuring the spin susceptibility using the Knight shift of NMR, the anisotropy in the basal plane was later confirmed by Tou *et al.* [109]. The spin susceptibility main features are (i) a large value at $T = 0$ K, (ii) a weak temperature dependence in the range ($T < 2$ K), (iii) an important anisotropy (larger response for field in the basal plane), and (iv) a peak in χ_{xx} at 20 K, which can be explained by van Vleck and Pauli contributions and energy bands splitting due to the crystal field [65].

The magnetic fluctuations were investigated by Aeppli *et al.* [64, 110] using elastic and inelastic neutron scattering. Moments on nearest-neighbour sites become correlated antiferromagnetically below about 20 K. Below 5-6 K, an elastic component of the magnetic correlations was found, i.e. a static antiferromagnetic order sets in the basal plane [64, 111–113]. However, low-energy probes, such as NMR or μSR, fail to detect it [67, 70, 78]. Some authors point out that the antiferromagnetic moments may be fluctuating in time [71, 109, 113, 114].

Superconducting state

The superconductivity in UPt_3 was discovered in 1984 with resistivity, specific heat and AC susceptibility measurements [53]. As crystal quality was improved T_c rose, though the superconducting transition remained broad [115], this was recognized to be intrinsic, as it was later confirmed by resolving the double transition by specific heat and thermal expansion measurements [84, 94, 116]. Three different superconducting phases were identified based on specific heat and ultrasonic attenuation measurements and widely confirmed [94, 117–119]. The three phases are referred as A-, B- and C-phase in the following of the manuscript according to fig. 1.10(b). The multiple superconducting phases in the phase diagram are only possible if the superconducting order parameter of this compound has unconventional symmetries. Furthermore, due to the momentum-dependent inter-f-electron potential, the unconventional symmetry is likely caused by a mechanism different from the electron-phonon interaction of conventional superconductivity [32, 65]. Moreover, since specific heat behavior was described by the spin fluctuations form, it is natural to think that the pairing is likely driven by exchange of spin fluctuations.

The specific heat measurements of Brison *et al.* on a high quality single crystal [91] exhibit the fingerprints of the superconductivity: the onset of superconductivity at 500 mK, the appearance of a second transition at a slightly lower temperature and the roughly linear decrease in C/T with temperature. As the transitions become sharper and sharper with increasing the sample quality, up to the order of a width of $T_c/100$. The difference between the two T_c at zero field, ΔT_c, remains remarkably invariable [65], which indicates the intrinsic nature of the double transition. Moreover, the T^2 dependence of specific heat at low temperatures indicates the existence of nodes in the structure of the order parameter.

The curve of $H_{c2}(T)$ does not follow the usual BCS behavior. It presents a kink at the tetracritical point at which the three superconducting phases join the normal phase (see fig. 1.11(a)). The magnitude of $H_{c2}(0)$ is large compared to T_c because of the huge effective masses, however, no model describes $H_{c2}(T)$ over the whole range of temperatures [72, 75].

The upper critical field H_{c2}(T) of UPt_3 presents an important anisotropy, as measured by various authors [65, 75, 120]. On the other hand, the anisotropy of the lower critical field $H_{c1}(T)$ is not that well established. It was measured by Zhao *et al.* and Shivaram *et al.* [121, 122], but not detected by Vincent *et al.* [123]. Most of the measurements present a sudden increase of the slope at a certain temperature, T_{c*}, which varies from 50 to 150 mK below T_c (see fig. 1.11(a)) [121–123]. This kink evidences an increase of the condensation energy at this temperature, that may be related to the A-B phase transition [123].

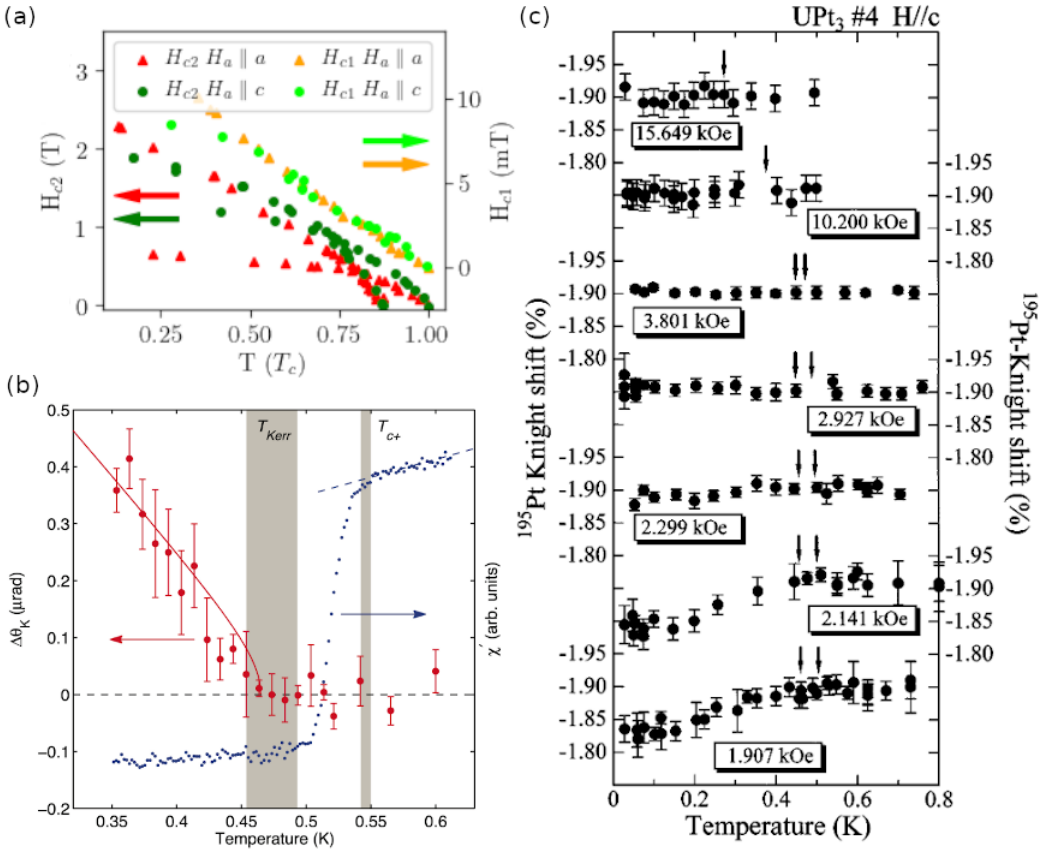

Figure 1.11: *In (a), the upper and lower critical fields. In green and red, the upper critical fields for H ∥ c and H ∥ a respectively obtained by ultrasound measurements carried out by Adenwalla et al. (T_c = 497 mK) [119]. The transition between A- and B-phases is also measured by this probe. In light green and yellow, the lower critical field for H ∥ c and H ∥ a respectively obtained by magnetization measurements carried out by Zhao et al. (T_c = 542 mK) [122]. In (b), the polar Kerr angle measured by Schemm et al. along with the susceptibility [124]. In (c), the spin susceptibility (Knight shift) measured by Tou et al. [125].*

The pressure-temperature phase diagram was studied by a number of groups [126–129]: the two transition temperatures are suppressed by the application of pressure (more importantly on the c axis [128]) and they converge into one single line between 3 and 4 kbar. The phase diagram lines do not cross at that point but merge to a single transition line thereafter. This degeneracy strongly suggests that the two transitions at ambient pressure are not close by coincidence [127].

Theoretically it is expected that chiral domains, if they exist, would hold a magnetic moment and break time-reversal symmetry (TRS). De Roetier *et al.* [71] did not observe any change in the μSR signal while crossing the A-B phase transition, thus it was concluded that the B-phase of UPt_3 did not present any magnetic moment. Polar-Kerr effect was also believed to be sensitive to the breaking of TRS, thus Schemm *et al.* [124] used this probe to rexamine UPt_3 and showed a shift in the angle of polarization when warming the sample from the B- to the A-phase (see fig. 1.11(b)). However, a non-zero polar-Kerr angle may be measured in a compound with broken TRS in presence of an external magnetic field and in a chiral superconductor without translational symmetry [130]. In vicinity of a DW of a chiral superconductor, the translation symmetry is not preserved: the order parameter changes from one domain to the other one and the gap is locally reduced [131]. Therefore, the non-zero polar-Kerr angle could be measured in UPt_3.

Spin susceptibility measurements above and below T_c present an independent or very weak temperature dependence for all magnetic field orientations[7] (see fig. 1.11(c)), which supports an odd-parity order parameter [109, 125]. Polarized neutron diffraction measured the magnetic susceptibility and evidences the temperature independence below 1 K, supporting this conclusion [132]. The field isotropy of previous measurements infers a weak

[7] In a singlet pairing superconductor, Cooper pairs do not contribute to the spin susceptibility, so the whole magnetic response is given by the excitations, i.e. normal electrons. Thus, the susceptibility will fall to 0 as $T \to 0$ because at this temperature all the particles are in the ground state (Pauli susceptibility). A more mathematical explanation can be found in ref. [38]. In the case of a triplet pairing superconductor, the $\mathbf{d}$ vector points to the k-space direction where the spin projection is zero. If there's strong spin-orbit coupling, the susceptibility should fall to zero when the field is applied along the $\mathbf{d}$ vector. On the other hand, if there is a weak spin-orbit coupling, the spins of the Cooper pairs will follow the field direction, i.e. the susceptibility does not change.

spin-orbit coupling at low fields, thus, the **d** vector seems to align freely above a field around 0.2 T [109, 125, 133, 134].

The symmetry of the order parameter is still an open question. Angle-resolved experiments, such as AC resistivity [72], critical current [73] or thermal conductivity [74], disagree, claiming 6-fold, 4-fold and 2-fold symmetries respectively. Although the experiments do not agree in the symmetry of the A- or C-phase order parameter, they do in the existence of nodes at the poles [72, 74, 135–137]. In the case of the B-phase, the order parameter seems invariant under azimutal rotations [72–74, 87, 138].

Chapter 2

Experimental Setup

The Scanning SQUID Microscope (SSM) was designed to scan and image weak magnetic signals, especially vortices in superconductors at very low temperatures. The high resolution needed for this task was achieved using microSQUIDs. These probes are relatively easy to fabricate in comparison to more advanced SQUIDs or Hall probes and the required electronics were already in the laboratory. In order to operate the microscope at very low temperatures it is placed in a dilution refrigerator.

The microscope uses a tuning fork for near-field regulation in order to maintain a small SQUID-sample distance. This is a prerequisite for high spatial resolution. The sample platform has a scanning range of 71.6 μm x 54.7 μm. For coarse movements in the xy plane we use Attocube motors and a home-made piezo motor for the z direction.

The present setup was initially developed by D. Hykel and further improved by Z. S. Wang and myself. To give a small insight I will present it in four sections. In sec. 2.1, I will explain how a SQUID is fabricated and how we measure the field with our probes and in sec. 2.2 I will illustrate and briefly explain the cryostat used in the experiences. Then, the scanning height regulation will be described in sec. 2.3, in particular the tuning fork, the height regulator and the regulation. Next, I will present the scanner for fine movements in xy plane in sec. 2.4 and for coarse movement in sec. 2.5. The used electronics are embedded in the corresponding sections, a schema of the whole electronic setup is presented in fig. 2.9.

2.1 MicroSQUIDs

One of the crucial parts of the microscope is the microSQUID. Fundamental concepts of SQUIDs have already been introduced in sec. 1.2.3 so I will focus here on technical information of the fabrication, measurement and magnetic sensitivity of microSQUIDs.

2.1.1 Fabrication

The aim of the fabrication is to place the SQUID loop as close to the tip of the SQUID chip as possible. The fabrication of this chip is well mastered. The pattering is undertaken at the laboratory (T. Crozes at Nanofab, Néel Institut-CNRS) generating hundreds of SQUIDs on each wafer. Now I present how we achieve our aim:

1. Alignment marks: a silicon wafer is spin-coated with PMMA[1], then the electron beam draws the marks, destroying the polymer chains. After development, gold is evaporated and then the remaining PMMA is lifted-off.

2. SQUID deposition: the marked silicon wafer is spin-coated with PMMA. The electron beam draws the SQUID pattern. Once developed, 30 nm of aluminum is evaporated. Then, the remaining PMMA is removed with acetone. See fig. 2.1 left.

3. After a realignment with the gold marks, a Laser writer (Heidelberg Instruments) patterns the etch mask in a 2.5 μm thick S1818 resist.

4. Inductive Coupling Plasma Etching: 75 μm of Silicium are etched using a Bosch process at IRAM[2] (Saint Martin d'Heres), courtesy of A. Barbier, E. Driessen and K. Schuster. After the etch the microSQUID is situated at the edge of the chip (see fig. 2.1 right).

5. Diamond cut for creating individual SQUID chips. This steps is carried out by J. Goupy, Néel Institut-CNRS and I. Pheng at CIME Minatech.

[1] Poly (methyl methacrylate)
[2] Institut de Radioastronomie Millimetrique - CNRS(France)/MPG(Germany)/IGN(Spain)

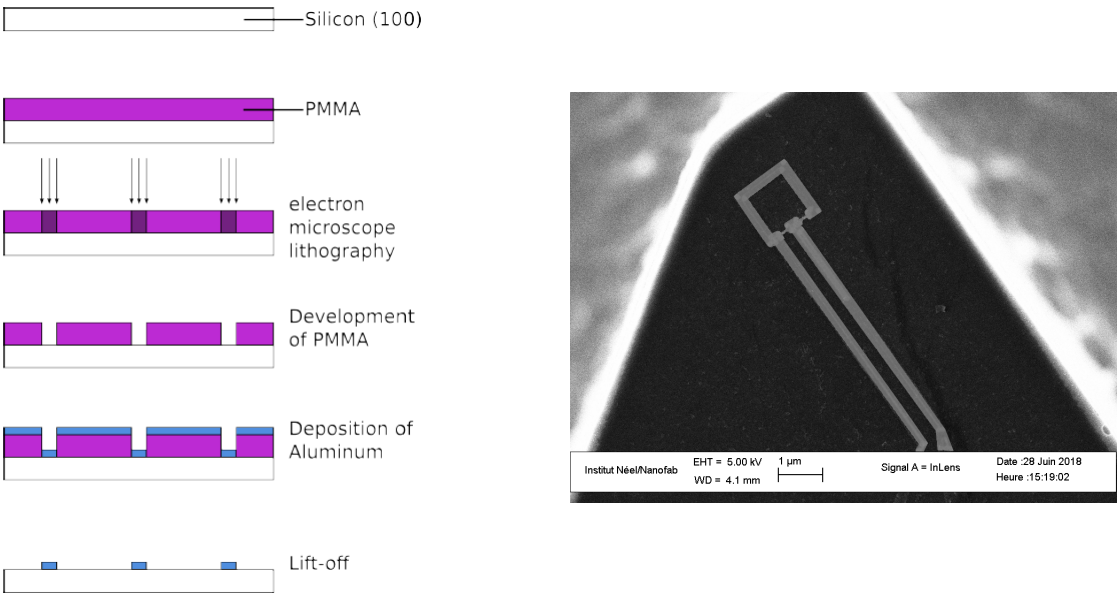

Figure 2.1: *On the left, schematics of the fabrication process. On the right, a SEM image of a SQUID of 1x1 μm^2 of inner loop. Microbridges of 50 nm large and 200 nm long. The outer light grey region is the deep etched ($\sim$ 50 μm below the SQUID).*

2.1.2 Measurement

Critical current measurement

The scanning SQUIDs consist of one aluminium layer, which is one strength in the fabrication process [139, 140]. However, these SQUIDs are thermally hysteretic (see fig. 2.2 left) [141]. When a current bias reaches the junctions critical current the junctions transit to normal state and they dissipate enough to turn the whole SQUID normal. The only way to get back into the superconducting state is to switch off the current bias.

In order to measure this SQUIDs critical current we have to inject a ramping current in order to reach the critical value and cut it when a voltage is detected. We measure the time of the ramp from which we deduce the critical current (see fig. 2.2 right). In order to optimize this measurement method, we can start the ramp at a custom current, I_p.

The flux dependence of the critical current is valid for any temperature below the T_c, but the critical current depends on the temperature. At temperatures low enough we can

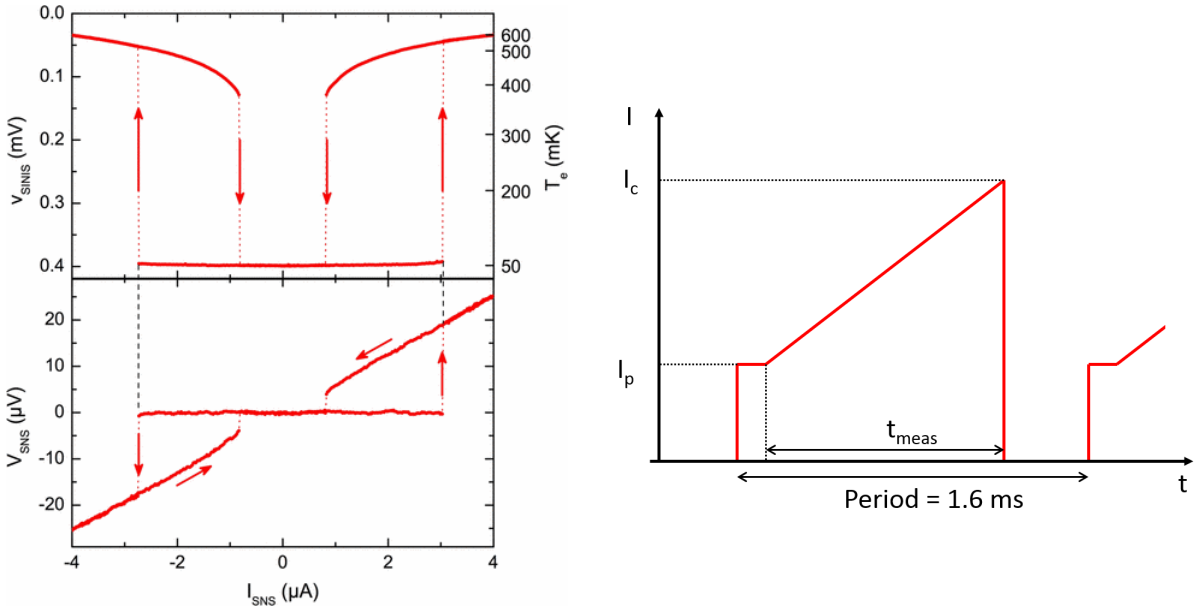

Figure 2.2: *On the left, the voltage-current curve for the Al/Cu/Al (S-N-S) junction [141]. Thermal and voltage hysteresis are represented. On the right, the current ramp is sketched used to determine the critical current of the microSQUID junction (S-s-S). Each measure takes about 1.6 ms, a readout frequency of around 600 Hz.*

consider that I_c does not depend on T, therefore the SQUID is operated at low temperatures for minimizing the effect of temperature fluctuations.

A custom-built Digital Direct Synthesizer (DDS) device[3] provides the interface between the computer and the SQUID electronics. The readout electronics consists of two devices more. One contains the numerical part (computer interface and timing) and the other the analog part (current source and voltage detection). One of the two leads of the SQUID is used for current biasing and the other is grounded. Via a room temperature switch we can permute injection and ground leads. Tightly screwed to the cryostat, the analog device sends a current ramp into the SQUID and simultaneously arms a trigger for a sudden change in the voltage increase at the injection lead. Such a change switches off the current. The duration of the ramp, proportional to the critical current, is stored in the buffer of the numerical part with a resolution of 25 ns (see fig. 2.2 right).

[3] developed by Julien Minet at Néel Institut - CNRS

From critical current to field

In order to transform critical current images to magnetic images we have to sweep 4 times the magnetic field produced by the room temperature copper solenoid in order to obtain a calibration curve:

(a) The magnetic field is ramped up and down at a constant rate in order to remove the Foucault currents effect. This effect implies a shift in the field proportional to variation rate. By averaging the two $I_c(B)$ curves we obtain a quasi-static $I_c(B)$ curve corresponding to the scanning situation.

(b) Two similar sweeps are required after having permuted injection and ground lead of the SQUID. Due to the asymmetry of the SQUID's inductance we can determine any field offset thanks to the crossing of both quasi-static curves, at $H = 0$ (see appendix A).

However, the periodic $I_c(B)$ presents some important disadvantages, that I will discuss using fig. 2.3:

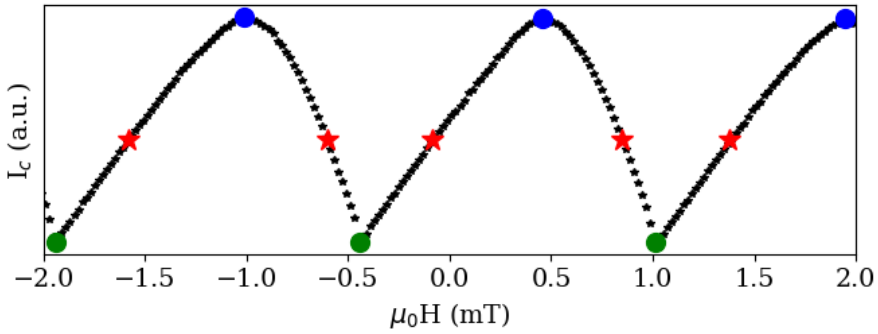

Figure 2.3: *$I_c(\Phi)$ modulation curve for the scanning SQUID. Each symbol corresponds to the same critical current. Circles are the insensitive points and the cross is a sensitive point.*

- The circles are points with the least magnetic sensitivity, called insensitive points. Going through one of these points will give rise to the uncertainty whether the magnetic field increases or decreases. Although, this is a clear disadvantage while measuring, it can be useful when making noise analysis.

- Multi-valuedness: in the figure all the red crosses have the same critical current, however they correspond to different values of flux. The field corresponding to the flux value depends on the SQUID size: smaller area, larger field period. Therefore, for small field ranges we would prefer a larger SQUID loop rather a smaller one because of the higher field sensitivity (see chapter 4) and for larger field ranges we would use an smaller loop in order to avoid crossing several modulation arcs (see chapter 3).

In appendix B I detail the process of translating the critical current to field, in particular, how I worked out the multivaluedness of the measurements. In order to avoid this problem some groups feedback their SQUIDs to keep the critical current modulation at the optimal point [139, 142].

Convolution

To attain ultimate resolution in imaging it is in general necessary to take into account effects of probe sample distance and of convolution between the probe size and the signal feature. We aim at scanning at a distance less than the SQUID diameter and less then the typical feature size (λ). We take into account the SQUID size and the scanning height when we extract quantitative values from our images.

Noise estimation

I will briefly comment on the current noise in the SQUID read-out. However, the noise of scanning microscope technique was not analyzed exhaustively.

The standard deviation (STD) of the measurement was determined mathematically from the unaveraged critical current values. We know thanks to the theorem of Shannon [143] that the noise is obtained by dividing the STD by the bandwidth, which is half of readout frequency. The lowest noise obtained in the current scanning SQUIDs is 0.2 $\mathrm{m}\Phi_0/\sqrt{\mathrm{Hz}}$ (for a SQUID with 1 $\mu\mathrm{m}^2$ of loop, this corresponds to 0.3 $\mu\mathrm{T}/\sqrt{\mathrm{Hz}}$). This flux noise corresponds to a current noise of $\sim$7 $\mathrm{nA}/\sqrt{\mathrm{Hz}}$. While scanning, the pixel value is usually the average of 30 individual measurements, then the error per pixel (at this frequency) is ~ 1 $\mathrm{m}\Phi_0$ or ~ 2

μT for a 1 μm^2 SQUID.

We can estimate the contribution of different noise sources. The thermal noise is mainly given by the room-temperature bias resistor (25 kΩ) $S_I = \sqrt{4k_BT/R} = 0.8$ pA/$\sqrt{\text{Hz}}$. The current source has 2^{16} bits, which correspond to the time of the current ramp from 30 μA to 80 μA. Therefore, the current noise due to discretisation is $S_I = \Delta I/N_{bits} = 25$ pA/$\sqrt{\text{Hz}}$. There is also some noise contribution from the shot noise measurement (due to the discrete charge of electrons), given by $S_I = \sqrt{2eI} = 4$ pA in a first order approximation [144]. Thermal noise, shot noise and discrete current source noise together are orders of magnitude lower than the measured noise.

Other sources of noise are ambient magnetic field fluctuations or due to temperature instabilities in the refrigerator and the effect in the critical current of the SQUID. In the latter case and following a GL dependence ($I_c(T) = I_c(0)(1 - T/T_c)^{1.5}$ [23, 145]) for a scanning SQUID ($T_c = 1.2$ K and $I_c^{max} = 70$ μA), temperature fluctuations of 100 μK at 300 mK results in an error of the critical current of 7.5 nA. Such thermal fluctuations could explain the measured noise.

2.2 Cryogenics

The scanning microscope has to be cooled down well below the superconducting transition temperature so that we can consider that the critical current is not affected by small changes of temperature ($T_{SQUID} = 300$ mK). In addition, samples need to be cooled down to 200-300 mK, in particular UPt_3 because of its $T_c = 500 - 550$ mK [64, 71, 124, 146]. For this purpose our experiment uses an inverse dilution cryostat[4] (see fig. 2.4 left): the lowest temperature stage is at its top while the highest temperature stage is at the bottom (so-called SionLuDi (inverse of DiLuSion)). It was developed at the CRTBT (Centre de Recherche de Très Basses Températures, today called Néel Institut-CNRS) by A. Benoit,

[4] The reader is referred to [147] for a more detailed discussion of cryogenics.

M. Caussignac and S. Pujol. There are five stages and four gold coated copper cylinders attached to the stages in order to screen the room-temperature radiation: 80 K, 20 K, 4 K and 1 K. Everything is contained in a vacuum vessel. Liquid ^{4}He is fed to the 4 K-pot from a liquid Helium dewar underneath.

The mixture is circulated by a compressor and pumps through the heat exchangers, auxiliary still, mixing chamber and main still. The ^{4}He circuit thermalizes the 4 K-pot and the incoming mixture via a circular counterflow heat exchanger. The different mixture circuits are designed to precool to different temperatures. One mixture circuit carries relatively high flow and serves to precool from 300 to 4 K the stills and the mixing chamber. Another one (1-4 K circuit) cools the dilution part down to 1.2 K. The last circuit (injection) is thermalized in the 4 K-pot and the main still before injecting the ^{3}He-^{4}He mixture into the mixing chamber. With all other circuits shut, this one allows to reach base temperature of 150 mK.

The cooling process in more detail:

1. The ^{4}He circuit cools down the 4 K-plate. Typically we use a flow rate of 10-15 l/day (liquid) or 85-125 ml/sec (gas). This corresponds to 20-30% on the gauge.

2. While the ^{4}He circuit is cooling, we circulate the three mixture circuits with a flow rate of 40 ml/s, thanks to a compressor before the entry the refrigerator. This gas is thermalized to 4 K by a ^{4}He counter flow heat exchange. Then, the gas passes through the auxiliary still, the mixing chamber and main still.

3. Once every stage is well thermalized at 4 K, we close the precooling circuit.

4. Closing the precooling circuit, we need to run two pumps in series at the exit the cryostat (roots pump and a rotary vane pump) to create a higher pressure difference between the entry and the exit. If we want to work in the range of 1-4 K, this is the final step.

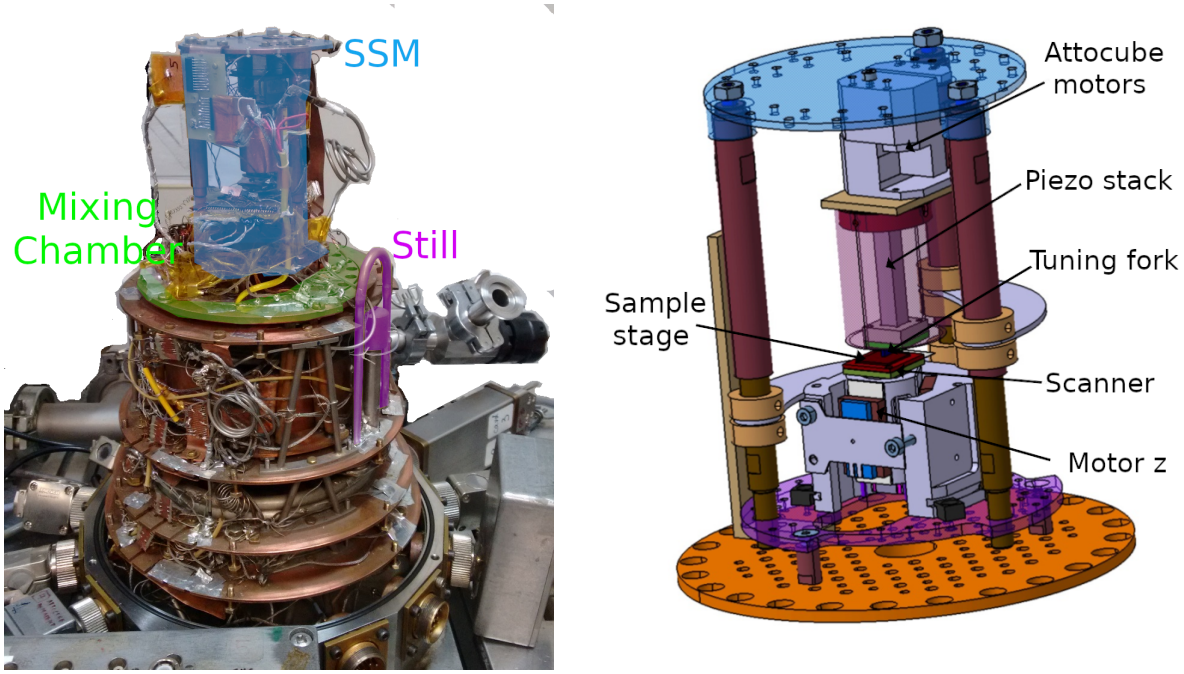

Figure 2.4: *On the left, the cryostat used for the scanning SQUID measurements. The microscope is on the top of the cryostat. We can differentiate the thermalization stages one of the stills and the wiring for the microscope. On the right, an schema of the microscope without the wiring.*

5. For lower temperatures, we need to close the 1-4 K circuit. The only mixture circuit is the injection.

6. The cooling effect under a certain temperature (600 - 700 mK in our cryostat) takes place due to separation of isotopes: one ^{3}He-rich phase and one ^{4}He-rich phase. By transferring of ^{3}He atoms from the pure ^{3}He phase to the ^{4}He-rich phase, heat is extracted from the mixing stage, so the lowest temperatures can be achieved [95].

Once we are in the temperature range where we want to work, the sample stage is partly isolated from the mixing chamber, thus the temperature can be controlled independently.

2.2.1 Thermometry

We have chosen a well-proven thermometry system developed at the laboratory: TRMC2, CRTBT. Up to 4 cards can be read simultaneously, each card can read up to 4 thermome-

ters in the 3 wires + ground configuration. One card measures the temperatures of the two stills (ruthenium oxide resistors) and the 4 K-pot (carbon resistor for lower temperatures and platinum one for higher ones). Another card measures the temperature of the mixing chamber, which has 3 different resistors: two carbon and one germanium for the mixing chamber stage. The fourth resistor is ruthenium oxide placed at the sample stage. One last card measures the SQUID temperature with a carbon resistor.

The sample' stage thermometer was calibrated in other SionLuDi refrigerator. The calibration goes down to 50 mK, thanks to a SRD[5], a CMN[6] and a well calibrated thermometer.

2.3 SQUID-sample height control

We scan the sample at the surface, therefore the regulation serves to follow the topography without scratching the probe. The whole regulation consists of the tuning fork, the lock-in amplifier that compares the response of the tuning fork with the excitation signal, the Direct Signal Processor (DSP) card that calculates the regulation loops, the DDS device that produces the excitation signal, the excitation piezo element and the piezo-z stack. Here, I will present three key elements, which are common in near-field force microscopy: the tuning fork, the height controller and the regulation.

2.3.1 Tuning Fork

The tuning fork[7] is a quartz resonator that is extremely sensitive to external mechanical forces. For this reason, it is widely used for near-field microscopy. The current that flows through it and the mechanical vibration are related [149], thus exciting the tuning fork mechanically (electronically) produces the current (vibration). The frequency spectrum of the output signal is characterized by a Lorentzian peak and a phase shift between the

[5] The Superconducting Reference Device SRD1000 has 13 stable reference superconducting points for thermometry between about 10 mK and 10 K [148].

[6] The CMN1000 is a precision thermometer for the range of 10 mK to 2 K using the temperature dependence of the susceptibility of powdered Cerium Magnesium Nitrate (CMN) [148].

[7] Multicomp Pro MCRJ332768F1220HOW

excitation signal and the response of the tuning fork (see fig. 2.5). At low temperatures, the quartz becomes stiffer and the spectrum is modified: the resonant frequency increases and the peak sharpens (see fig. 2.5). The spectrum is also affected when the tuning fork touches the sample: the whole spectrum shifts upwards, thus it is possible to measure the contact with the sample.

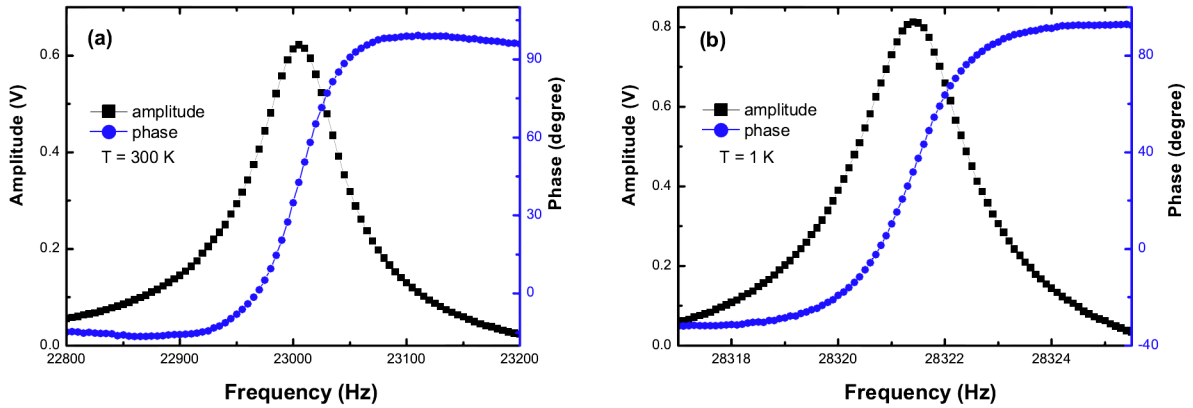

Figure 2.5: *Typical resonance curves of the tuning fork with SQUID at 300 K and 1 K. At 300 K, the resonance frequency is 23000 Hz (much lower than 32768 Hz due to gluing, and the SQUID chip) and the width of the peak is around 100 Hz. At low temperature, the resonance frequency increases (28323 Hz) and the peak becomes sharper (width of 2.5 Hz).*

In our microscope, one of the arms of the tuning fork is glued on a PCB board, and the SQUID chip is glued on top of the free arm. This naturally increases the effective mass of the oscillator and decreases the frequency and quality factor of the resonance. The SQUID chip is electrically connected with a bonding machine that uses aluminum wire of 25 μm of diameter to the SQUID pads by using ultrasound vibrations. This step can also affect the resonance of the tuning fork. The PCB board that contains the tuning fork is screwed in direct contact with the piezo element that excites mechanically[8] the tuning fork, so the transmission is maximal without changing the exciting piezo with each new tuning fork [149].

The quality of the spectra depends on several factors, such as the quality of the glue-

[8] The electrical excitation is also possible but many vibration modes would be excited, thus one needs a more complicated electrical setup

ing, the electrical connections, the SQUID chip or the temperature. In the worst cases it becomes quite complicated, with multiple peaks, that may behave differently with temperature (shifting down in the spectra, appearing and disappearing, ...) [150]. In best of cases, there is a single and sharp peak, with large amplitude. For this reason, we use only tuning forks with a good spectrum at room temperature.

2.3.2 Piezo-z stack

The contact between the SQUID and the sample is measured by the tuning fork's resonance change. Thanks to the regulation, the height of the SQUID/tuning fork is controlled by applying a voltage to a piezo-electric stack[9]. This element of the microscope is attached between the coarse motors and the exciting piezo of the tuning fork.

Its length is 3.6 cm and its piezo-electrical expansion coefficient is 0.32 μm/V at room temperature and 0.067 μm/V at 1 K. This yields a maximal elongation of 35.2 μm at room temperature and 7.37 μm at 1 K for 110 V. This low expansion coefficient allow us to scan the surface topography with relatively high precision.

2.3.3 Regulation

The tuning fork creates a current depending on the frequency of excitation and the contact with the sample. This current is compared with the excitation signal with a lock-in amplifier (Ametek 7270 DSP). The output is read by the DSP card in order to update the regulation loops. The card will command in consequence the extension of the piezo-z stack (through a homemade amplifier) and the excitation frequency (through the DDS device). There are two proportional-integral (PI) regulation loops: one is phase-locked and the other one frequency-locked. The first loop varies the excitation frequency in order to keep the phase at the steepest part and most sensitive point of the spectra. The second loop fixes the frequency and modifies the voltage applied to the piezo-z stack (the height of the tuning fork) so that the phase and frequency correspond to the respective set points. Thus, the

[9] Piezo Ceramic, Model: P-885.90 in the z direction

topography is measurable in terms of the voltage of piezo-z stack. The whole regulation process is presented in fig. 2.6.

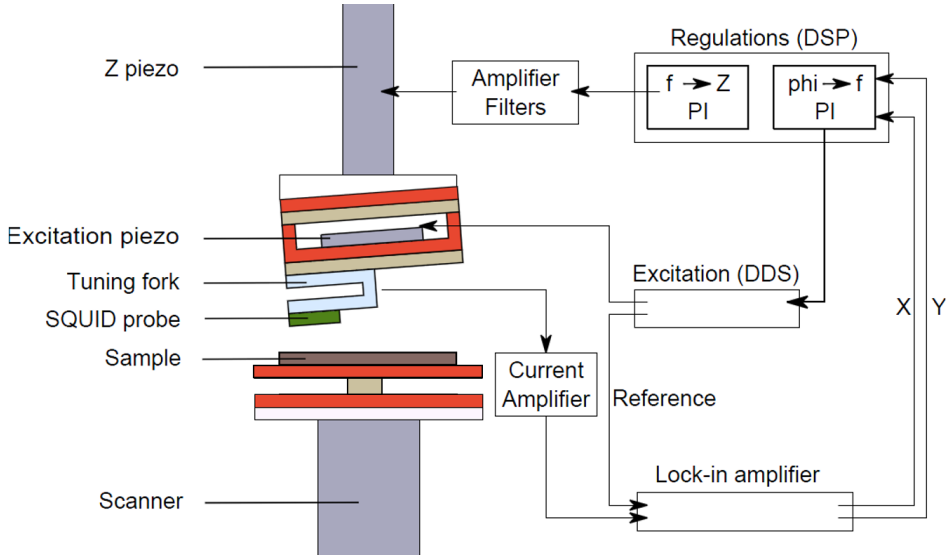

Figure 2.6: *Schematic of the regulation loops. The tuning fork is excited by a piezo-electrical actuator which is controlled by the DDS card. The signal of the tuning fork is amplified then measured by the lock-in, which send the X and Y to the DSP card. Then, the DSP card regulates the phase of tuning fork and also the piezo-z stack with two PI controllers.*

In order to start the regulation, a frequency sweep is measured to establish the frequency spectrum. Then, we select a frequency range where the phase shifts monotonically with relatively large amplitude to limit the phase-locked loop (see fig. 2.5). As the spectra will shift upwards when there is contact with the sample, we choose a set phase that is in the steepest region of the curve, and on the left of the peak, thus, if we touch the amplitude will increase. For the frequency-locked loop, we set the frequency f_{set} about 1 - 3 Hz higher than the non-touching frequency. The regulation will extend the piezo-z stack until the tuning fork feels the sample and the frequency reaches f_{set}, otherwise the piezo-z stack will extend out completely. If an important extension or retraction of the piezo-z stack is executed rapidly, the high applied voltage will heat the SQUID, consequently, a fast and fine regulation is needed.

2.4 Scanner

2.4.1 Scanner

A piezoelectric bimorph scanner is used for imaging the surface. The scanner is an assembly of 4 S-piezos that will bend under voltage application in order to move the sample over a short range (see fig. 2.7(a)-(b)).

At each cool down an image of the *chessy*[10] (calibration sample) is acquired allowing us to scale the magnetic field consistently. A calibration image of the scanner can be observed in fig. 2.7, with a scanning area of 71.6×54.7 μm^2 for a difference of 400 V applied to the electrodes[11].

The DSP card controls also the scanner. The commanding signal coming from the analog output of the card is amplified with a homemade amplifier before going into the cryostat.

2.4.2 Platform

During the internship of the second year of my Master's degree, I built a thermally isolated sample stage. Two parallel plates separated by an isolating column. Initally, the plates were made of saphire and the column of alumina because of their thermal conductivities [95], however due to thermal stress while cooling we had to change to other materials: copper plates and a Kapton cylinder as column. On the sample plate, we have attached a RuO_2 resistor for measuring the temperature, a 100 Ω resistor for heating and a thermal link to the mixing chamber (prepared to be around 5 μW/K). The aim was to heat the sample without perturbing the mixing chamber nor the SQUID (the critical current depends on the temperature). In the case of UPt_3 ($T_c = 550$ mK), a pulse to heat the sample above T_c is acceptable for the SQUID, however, scanning at 600 mK slightly perturbs the mixing chamber. Scanning $PdTe_2$ ($T_c \approx 1.55$ K) above T_c or turning normal the *chessy* (made

[10] The sample called *chessy* is a checker board of Nb on a substrate of Si. The big squares are 20 μm long and each of these squares is itself a checker board of squares of 2 μm a side. Thanks to this design, the scanner can be easily calibrated.

[11] This area corresponds to measurements in the $PdTe_2$ crystal. Due to some technical modifications, the scanning area in the UPt_3 sample is slightly smaller: 58×39 μm^2.

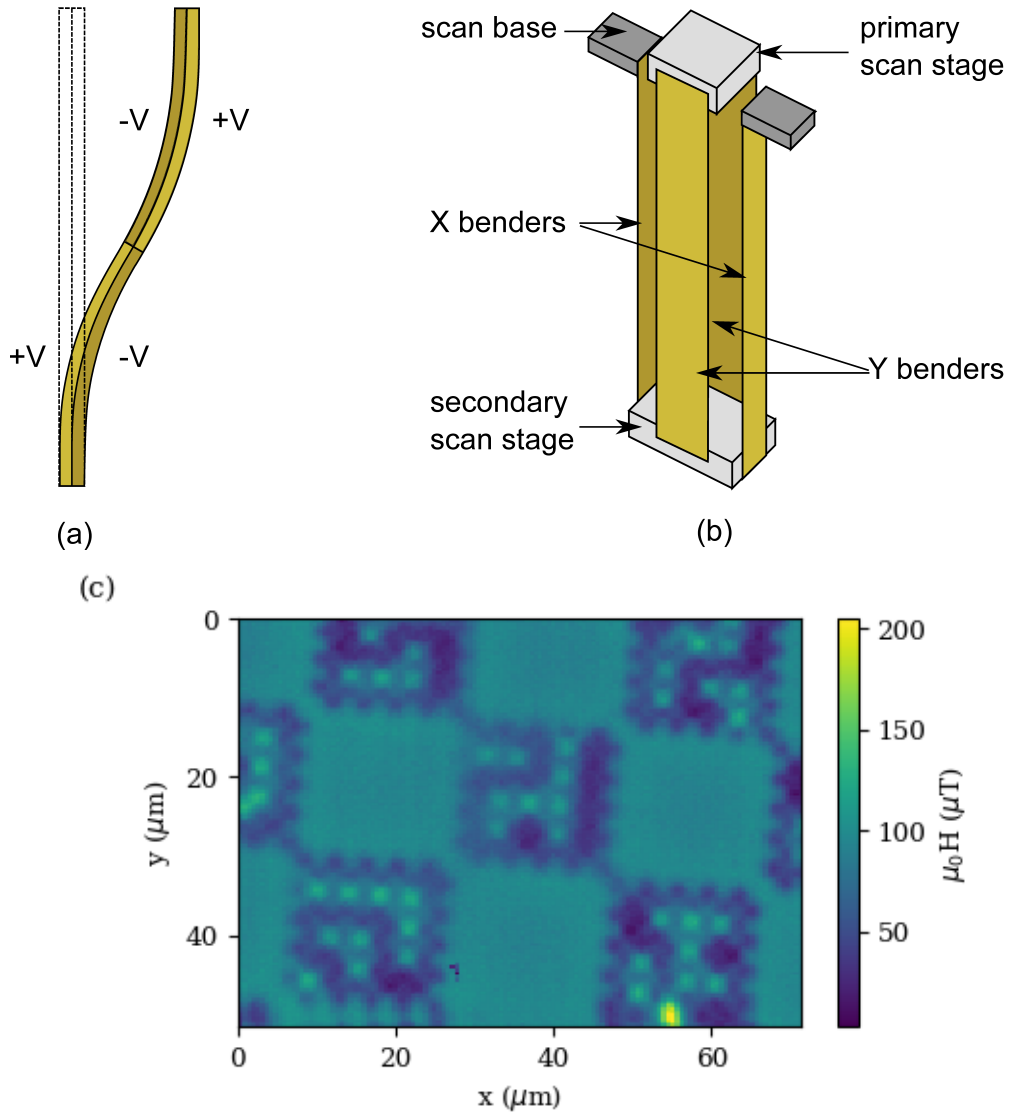

Figure 2.7: *In (a), the schema of the S-shaped scanner piezos. In (b), schema of the 4 S-shaped piezos forming the scanner. The sample stage is placed in the primary scan stage. In (c), magnetic image of the calibration sample. We call it chessy, as it is a checker board of Nb on a Si substrate. The big squares of the checker boards are 20 μm a side and the small squares are 2 μm a side. Subfigures (a) and (b) reused from ref. [151].*

of Nb with $T_c \approx 9.3$ K) strongly heats the mixing chamber and consequently the SQUID, perturbing the measurement and the refrigerator.

2.5 Coarse motors

The coarse motion can be divided to two systems: the x-y plane motors and the z axis motor.

The x-y plane motors are used to change the position on the sample or to move to other samples. In each axis, there is an Attocube motors (AN-Pxyz101LT), which is controlled via the corresponding Controller (ANC150). At low temperature, the range of these motors is around 5 mm. The typical measured samples are much smaller than the whole range, so we can choose a good spot in the sample for imaging or measure several samples within one cooling down (sample and *chessy* for example).

The z axis motor is a home-made motor inspired by the design of Sheheng Pan [152]. It consists of 6 shear piezos (EBL Products Inc., PTZ-5A) glued on a titanium base. The slider (mobile part inside the titatium base) has glued sapphire plates to make the direct contact with the piezos. A sawtooth voltage generator (Swissprobe Piezo-Motor Controller SP869) is connected to the shear piezo and can deliver peak-peak voltage of 800 V. At low temperatures, the capacitances of the piezos and their movements are greatly reduced, so high voltages are of much importance.

Position read-out

At low temperatures, the x-y Attocube motors and the Z motor do not move steadily: one single voltage pulse does not necessarily result in a motor movement. Therefore we read the displacement position using a comb capacitor (depicted in fig. 2.8). One comb fixed to the mobile part and the two others in immobile part. A 10 V alternating voltage is applied to one comb of the static part (blue in fig. 2.8) and the same signal but shifted 180° to the other comb (red in fig. 2.8). The mobile comb (magenta in fig. 2.8) is connected to a lock-in amplifier (EG&G Instruments 7220). The capacity between the mobile and immobile combs is of the order of a few pF. When the slider moves, its comb will alternate periodically to face the unshifted comb or the shifted comb. The resulting signal is an

oscillation with the same period that the combs: $\sim$ 1.5 mm. The capacitance readout changes much from room temperature to low temperature, but the shape and the relative positions to the maximum and minimum don't change. Thanks to a small misalignment of the combs, the local maxima and minima change from period to period, therefore, we can find the sample at low temperatures with the room temperature curve.

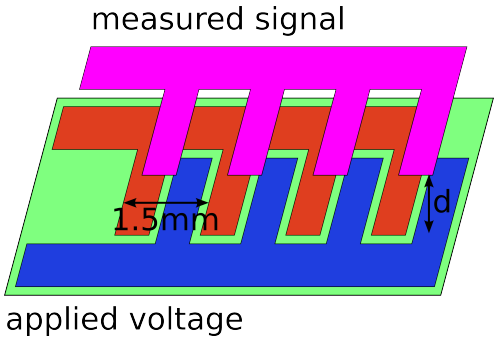

Figure 2.8: *Schematic of the comb capacitor. The two combs of the static part (red and blue) are excited with the same signal but inverse phase. When the mobile comb (magenta) moves, it will alternate periodically to face the unshifted comb or the shifted comb. The signal is measured by a lock-in amplifier. The periodicity of the combs is* $\sim$ *1.5 mm. Figure reused from ref. [150].*

2.6 Field coil

We used one copper coil, which is directly attached to the external vacuum vessel of the SionLuDi. It can provide 6.8 mT/A in z-direction. The coil is driven by a V-I converter, which can provide a maximal current of 3 A ($\sim$20 mT). The converter is controlled by an analog voltage delivered from the DSP card.

In general, Earth field is compensated with the coil, so that we can observe the Meissner effect. However, as Earth field varies with time, the point of zero field is not exact, but approximately $\pm$ 5 μT the measured value. Thus, zero field cooling will usually present some remanent flux.

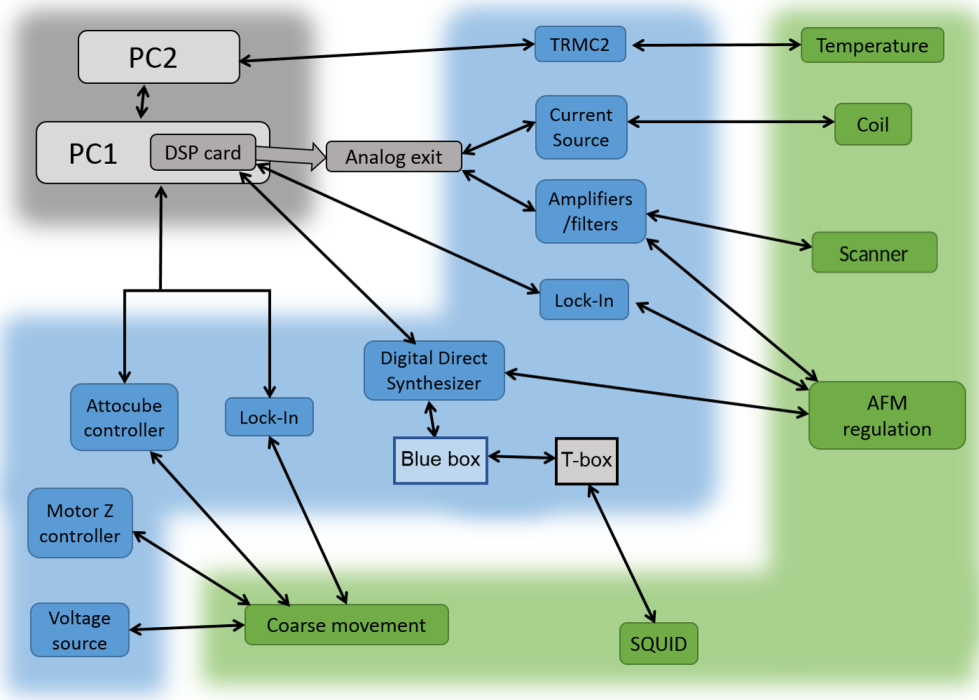

Figure 2.9: *Electronic schema: in gray background the computers that command the electronics (in blue background), that control the low temperature setup (in green background).*

I mastered the setup here presented, with which I imaged the magnetic flux distribution of two superconductor at low temperatures with a magnetic resolution 0.2 $\mathrm{G}/\sqrt{\mathrm{Hz}}$ and spatial resolution of the order of 1 μm. In the following chapters I will present the measurements of these superconductors with the microscope and their interpretation.

Chapter 3

Intermediate state in $PdTe_2$

Finding materials presenting topological superconductivity is an important challenge in today's condensed matter research. A wide range of unconventional superconductors are under scrutiny for signs of topologically protected states [153–155]. One promising family of materials is the transition metal dichalcogenides, to which $PdTe_2$ belongs. This compound becomes superconducting at a temperature $T_c = 1.6$ K [156–158]. and angle-resolved photoemission spectroscopy (ARPES) identified a tilted Dirac cone 1.6 eV below the Fermi energy (see fig. 3.1(a)), which may be the signature of a topological superconductor. The Dirac cone presents spin-polarized topological surface states [159–161], classifying this compound as a type-II Dirac semimetal [162]. Thermodynamic and magnetic bulk experiments report type-I superconductivity, which is unusual for a binary compound, however, surface probes like Scanning Tunnel Microscopy/Spectroscopy (STM/STS) [163, 164] or Point Contact Spectroscopy (PCS) [165] evidence type-II superconductivity. A magnetic scanning microscope such as the SSM shall shed light on this question.

3.1 State of the art

$PdTe_2$ has a trigonal crystalline structure similar to the CdI_2 [157, 166] formed by inserting a packed hexagonal layer of Pd atoms between every other layer of hexagonal close-packed Te atoms (see fig. 3.1(b)) [167]. The compound belongs to the space group $P\bar{3}m1$. The lattice parameters are $a = b = 4.024$ Å and $c = 5.113$ Å. The density is 8.4 gcm^{-3} and

the molar volume of 71.7 Å^3/unit cell.

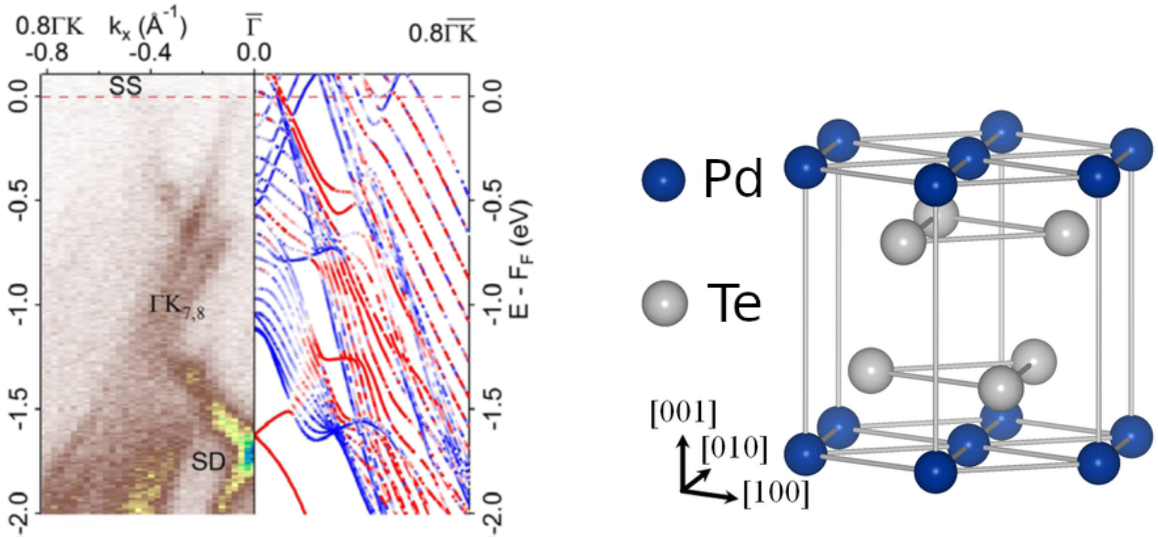

(a) (b)

Figure 3.1: *In (a), $PdTe_2$ electronic structure measured by Noh et al. [168] and the band calculation for bulk (blue) and surface (red) states. Figure modified from ref. [168]. The crystalline structure of $PdTe_2$ presented in (b) corresponds to a trigonal structure similar to the CdI_2, formed by inserting a packed hexagonal layer of Pd atoms between every other layer of hexagonal close-packed Te atoms. Figure modified from ref. [166].*

3.1.1 Superconducting state

The superconductivity of $PdTe_2$ was first observed by Guggenheim *et al.* in 1961 [169]. It wasn't until the identification of topological surface states by ARPES in 2015 [159] that it became extensively studied. The superconducting order parameter is fully-gapped [156], with an amplitude of $215 - 326$ μeV [160, 163, 164]. Comparing this values with the critical temperature, $\Delta_{BCS}/k_BT_c = 1.55 - 2.36$, close to the conventional BCS value of 1.76 [163]. DC magnetization and AC susceptibility measurements show the presence of the differential paramagnetic effect in applied magnetic fields $(1-N)H_c < H < H_c$, where $\mu_0 H_c = 13.6$ mT is the thermodynamic critical field [170] and N, the demagnetization factor of the single crystal used in the experiment. This provides strong evidence for the existence of the intermediate state (IS), which is a key property of a type-I superconductor [23]. The supercon-

ducting IS shall be defined as the coexistence of superconducting (S) and normal-state (N) regions [171]. Type-I superconductivity is in-line with the reported value of the Ginzburg-Landau parameter $\kappa = \lambda/\xi \approx 0.09 - 0.34$ [157, 170]. This value of κ is smaller than the theoretical boundary value $1/\sqrt{2}$, above which type-II behavior is expected. On the other hand, surface probes such as STM/STS [163, 164] and PCS [165] have given rise to an interpretation in terms of a mixed type-I and type-II superconductivity along with a spatial distribution of critical fields. This was attributed to an intrinsic electronic inhomogeneity at the surface already present in the normal phase. Furthermore, another STM/STS measurement [160] observed a vortex core reporting type-II superconductivity, however, an Abrikosov vortex lattice, hallmark of type-II superconductivity [23], is yet to be observed.

The electronic behavior of the superconductor under magnetic field (type-I or type-II superconductivity) is represented by ξ and λ. These characteristic lengths depend on the derivatives of $E(k)$, as $\xi \propto v_F = dE(k)/dk$ and $\lambda \propto \sqrt{n_s/m_s} = \sqrt{n_s}(d^2E/dk^2)^{1/2}$. Note that they depend on the **k**-vector, however at the macroscopic scale, they are usually averaged over the Fermi surface. Therefore, these lengths can be estimated from the band structure (see fig. 3.1(a)). This can result in different superconducting behaviors in the bulk and at the surface states [23]. In the case of $PdTe_2$, the bands that cross the Fermi surface are rather steep, resulting in large Fermi velocities, thus large ξ values. At the surface Dirac cone (SD), bands are less steep, thus lower ξ values. Furthermore, the density of occupied states peaks at SD, resulting in larger values of λ. We can qualitatively estimate type-I superconductivity (large Fermi velocities and low density of states) in the bulk and type-II superconductivity (smaller Fermi velocities and large density) because of the surface states.

More recently, transverse μSR measurements reveal the presence of normal regions (with H_c) in the bulk of the sample, which further supports the IS on the microscopic scale [172].

Furthermore, some measurements find superconducting signals above H_c [170, 173], the T-H phase diagram presents some similarities with those of so-called type-II/1 superconductors with $\kappa \approx 1/\sqrt{2}$ [170].

3.1.2 Theory

The superconducting nature of $PdTe_2$ has been unclear during recent years due to contradicting conclusions: type-I with IS [170, 172] and mixed type-I and type-II superconductivity [160, 163–165]. My work presented in ref. [174] show type-I superconductivity by imaging the magnetic pattern of intermediate state.

The main experimental situation which induces the IS is the application of a magnetic field, H, to a sample of non-zero demagnetizing factor, N, in the field range $(1-N)H_c < H < H_c$ [171]. This factor reflects the tendency of the demagnetizing field to reduce the total magnetization[1]. When the dimensions of the superconductor perpendicular to the applied magnetic field are small enough, the demagnetizing effects can be neglected, and the superconductor totally expels the magnetic field, which is the so-called Meissner effect [175]. When it cannot be neglected, the magnetic field penetrates the sample above $H = (1-N)H_c$, and at $H = H_c$ the sample becomes totally normal[2].

Other situations where the type-I superconductivity with IS is produced are: in a superconducting wire when the current exceeds the Silsbee current [175, 177] or in special configurations such as a superconductor enclosed inside another superconductor with higher T_c and H_c [171].

The IS results from the competition of volumetric magnetic energy and the N-S interface energy, which depends on the interface width, $\delta \approx \xi - \lambda$ [22, 178] (see fig. 3.2(a)). The structures tend to organize in a periodic manner, with a periodicity a and structure size, R, which both depend on the sample thickness, d, and the interface width as $\sim \sqrt{\delta d}$.

[1] The cases most often treated by theory and experiments are spheres with $N = \frac{1}{3}$, cylinders with traverse field with $N = \frac{1}{2}$ and thin plates in traverse field where the thinner the the more $N \to 1$.

[2] The penetration field is defined as the field above which the field enters the sample. For an ellipsoid, the penetration field is the same all over the sample, however, for other shapes, the penetration field depends on the measurement position (center of the sample is not the same that a corner). The definition of penetration field as $(1-N)H_c$ is usually taken true for the center of the sample, but a misalignment in the probe position could lead to important modification of the local demagnetizing factor, N[176].

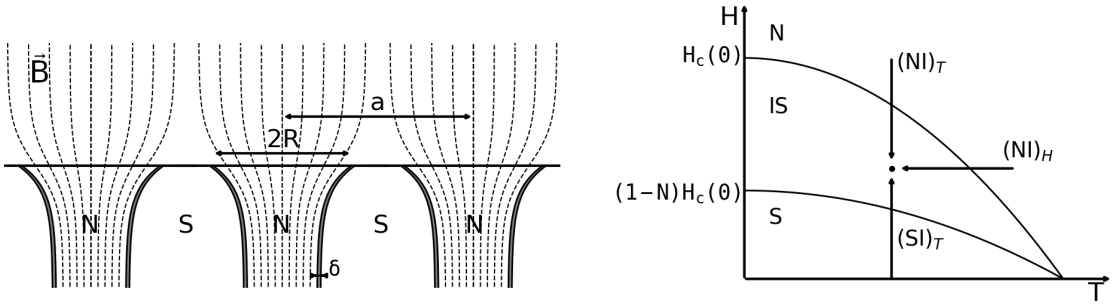

(a) (b)

Figure 3.2: *In (a), schema of the IS with the different regions (superconducting: S and normal: N), the magnetic field lines ($\vec{B}$), the size ($2R$) and periodicity (a) of the normal-state spots and the interface width (δ). In (b), representation of the T-H phase diagram with the different paths to reach an IS point: (i) increasing the field at constant temperature, (ii) cool down at constant field, and (iii) decreasing the field at constant temperature.*

In the case of superconductors with low κ, the IS pattern will be macroscopic, however, when $\kappa \to 1/\sqrt{2}$, δ decreases and the IS structures become smaller. Schematically, we could imagine a type-II vortex as the limit of a normal-state flux tube as κ goes beyond $1/\sqrt{2}$ [171]. For example, if we consider a sample in which κ is low and the thickness is thin enough, the equilibrium structures under traverse field are quantified vortices like those of type-II superconductivity [179]. Although for $\kappa \gg 1$ the IS cannot exist in equilibrium, Abrikosov suggested that for κ slightly greater than $1/\sqrt{2}$, the IS may also exist [26].

The IS regions in the bulk carry H_c, but as the regions approach the sample surface, the magnetic field spreads, thus, because of conservation of flux, the measured field is no longer H_c. Landau proposed that in order to avoid regions which don't carry H_c, the lamina would split in such a way that they always carry H_c (see fig. 3.3(a)). This is the so-called branching [178]. Lifschitz and Sharvin [180] reexamined the theory and concluded that multiple branching only occurs when the sample is extremely thick, whereas for ordinary experimental sample's dimensions the magnetic structures split once or twice, if they do. The critical thickness above which branching occurs was estimated to be $d_c \sim 800\delta$ at $H = 0.5H_c$ [181]. However, the unbranched laminar structure can lower its energy by

creating corrugations near the surface, so that the interface is increased [182, 183].

The magnetic field measured at the surface of the superconductor is lower than H_c [184], because of the field broadening and because some of the probes that may be only sensitive to the perpendicular component of the field (magneto-optical method [184], Hall probe microscopy [185] or the SSM [186]).

For low flux densities, normal flux tubes structures are more favorable than laminar structures, and for high flux densities, laminar or superconducting tubes structures are more favorable [178, 187].

As presented in fig. 3.2(b), a given point in the T-H phase diagram can be reached by various paths: (i) increasing the field at constant temperature (also known as Zero Field Cooling), (ii) cooling down at constant field (also known as Field Cooling), and (iii) decreasing the field at constant temperature. The pattern of equilibrium structures should not depend on the path taken, however, several authors observe complex maze-like structures with corrugated interfaces when the (T, H) point is reached by paths (ii) and (iii) [182, 184, 188, 189], and honeycomb structures when reached by path (i) [184, 185, 188, 189].

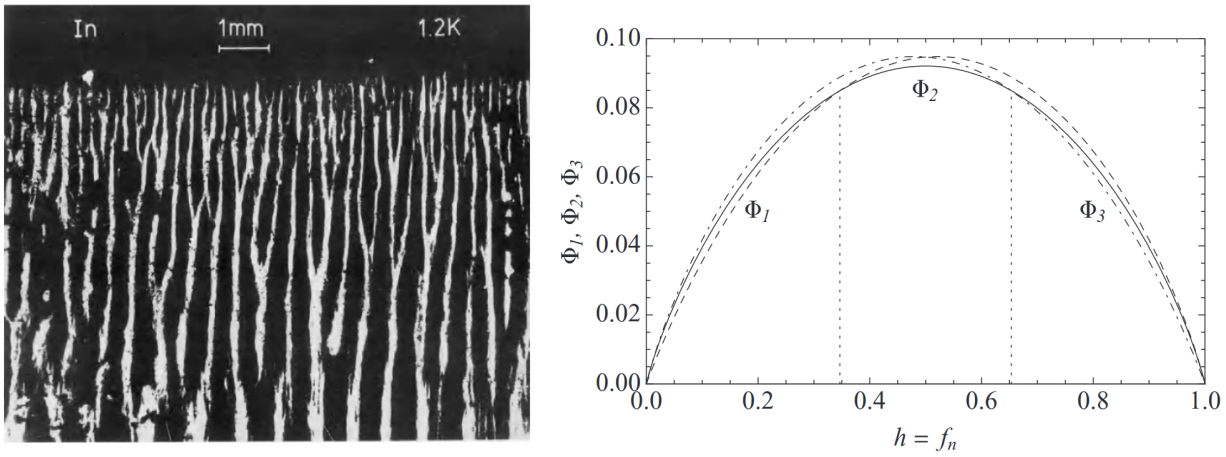

(a) (b)

Figure 3.3: *In (a), the branching of the intermediate state in an Indium sample, replicated with Cobalt powder: white is the normal-state laminae and the black is the superconducting regions [190]. In (b), the adimensional free energies of the different ground field distributions:* Φ_1 *for normal-state tubes,* Φ_2 *for laminae and* Φ_3 *for superconducting tubes [187].*

The IS was further studied by Goren and Tinkham [191], Fortini *et al.* [192] and more recently by Clem *et al.* [187].

Landau studied the continuity of the magnetic field deriving an equilibrium spreading distance proposing a laminar IS [22]. Goren and Tinkham considered a highly simplified model in which they compared the energy cost of normal-state spots and normal-state laminae. They took into account the volumetric and interface energies, obtaining the following equilibrium distances (see fig. 3.2(a)):

$$a^{spot}(h) = \sqrt{2\delta d/h(1-h)(1-\sqrt{h})} \tag{3.1}$$

$$a^{lam}(h) = \sqrt{\delta d/h^2(1-h)^2} \tag{3.2}$$

$$R(h) = \sqrt{h}a(h)/2 \tag{3.3}$$

where a is the periodicity, R is the half-size of the structure (radius of the spot or half-width of the lamina) and $h = H/H_c$. The ground state of the spot pattern has an energy slightly lower that the laminar model, which implies that either flux spots, laminae or both could exist in the IS.

Further investigation was carried out by Clem *et al.* [187]. They considered a bulk system with volumetric magnetic energy and normal-superconducting interface energy. The energetic balance showed that the ground-state energy of the system depends on the reduced applied field, h (see fig. 3.3(b)). Moreover, they performed the analysis on three different flux patterns: (i) normal-state flux tubes, (ii) laminae, and (iii) superconducting tubes, revealing that the ground-state changes from (i) at low fields, to (ii) a mid fields and to (iii) at high fields. For the (i) case, the radius of the spot and the lattice periodicity are given by:

$$R = h\sqrt{\delta d}/2\Phi_1 \tag{3.4}$$

$$a = \sqrt{2\pi/\sqrt{3}}\sqrt{\delta dh}/2\Phi_1 \tag{3.5}$$

for the case (ii) the half-width and the laminae periodicity are given by

$$R = h\sqrt{\delta d}/4\Phi_2 \tag{3.6}$$

$$a = 2R/h \tag{3.7}$$

and for the case (iii) the radius of the superconducting spot and the lattice parameter are

$$R = h\sqrt{\delta d}/2\Phi_3 \tag{3.8}$$

$$a = \sqrt{2\pi/\sqrt{3}}\sqrt{\delta d(1-h)}/2\Phi_3 \tag{3.9}$$

where Φ_i is the normalized free energy as defined for each case in ref. [187].

Summarizing, the IS patterns depend on the sample thickness and the path in the phase diagram. The theories presented above agree on the change of field distribution. These patterns can be understood from energy balance, where δ is the most significant parameter: the periodicity of the structures and the size depend on it.

3.2 Results

The single crystal of $PdTe_2$ used in this work was grown by Y. K. Huang by a modified Bridgman technique and characterized in reference [170]. The layered structure allows exfoliation before measurement. It was used for measurements of the London penetration depth, labeled s1 in ref. [157]. Among the four studied samples, this one had a $T_c = 1.66 \pm 0.02$ K and the zero temperature penetration depth $\lambda(0) = 377 - 470 \pm 10$ nm. The crystal used in the experiments is slab-shaped with length 0.88 mm, width 0.84 mm and thickness 0.097 mm, which gives a demagnetization factor of $N = 0.788$ for the center of the *ab* face [193]. All the measurements presented in this section were made above the *ab* face with the magnetic field applied along *c*-axis.

3.2.1 Confirming the phase diagram

In order to investigate the T-H phase diagram I measured the local magnetization, placing the SQUID at 350 nm above the sample and cooling the sample at zero field (ZFC) (see path (i) from fig. 3.2(b)). I recorded the SQUID response while increasing the applied

magnetic field, H, at rate of 50 μT/s for 13 different temperatures. In fig. 3.4(a), the critical current $I_c(H)$ is presented for three temperatures: $T = 1.7$ K (black line), 0.9 K (blue line) and 0.3 K (red line). At $T = 1.7$ K the sample is in the normal state and the response is the non-affected modulation (arcs) of the SQUID's critical current. Each period corresponds to one additional flux quantum entering the SQUID loop. At 0.9 K and 0.3 K the sample is in the superconducting state. The data starts off with a flat response, which corresponds to Meissner screening, up to the penetrating field $(1 - N)H_c$. Above this field the sample is in the IS and flux penetrates in a rather abrupt manner, as indicated by the fluctuating signal. Above H_c non-affected arcs are recorded, the sample is in the normal state. The field values $(1 - N)H_c$ and H_c measured in this way are indicated by arrows in fig. 3.4(a). In between these fields we denote a significant change in the SQUID response, from large to small fluctuations of I_c, at a *fusing* field, H_f. As we will show in the following, at this field tubular magnetic structures start fusing into laminar structures.

The values of these fields were collected and plotted in fig. 3.4(b). H_c follows the standard BCS behavior, $H_c(T) = H_c(0)[1 - (T/T_c)^2]$, with $\mu_0 H_c = 13.62$ mT and $T_c = 1.57$ K. The first value is in excellent agreement with the $H_c(T)$ behavior reported in ref. [170], however, the T_c is slightly lower than the one measured in ref. [157], probably due to the locality of the measurement. Correspondingly, I obtain $\mu_0(1 - N)H_c(0) = 3.83$ mT, which indicates a demagnetization factor of $N = 0.72$. This value is smaller than the calculated one, $N = 0.788$, which we attribute to an effective value $N_{eff} < N$, due to the locality of the probe. The effectiveness of this method for determining the phase diagram is the result of a very low resistance to flux penetration and weak flux pinning in $PdTe_2$ [174].

3.2.2 Zero Field Cooled

In order to investigate the equilibrium state, the best method is to study how the flux penetration develops in the IS after ZFC. The magnetic field distribution was measured at $T = 0.9$ K (blue dashed line in fig. 3.4(b)) for different fields (see fig. 3.5(a)-(d)). At

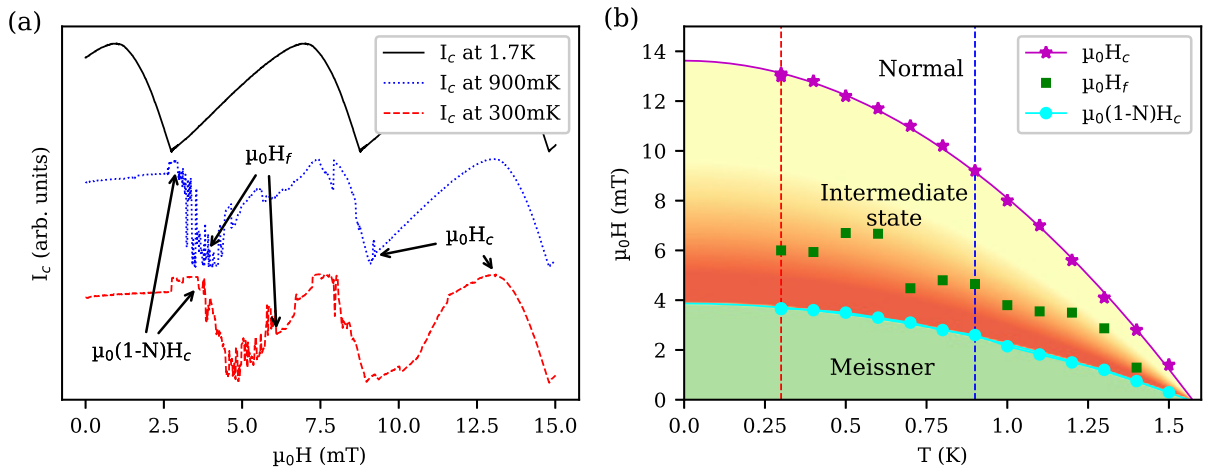

Figure 3.4: *(a) The SQUID response after ZFC at three temperatures. In the normal phase (black solid line) the SQUID response is smooth and periodic. In the superconducting phase we distinguish three different behaviors: (i) flat response, i.e. screening for $H < (1-N)H_c$, (ii) high-dispersion response, i.e. penetration of magnetic flux tubes for $(1-N)H_c < H < H_f$, and (iii) low-dispersion response, i.e. when flux tubes fuse into laminar structures $H_f < H < H_c$. The fields $(1-N)H_c$, H_f and H_c are indicated by arrows. In (b) the phase diagram is constructed from the gathered characteristic field values. The solid magenta line represents a BCS-like fit $H_c(T) = H_c(0)[1-(T/T_c)^2]$ with $\mu_0 H_c(0) = 13.62\ mT$ and $T_c = 1.57\ K$ and the solid cyan line is the equivalent fit with $\mu_0(1-N)H_c(0) = 3.83\ mT$ and $T_c = 1.58\ K$. The green squares indicate the field values when the flux changes become smoother above which laminar structures appear. The vertical dashed lines indicate the temperatures of the SQUID responses in (a). Grey lines represent the surface critical field measured by AC susceptibility, H_c^s, and the surface critical field found by resistivity measurements, H_c^R, referenced in [170]. The red diamond and the blue triangle are the T-H points of scans in fig. 3.10.*

the lowest applied field $\mu_0 H = 1$ mT the Meissner state is expected, which is confirmed in fig. 3.5(a). Some magnetic structures are observed, but since they do not evolve with the applied magnetic field (up to the penetrating field $(1-N)H_c$), they were likely created by the residual magnetic field upon cooling. The smallest structure is zoomed in the inset fig. 3.5(a) and the field profile along line A is plotted in the inset of fig. 3.5(e). We note that this structure is the least intense found.

When the magnetic flux penetrates the sample, magnetic structures fill the space as observed in the scans acquired at 3, 4.5 and 7.5 mT (see fig. 3.5(b)-(d)). At 3 mT (see

fig. 3.5(b)), the IS is established in a self-organized lattice of flux tubes. We notice two types of tubular structures: *mountains*, see the structures in fig. 3.5(a) and the profile in inset of fig. 3.5(e), and *volcanoes*, see fig. 3.5(b) and the profile in fig. 3.5(f). The strong dip on the center of the profile in fig. 3.5(f), which indicates the presence of a superconducting region as sketched in the inset, is a strong evidence of branching. The residual magnetic field above the dip on the center of the *volcano* is attributed to the overlapping stray fields of the surrounding normal region. The appearance of branching depends on the size and flux contained in the structure. Small ones like the one at $(x, y) = (15, 25)$ in fig. 3.5(b), do not present branching whereas the bigger ones do.

These closed structures should obey flux quantization [23], and the appearance of isolated single-Φ_0 structures, such as reported in refs. [160, 164], is possible. We measured the amount of flux contained in the weakest flux structure by two methods. One is fitting the flux profile of a hypothetical Abrikosov vortex to the measured flux profile. As penetration depth and height above the surface are interdependent parameters of the stray field originated from an Abrikosov vortex [194], the SQUID height was set to 350 nm and obtained a good agreement for an effective penetration depth of $\lambda_{eff} \approx 2.1$ μm and a total flux of $3\Phi_0$. The large λ_{eff} compared to the λ obtained by Salis *et al.* [157] indicates that field spreading effect is more important than in type-II superconductors, in which it's of the order of λ [139, 195]. The other method is model-free, based only on the definition of magnetic flux, which is the integration of magnetic field over an area. Fig. 3.5(e) shows the increase of collected flux with the increasing area of integration (square area of side L, centered at the flux spot zoomed in the fig. 3.5(a)). Before integration a linear plane fit was substracted to remove any field offset. This method tends to indicate $2.75\Phi_0$ for the amount of flux contained in the flux tube. As magnetic flux in a superconductor is quantized this indicates that the flux contained in the structure is $3\Phi_0$ and our procedure misses about 10% of the total flux.

The interface width is an important parameter in the energetic analysis of the system [22, 178, 187, 191, 192]. Following the model of Goren and Tinkham [191], it can be deduced

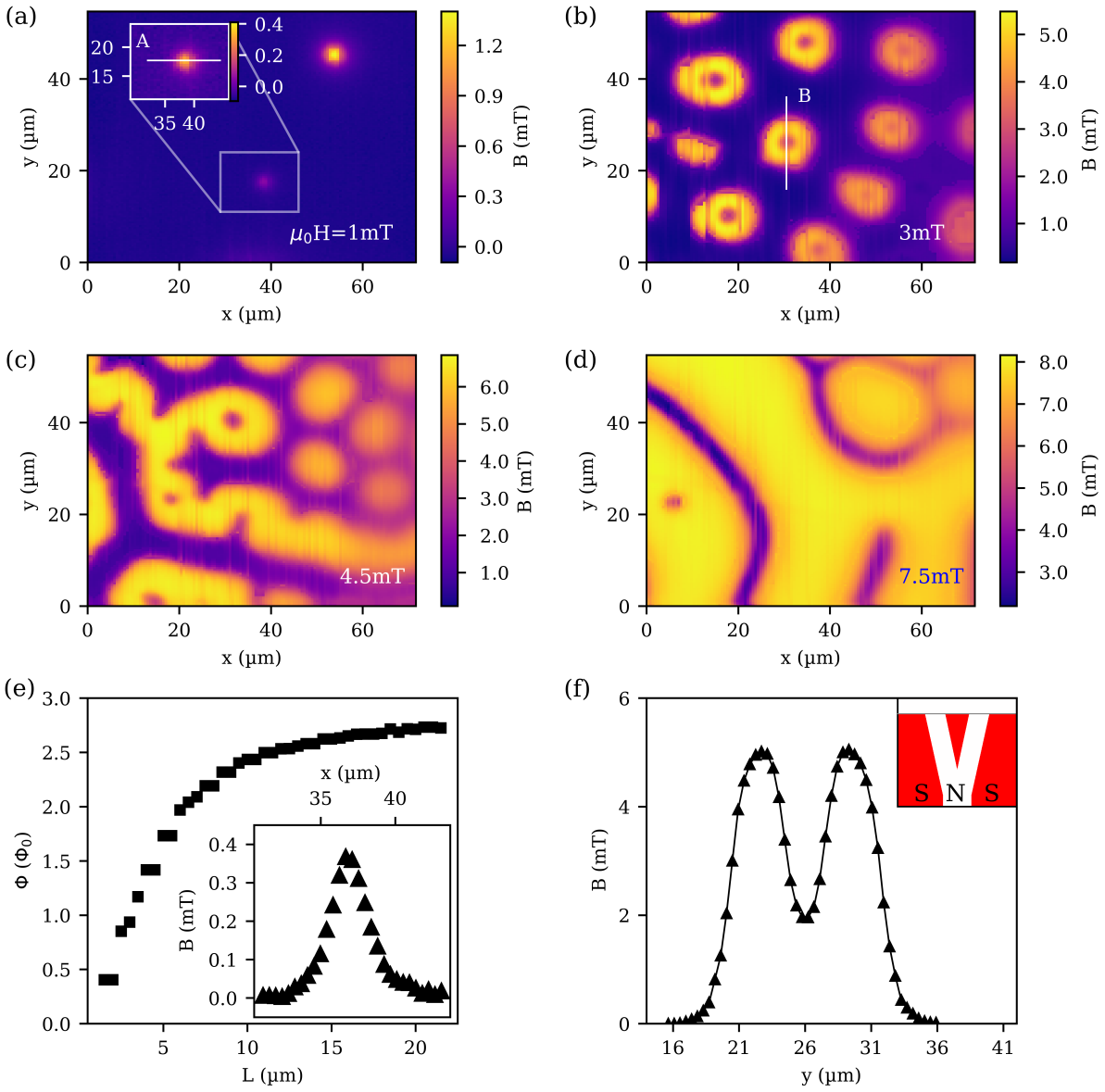

Figure 3.5: *Panels (a) to (d): ZFC magnetic images taken at* 900 *mK* ($\mu_0 H_c = 9.1$ *mT) and at an applied field of* 1 *mT (reduced field,* $h = H/H_c$*, of 0.11),* 3 *mT (0.33),* 4.5 *mT (0.5) and* 7.5 *mT (0.82), respectively (all images are from the same cool down). These images show the magnetic structures in the different regions of the phase diagram: dark blue regions are superconducting and orange ones are in normal state. The inset in (a) contains a zoom on the least intense observed flux tube. In panel (e) the inset shows the flux profile along the line A of the flux tube in the inset of panel (a), the main panel shows the increase in collected flux as the magnetic field is summed up over areas with increasing lateral length, L. In (f), the field profile along the line B in (b). The inset in (f) represents the schema of branching at the surface of the sample, neglecting N-S interface bending.*

either from the flux spot radius, R, or from the lattice parameter between adjacent flux spots, a, as presented in the sec. 3.1.2. Choosing fig. 3.5(b) to measure the lattice parameter and sizes of several spots ($2R \sim 13$ μm and $a \sim 20$ μm), the interface width resulting from the spot size is 0.24 μm and 0.19 μm based on the lattice parameter, for $h = 3/9.1$ and $d = 97$ μm. A second way to calculate δ is the model derived by Clem *et al.* [187]. The free energy of the flux tube pattern is $\Phi_1 = 0.079$ for this field. Based on the spot size diameter, the interface width attains the value of $\delta = 0.10$ μm. Alternatively, Clem *et al.* estimate δ from a normalized lattice parameter to be $\delta = 0.09$ μm. Since the model of Clem *et al.* does neither take into account the spreading of the flux tubes near the surface nor the branching of the flux tubes that we observe, the most reliable estimates of the interface width are the ones based on the lattice parameter, thus $\delta = 0.09$ μm according to the model of Clem *et al.* or 0.19 μm according to the model of Goren and Tinkham.

Above a certain threshold field, H_f, the tubular magnetic structures fuse into laminar domains, as for instance shown in the scan taken at 4.5 mT reported in fig. 3.5(c). The values $H_f(T)$ (green squares in fig. 3.4(b)) show a relatively high dispersion which is attributed to the coexistence and competing effects of tubular and laminar structures. Such coexistence of shapes has been reported before in the literature [196, 197]. Our results are consistent with the predictions of Clem *et al.* considering the small free energy difference between the flux arrangements [187].

The interface width was also derived from the laminar pattern like the one observed at 4.5 or 7.5 mT (fig. 3.5(c)-(d)) using the model of ref. [187]. The distance between two normal laminae is $a = 15$ μm and the width of the laminae is $2R = 8$ μm. The normalized free energy at the reduced field $h = 4.5/9.1$ is $\Phi_2 = 0.092$, which results in a value of $\delta = 0.09$ μm for the lattice parameter and $\delta = 0.09$ μm derived from the width of the normal laminae.

As the field increases, the normal laminae become wider and occasionally some superconducting tubular regions are observed, for instance at $(x, y) = (5, 22)$ in the fig. 3.5(d). The high field equilibrium state in our case is a mixture of tubular and laminar superconducting

structures at odds with exclusively tubular structures predicted for the high field phase in the Clem *et al.*'s model [187].

Measurements report only one single funnel-like branching per normal domain. Branching patterns similar to those in fig. 3.5(c) were reported [175, 198] in the case of elemental type-I superconductors. Branching is expected to occur only for a sample thickness larger

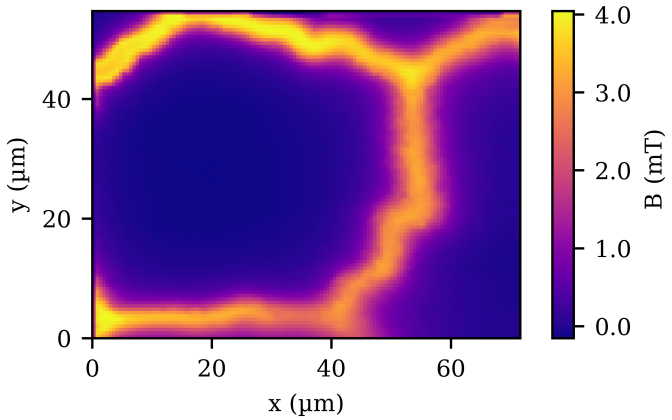

Figure 3.6: *Scanning SQUID image taken after cooling to* 300 *mK under* 1 *mT. Dark blue regions are superconducting and orange normal.*

than the critical thickness $d_c \approx 800\delta$ [175]. With our estimate of $\delta = 0.1 - 0.2$ μm, d_c falls in the range $80 - 160$ μm, the sample thickness being 97 μm one branch could be expected [180].

The partial duplication of the structure at $x = 15$ μm in fig. 3.5(b) and the vertical lines in fig. 3.5(b)-(d) denote movement of the structures while scanning, which we attribute to the coupling between the SQUID's magnetic field and the structure itself. This movement can only be observed in case of weak flux pinning.

3.2.3 Field Cooled

Above I presented flux structures in the IS after ZFC. Alternatively, one can reach the IS by field cooling (FC) from the normal phase (see path (ii) from fig. 3.2(b)). In general, the flux trapped in the sample results in laminar structures [175]. At low fields (such as

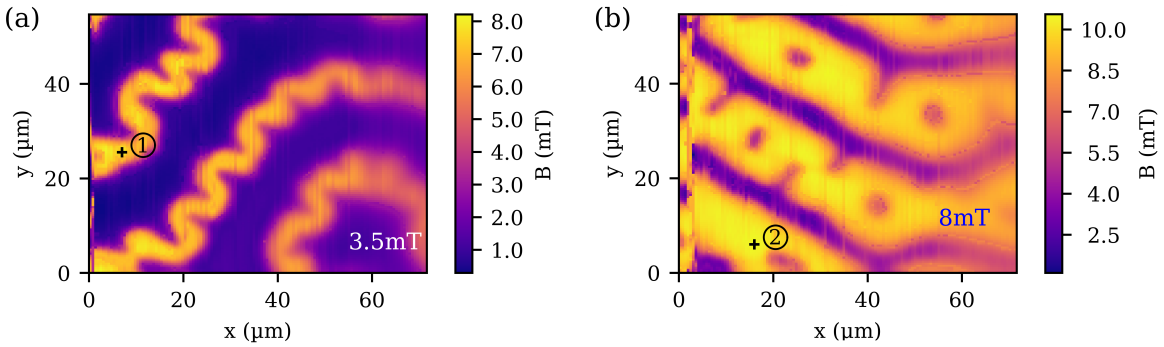

Figure 3.7: *Magnetic images taken after field cooling under* 3.5 *mT (reduced field,* $h = H/H_c$*, of 0.34) and under* 8 *mT (0.61) in (b), at a temperature of* 300 *mK,* ($\mu_0 H_c$*=13.1 mT). Points 1 and 2 indicate the maximal measured fields of each scan used to plot fig. 3.8. Dark blue regions are superconducting and orange normal.*

the residual field when ZFC) tubular structures are also found in addition of laminae (see scan at 0.3 mK and 1 mT in fig. 3.6). The honeycomb pattern appears when the field is low enough to let the IS structures organize themselves, their junctions tend to form 120°. This indicates that the repulsion of the normal-state laminae is stronger than the pinning. In fig. 3.7(a) (scan at 0.3 K in 3.5 mT), corrugated normal-state laminae are present. As the field is increased, the laminae get wider and with more corrugation, eventually tubular superconducting structures are enclosed in the lamina, as observed in the 8 mT scan of fig. 3.7(b). At higher fields, normal-state laminae get wider until the whole sample becomes normal.

3.2.4 Field at the surface

According to the theory of the formation of the IS of a type-I superconductor the magnetic field in the normal domains should always be equal to $\mu_0 H_c$ in the bulk [23], but at the surface, it is lower than $\mu_0 H_c$ as measured by two authors [198, 199]. In the case of $PdTe_2$, μSR measurements [172] verified the magnetic field in the bulk, however, we reported the first measurements of the magnetic field at the surface. A field lower than H_c is attributed to the spreading of the flux tubes at the surface. As many other magnetic techniques such as Hall probes [185, 200] or magneto-optical method [184], the SQUID sensibility depends

on the direction of the magnetic field. In our case we are sensitive only to the field perpendicular to the SQUID loop. As mentioned in sec. 2.1, our SQUID makes an angle of 3° with the sample surface, thus we consider that we are only sensitive to the normal component of the magnetic field emanating from the sample.

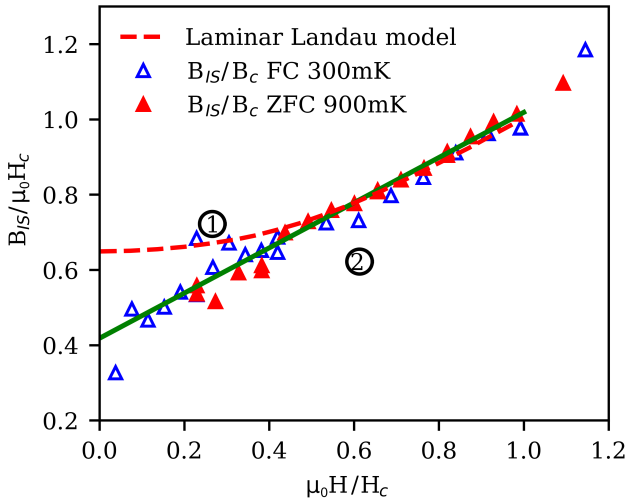

Figure 3.8: *The maximum of the magnetic field above the normal regions in the IS divided by the critical field, $B_{IS}/\mu_0 H_c$ (triangles) as a function of the applied field divided by the critical field, H/H_c, for in red, ZFC (900 mK) and, in blue, FC (300 mK) measurements. The green line represents a linear guide to the eye. The red dashed line traces the reduction of the maximal field at the surface in case of the Landau laminar model as reported by Fortini et al. [192]. Points 1 and 2 are references to the corresponding points in the images of fig. 3.7.*

From multiple images, like those ones obtained after ZFC at 900 mK (see fig. 3.5) and others obtained after FC at 0.3 K (see fig. 3.7), I measured the magnetic field of the sample at the center of many IS structures, B_{IS}. These measurements (tubes and laminae) were normalized by the critical field, $\mu_0 H_c(T)$, and then traced in fig. 3.8 as a function of the reduced applied field, H/H_c. We observe that $B_{IS}/\mu_0 H_c$ increases linearly as function of the applied field. For reduced fields $H/H_c > 0.5$, the measured values align with the Landau's prediction for the laminar model as expressed by Fortini *et al.* [192]. At lower fields, tubular structures are present in the case of ZFC and laminae in the case of FC, but in both cases

the field B_{IS} follows the same linear behavior, which could be attributed to field spreading for both geometries.

The measurements of the magnetic field at the sample surface allow to estimate the degree of spreading based on conservation of flux. $\Phi_{spot} = \mu_0 H_c S_{bulk} \approx \mu_0 H_{surf} S_{surf}$, where S_{bulk} and S_{surf} are the cross sections of the magnetic structure in the bulk and at the surface respectively. This implies the ratio H_{surf}/H_c behaves as S_{bulk}/S_{surf}. Considering $B_{IS} = B_{surf}$ as a first approximation and $B_{IS}/\mu_0 H_c \approx 0.4$ at the onset of the IS (see fig. 3.8), we could estimate that the ratio S_{bulk}/S_{surf} is linear with the applied field. Thus, the S_{surf} at 0 mT would be 2.5 times the S_{bulk}, whereas at H_c, $S_{surf} = S_{bulk}$.

The question of how far this spreading effect carries over into the bulk of the superconductor was calculated [192] in the framework of the Landau laminar model. The filling fractions for the fig. 3.7 are 38% and 66% respectively, the characteristic depths of spreading are predicted to be about 0.25 and 0.4 times a. The typical spacing of the order of $a = 20$ μm (see fig. 3.7(a)) would indicate the spreading of the interface at a depth of 5 μm and 8 μm respectively. This reduction could be observable by bulk probes in very thin samples.

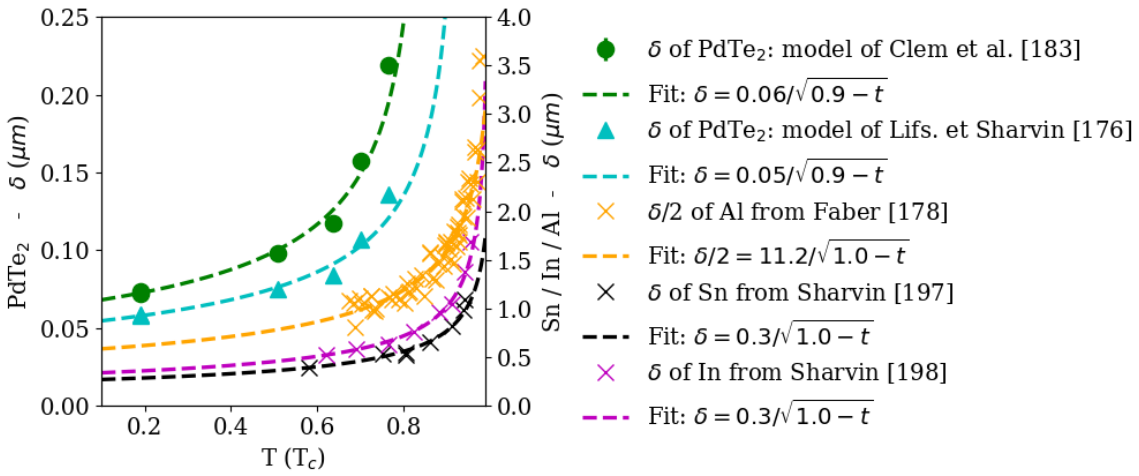

Figure 3.9: *Interface width, $\delta(T)$, obtained with the model of Clem et al. [187] in green and the model of Lifschitz and Sharvin [180] in cyan. The data of Al from Faber [182] and Sn/In from Sharvin [201, 202] are also represented for comparison. The lines in the corresponding colors are the corresponding fits with $\delta = C/\sqrt{1-t}$.*

3.2.5 Interface width

Further analysis of the interface energy can be carried out from the temperature dependence of δ. Sn and In samples were measured by other authors and a $\delta \propto 1/\sqrt{1-t}$ behavior was found [201, 202], which is in agreement with the $\xi(T)$ BCS behavior [175]. Faber proposed a dependance of $\delta \propto 1/\sqrt{1-t^4}$ based on Landau theory and the corrugations of the IS regions, however, he found $\delta \propto 1/\sqrt{1-t^{3/2}}$ for Al samples [182]. In fig. 3.9, the $\delta(T)$ of $PdTe_2$ obtained with the model of Clem *et al.* [187] and with the model of Lifschitz et Sharvin [180] was plotted along with the data of Al, Sn and In [182, 201, 202]. For each set, $\delta \propto 1/\sqrt{1-t}$ behavior agrees with the data of the four materials. The data of Faber were taken in the temperature range of $t > 0.6$. Below $t = 0.975$, both dependances describe well the data, above this value data points are scarce.

In the case of $PdTe_2$, there are not many points, but values obtained with both models seem to follow the behavior $\delta \propto 1/\sqrt{1-t}$, however, more data should be gathered to claim such behavior.

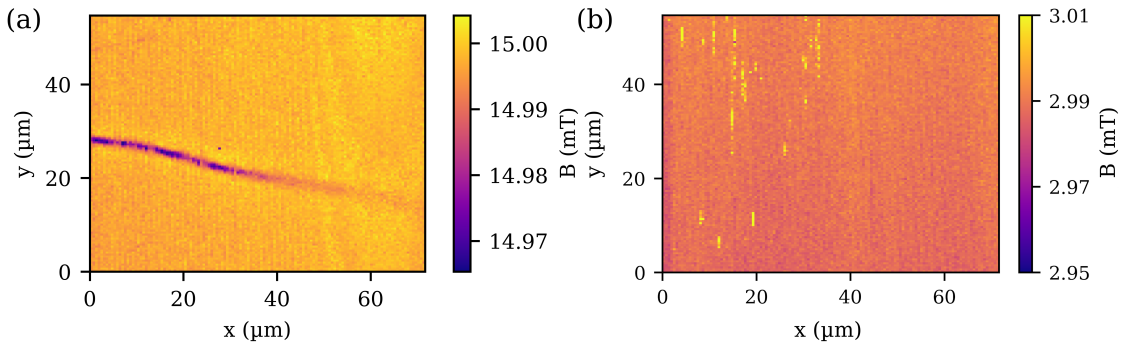

Figure 3.10: *Scans of the same spot of the sample at 300 mK and 15 mT and at 1.5 K and 3 mT. Both T-H points correspond to bulk normal phase, but the signal is different. These two points are represented in the phase diagram of fig. 3.4(b) as a red diamond and a blue triangle respectively.*

3.2.6 Signal above H_c

Leng *et al.* found traces of superconductivity above H_c with another T_c [170]. Their figure

of phase diagram presents the bulk $H_c(T)$ curve, the surface critical field, $H_c^s(T)$ measured by susceptibility and also the surface critical field measured by transport measurement, $H_c^R(T)$. The surface superconductivity only appears when the field is applied perpendicular to a small dimension of the sample, which would be in the plane *ab* for our sample. The fig. 3.10 presents two scans that lay out of the bulk superconducting phase: at 0.3 mK and $H = 15$ mT and at 1.5 K and 3 mT, represented in fig. 3.4(b) as a red diamond and blue triangle respectively. A weak magnetic signal was measured above bulk $H_c(T)$ for low temperatures but not at high temperatures, which is consistent with the results of ref. [170].

Pinning effects are usually caused by structural defects and impurities among other causes. The presented results support small/no pinning effects for bulk superconductivity, nevertheless, the structure from fig 3.10(a) always sits on the same spot. Although surface superconductivity as we know it should not happen in our experiment (and if it appeared, it would have the same T_c), the magnetic signal evidences some screening, which is not present at higher temperatures.

Recently, a possible explanation based on the stoichiometry was proposed [203], superconductivity could survive in a small fraction (10%) of the crystal where the stoichiometry is slightly different ($PdTe_{2+x}$) [169]. However, these compounds have generally a higher T_c than $PdTe_2$ [169, 204, 205]. Energy Dispersive X-Ray Analysis should be carried out to verify this hypothesis.

3.3 Conclusion and outlook

One of the major results from the present SSM measurements is the direct observation of the IS on the local scale in a binary compound. The evolution of the different patterns depending on the phase diagram path was studied in detail in the field range $(1 - N)H_c < H < H_c$, revealing the succession of tubular to laminar structures as the applied field is increased after ZFC. The smallest structure measured was found to hold 3 Φ_0, confirming the quantification of flux and therefore, not excluding single-Φ_0 structures

(typical superconducting vortex), which were reported by some authors [163–165]. In the FC case, laminae were revealed, at low field they tend to form angles of 120°, creating a honeycomb pattern. As the field is increased some corrugation appears in order to minimize the energy. At higher field, the corrugations tend to enclose superconducting tubular structures.

The spreading of magnetic field as the structure approaches the surface of the sample is well known in the IS literature but the experimental observations are rare. In $PdTe_2$, the reduced magnetic field of IS regions (tubular or laminae) is proportional to the reduced applied field for any temperature. At high field it corresponds to the expected behavior for a laminar pattern, as the ZFC measurements revealed. For any field and any temperature, this curve represents the spreading given by the ratio S_{bulk}/S_{surf}. The spreading length of the IS superconductors is larger than the penetration length in type-II superconductors, therefore, the magnetic profile of an usual vortex is not valid for IS, thus, cannot be used to quantify the flux.

Further focus lay on the interface width. This parameter rules the energy balance of the magnetic flux distribution in the compound, dicting the lowest energy pattern. Thanks to the models of Lifschitz and Sharvin [180], Goren and Tinkham [191] and Clem *et al.* [187], this parameter was univocally estimated to be 0.1-0.2 μm. The evolution in temperature seems to follow the behavior of $\delta(\mathrm{T}) = C_\delta/\sqrt{1-t}$ such as other materials, however, further measurements in $PdTe_2$ are needed to verify this behavior. The branching of magnetic structures may happen above a critical thickness, which is proportional to the interface width. The observation of single-funnel branching for tubular and laminar structures are in agreement with the sample thickness and the critical thickness estimated from the interface width.

The effectiveness of the method used for determining the phase diagram, the partial duplication of some structures due to their movement while scanning and the arbitrarity of the low FC structures orientation can only be observed in the case of weak pinning.

Furthermore, an unexpected signal was found pinned above bulk H_c for low temperatures which wasn't found at high temperatures.

Chapter 4

Chiral superconducitivity in UPt_3

UPt_3 has a crystalline structure of the $MgCd_3$ type, shown in figure 4.1 [65]. The uranium atoms form a closed-packed hexagonal structure with the platinum atoms between uranium ones on the planar bonds (see figure 4.1.(a)). The compound belongs to the space group $P6_3/mmc$ [1] and the point group D_{6h} [2]. The lattice parameters are a=b=5.764 Å and c=4.899 Å, the distance between uranium's atoms is 4.132 Å and between Pt and U atoms 2.882 Å. The density is 19.4 gcm^{-3} and the molar volume of 42.43 cm^3/mol U.

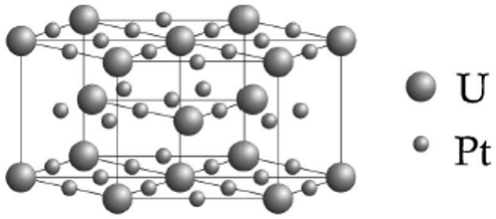

Figure 4.1: *Crystal structure of UPt_3 [65].*

The single crystal of UPt_3 used in the experiments was grown by D. Aoki using the Czochralski method, then it was annealed at 900°C. Finally, our sample was spark cut from the ingot, the scanning face was polished and reannealed again at 900°C for 15 days.

[1] $P6_3/mmc$ is a space group. P refers to primitive lattice. 6 for six-fold symmetry. 3 refers to the translation vector. /m refers to a mirror perpendicular to the six-fold axis The other m refers to a mirror which contains the six-fold axis. c refers to a glide translation along half the c-axis lattice vector.

[2] D_6 means a six-fold rotation axis plus 6 two-fold axis perpendicular to the six-fold axis. The h stands for a mirror plane with normal on the six-fold axis, and also six mirror planes, each containing the six-fold axis and one of the two-fold axes.

The polished face corresponds to the c face. The dimensions of the sample used in the experiments are 1.5x1x0.65 mm^3.

For the following work, the magnetic field is always applied along the c axis and the scans are carried out above the ab face. Given the dimensions of the sample and the scanned surface, the sample has a demagnetization factor of $N = 0.48$ [193].

As mentioned in sec. 2.6, the Earth's magnetic field is subtracted from the applied field when the sample is cooled at zero field, thus we observe the Meissner effect. This offset is calculated when the calibration is made, however, the background field varies slightly with time, resulting in a small error (<5 μT) in the zero field of each measurement. Because of this, we always have some magnetic structures present.

Our sample has a residual resistance ratio of 583. The superconducting transition measured by specific heat measurement on a ^{3}He PPMS system from Quantum Design happens at 514 mK with 25 mK of width (see fig. 4.2). The transition A-B phase occurs at 460 mK with also $\sim$ 25 mK of transition width. In order to calculate the local susceptibility, the magnetization was measured in response to alternating applied field. The difference of readout may be considered as an approximation of the measurement of the module of χ. This process was carried out for several temperatures, revealing the superconducting transition at 520 mK. In addition, a susceptibility peak appeared at the transition, indicating dissipative processes (related to Im(χ)) at the onset of superconductivity [206]. These authors also detected another peak at the A-B phase transition, 300 times smaller than the one at the superconducting transition.

4.1 Chiral domains: theoretical predictions

In a superconductor with complex order parameter, there are at least two ground states, each of the them with different chirality. If they coexist, they will form chiral domains separated by domain walls (DWs). Following the theoretical works on the chiral phase of ^{3}He [207], several authors have studied the effect of chiral domains in superconductors and

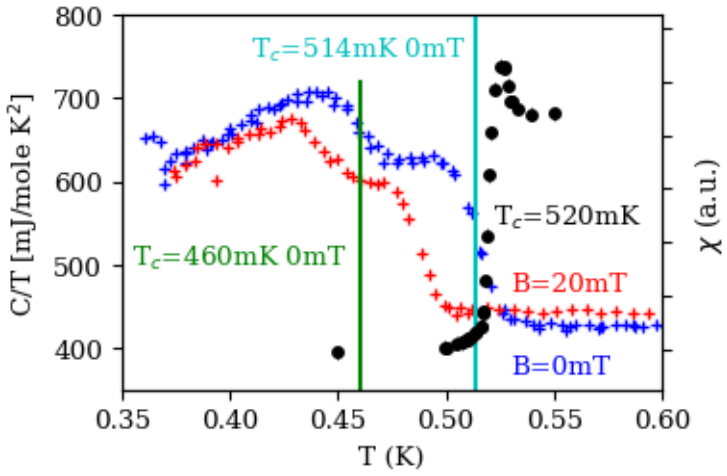

Figure 4.2: *Red and blue lines are specific heat measurements of the sample of UPt_3 used in the SSM measurements for two different fields. The critical temperatures at zero fieldare taken at the middle of the transition, they are marked in green and cyan. This was measured by K. Hasselbach in a ^3He PPMS system from Quantum Design. The black curve is the local susceptibility of the crystal as a function of the temperature. This last measurement was measured with the scanning SQUID, alternating measurements at fields of $\pm 50\ \mu T$.*

the interactions happening at DWs (see fig. 4.3(a)) [35, 69, 208–211].

Due to the complex nature of the chiral order parameter, the phase of a domain winds within the domain, thus, a chiral domain breaks time-reversal symmetry (TRS). At the DW, the two chiral domains interact and, due to the winding, the relative of phase between domains can vary along the DW. This was studied by Etter *et al.* in the case of a chiral p-wave in a tetragonal system such as Sr_2RuO_4, deducing that the relative phase was π-periodic with minima at 0 and π [131] as presented in (see fig. 4.3(b)-(e)). The spatial variation of the relative phase may produce a spontaneous superconducting current, often called chiral current, and/or unusual magnetic field distributions [69, 208, 209, 213]. The effect on the magnetic field distribution is predicted to be quite complex. Among the various magnetic signatures, I would like to mention a few: (a) the magnetic field peak arises spontaneously in the DW when approaching the sample side surface (see fig. 4.4) [208], (b) in the vicinity of the DW, one domain presents a concentration of magnetic flux, whereas the other domain

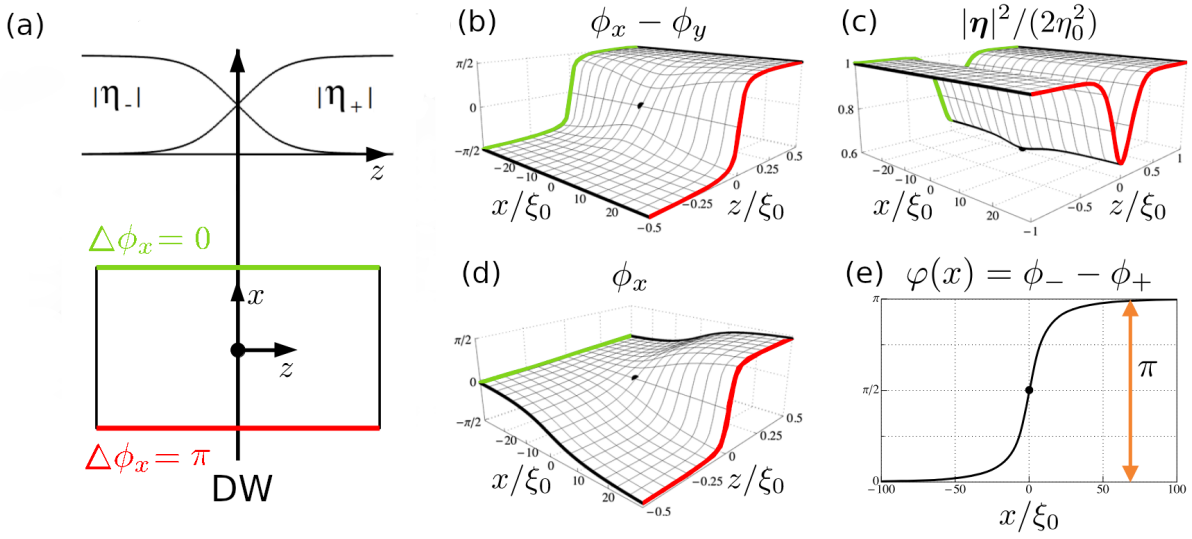

Figure 4.3: *In panel (a), a schema of the two domains joining at $z = 0$. The wavefunction of each domain tunnels into the other one. The order parameters are: $\eta = (|\eta_+|, |\eta_-|e^{i\varphi}) = (|\eta_x|e^{i\phi_x} + i|\eta_y|e^{i\phi_y}, |\eta_x|e^{i\phi_x} - i|\eta_y|e^{i\phi_y})$. The stable ϕ_x shift across the transition is either 0 (green line) or π (red line). In the panel (b), the phase difference between η_x and η_y, which denotes the domain wall. In (c), the modulus of the order parameter, presenting a depression at the DW. In panel (d), the phase shift between stable values: 0 and π. In panel (e), the relative phase between domains wavefunctions. Figures (b)-(e) were modified from ref. [131].*

presents a lack of it(see fig. 4.4) [208], (c) if chiral domains coexist, one will be favored by the applied field (see fig. 4.5) [35, 212], (d) vortices may decay into structures with fractional flux, that would be pinned at the DW. In particular, Etter *et al.* showed that half-Φ_0 structures are favorable in their system and would sit at the DW between relative phases of 0 and π. However, in the case of UPt_3, an analogous analysis shows 2π-periodicity, thus, single-Φ_0 structures.

So far structures containing fractional quantum of flux ($\Phi_0/2$) were only observed at the junction of three $YBa_2Cu_3O_{7-\delta}$ crystals specifically orientated for the symmetry of the order parameter (*d*-wave) [214, 215]. In order to explain this experiment, Volovik proposed a disclination: the orientation of the crystal lattice continuously changes by π around the structure [210]. Furthermore, he predicted half- and fourth-Φ_0 structures in the tetragonal

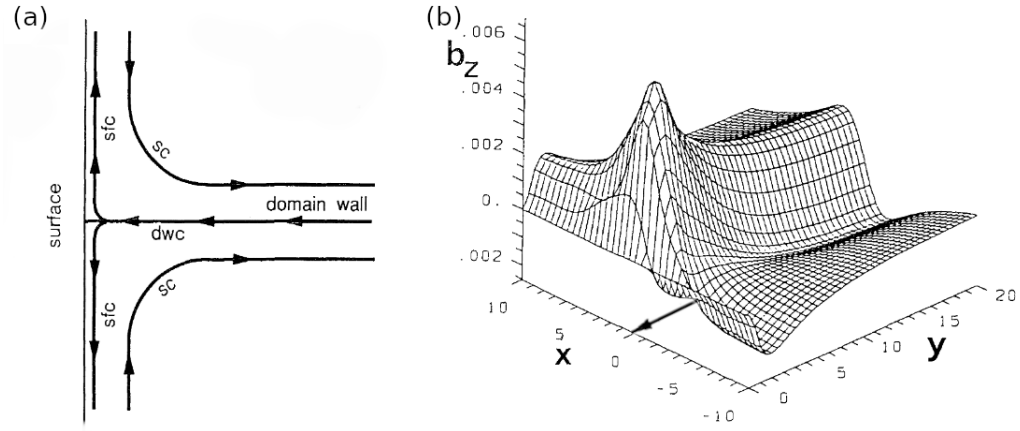

Figure 4.4: *In panel (a) picture of the currents around the DW when it arrives to the sample surface: dwc means domain-wall current; sfc, surface current; sc, screening current. In panel (b), the field distribution at the surface of the sample above a DW (x=0). The chiral current or domain wall current is indicated with an arrow. Figure modified from ref. [208].*

system for *d*- and chiral *p*-wave respectively, which is in contradiction with the results of Etter *et al.* [131].

At the DW, single-Φ_0 vortices may decay into fractional structures. Therefore, they would be strongly pinned and may form a line on the DW, repelling single-Φ_0 vortices. In this way it acts as an effective barrier for vortex dynamics [208].

The community agrees that domains of chiral superconductors break TRS and that fractional structures should exist in the frontier between chiral domains. This is only possible thanks to the interaction of both domains. However, the fractional amount of flux contained by the structure in a given system is still unclear.

4.2 Measurement of H_{c1}

In order to investigate the T-H phase diagram the local magnetization was measured while ramping the applied magnetic field. The SQUID sat 350 nm above the sample, the crystal was cooled through T_c in zero field and then, a magnetic field ($H \parallel c$) was ramped at rate of 50 μT/s to measure the local magnetization (see detailed translation method in appendix B). The first curve after ZFC (virgin magnetization curve) was measured at 16

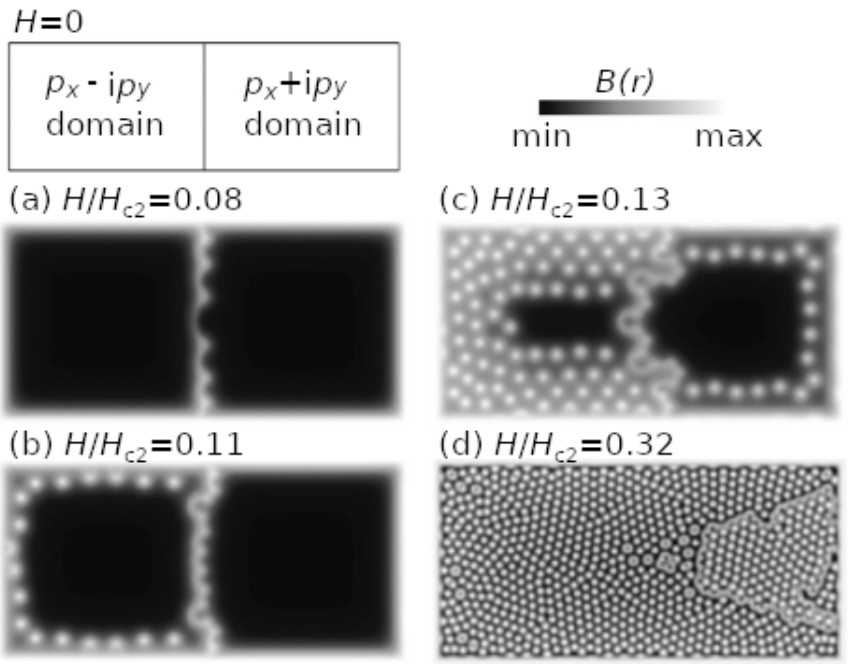

Figure 4.5: *Evolution of flux distribution with the applied field for two domains of different chirality. Figure modified from ref. [212].*

different temperatures in order to calculate $H_{c1}(T)$. The penetration field, H_p, is defined as the field at which the susceptibility (slope) of the virgin magnetization curve moves away from -1, i.e. $B = 0 \rightarrow B \neq 0$. This is presented in fig. 4.6(a) for $T = 350$ mK, where the magnetization curve and susceptibility (inset) are plotted as a function of the applied magnetic field. In the same figure, the corresponding H_p is marked with a red star. If we don't consider the demagnetizing effects, $H_p = H_{c1}$, however, in our experiments the sample has a non negligible demagnetizing factor, therefore the penetrating field is given by $H_p = (1 - N)H_{c1}$. With the calculated demagnetizing factor $N = 0.48$, the lower critical field is about the double of the measured penetrating field.

Previously, magnetization measurements were carried out on polycrystals by Jaccard *et al.* [216], and Palstra *et al.* [217] and on a single crystal ($H \perp c$) by Amann *et al.* [206]. Their hysteresis curves are slightly different from ours: smaller maximal magnetization values and smooth flux penetration (a kink around -6 mT is present in our curve of fig. 4.6(a)). Qualitatively the virgin curves are in good agreement, although quantitatively H_{c1} does not

agree with them. This difference likely comes from the locality of our probe. However, complete hysteresis cycles should be measured at different temperatures and at different domains to confirm the reproducibility.

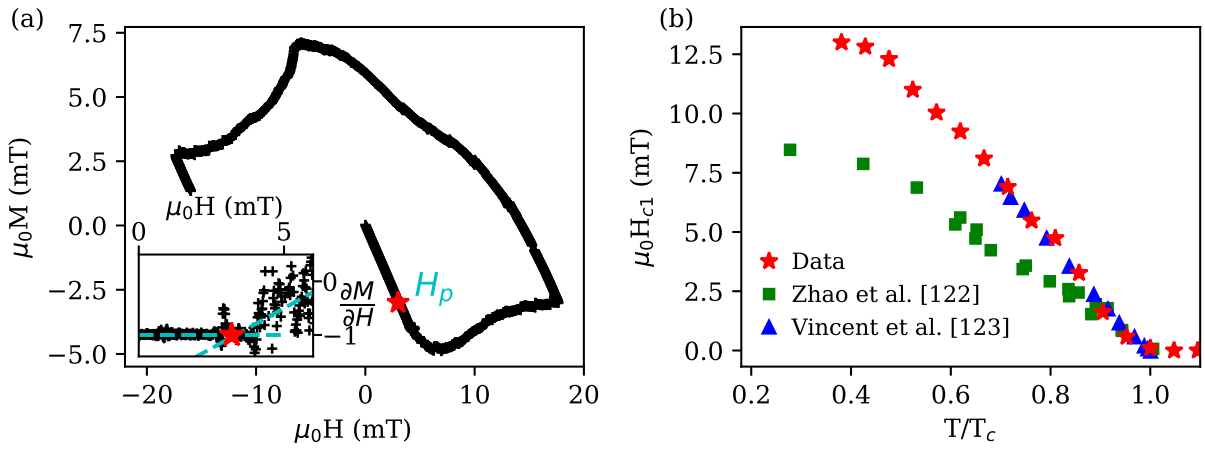

Figure 4.6: *In panel (a), the local magnetization after ZFC and ramping up the field to 17.5 mT, then down to -17.5 mT and back up to 0 mT at a rate of 50 μT/s at 350 mK. $\mu_0 H_p$ is the penetration field, at which the slope of $M(H)$ curve after ZFC shifts from -1. This is presented in the inset with the cyan dashed guidelines and $\mu_0 H_p$ in the red star. After calculation H_{c1} taking into account the demagnetizing factor ($N = 0.48$), the lower critical field curve is plotted in panel (b) as a function of the reduced temperature, along with the results of Zhao et al. [122] and Vincent et al. [123].*

The measured values of $\mu_0 H_{c1}$ are plotted as a function of the normalized temperature in fig. 4.6(b), along the data of Zhao *et al.* [122] and Vincent *et al.* [123]. Our data are in good agreement with the results of the latter. In addition, both groups reported a kink at a certain temperature below T_c (between 50 mK [123] and 150 mK [122]), which should be related to the A-B phase transition due to a change in the condensation energy. However, our data are not dense enough to detect it.

4.3 A vortex: quantification and penetration depth

Quantification of flux

In a typical type-II superconductor, the magnetic field induces vortices with one Φ_0. I

studied the temperature dependence of an isolated vortex (see fig. 4.7(a)). At the lowest temperature (300 mK), the amplitude is the greatest and the spreading of the structure is the smallest, therefore, the flux contained in the structure could be quantified by integration of the magnetic field for different circular Region of Interest (ROI) centered at the structure. The evolution of the flux as function of the size of the ROI is presented in fig. 4.7(b). As the ROI size increases, the magnetic flux tends to approach asymptotically one Φ_0, however, it does not saturate at this value as the vortex flux extends beyond the range of the image.

Penetration depth

The temperature dependence of the penetration depth can be described by $\lambda(t) = \lambda(0)/\sqrt{1-F(t)}$ [218], where $t = T/T_c$ is the normalized temperature, $F(t)$ is a temperature dependent integral which contains information about gap structure and density of states, and $\lambda(0)$ is the extrapolation of the penetration depth at $t = 0$. In an isotropic BCS case $F(t) = t^4$ [23, 219, 220], but the presence of zeros in the superconducting gap can result in behaviors described by other powers $F(t) = t^n$. This dependence is usually measured at low temperatures ($t \ll 1$), where this behavior is approximately described by $\lambda(t) \approx \lambda(0)(1+F(t)/2)$. Some reported low-temperature measurements are collected in tab. 4.1 and show linear [218, 221, 222], squared [218, 222–225] or close-to-4th/4th order dependence [222, 226, 227]. The linear behavior was likely caused by the gap symmetry in the ab plane while the squared behavior has unclear origin. The close-to-4th and 4th order dependence was addressed to the effect of the frequency of the Tunnel Diode Oscillator technique (TDO) [222, 227].

For each temperature, a monopole distribution with near-field correction (see appendix C) was fitted with the penetration depth as the only free parameter (the flux inside being confirmed by flux integration). For instance, the fit of the profile at 300 mK is presented in the inset of fig. 4.7(b). In our case I measured the magnetic field profiles for temperatures $t > 0.6$ ($T > 300$ mK), which are presented in fig. 4.7(c). The data is well described by the complete expression with an exponent $n = 4.05$, $T_c = 517$ mK and $\lambda(0) = 2.2$ μm (see

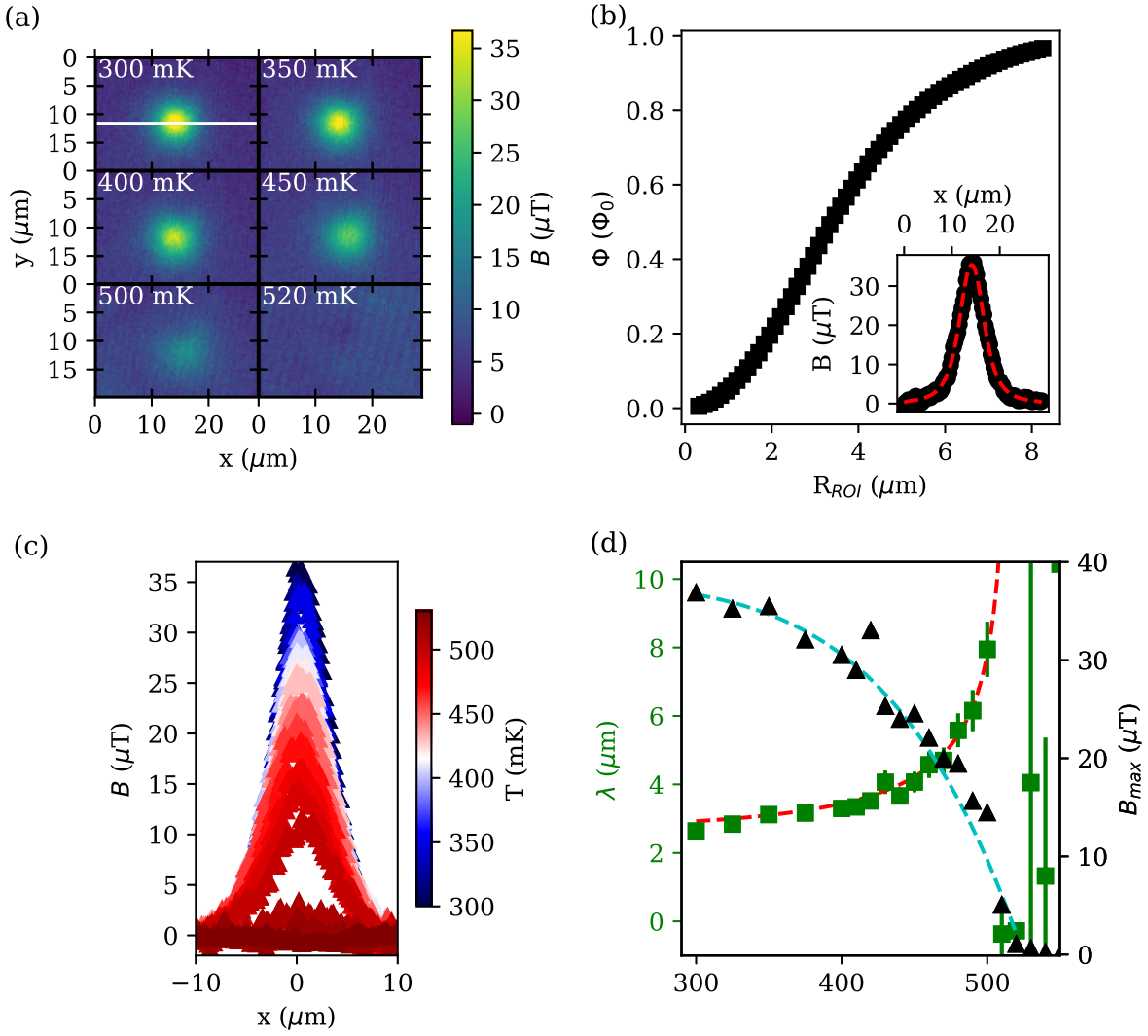

Figure 4.7: *In panel (a), scans at different temperatures after the same ZFC procedure are presented in a common color range with a scanning height of 350 nm. In panel (b), the flux integration of the structure at 300 mK is presented as a function of the radius of the ROI centered in the structure, R_{ROI}. The inset represents the fitting of the 300 mK profile. In (c), the profiles across the maxima for different temperatures. In (d), the penetration depth, $\lambda(T)$, obtained by fitting the profiles of (c) with the monopole distribution with a near-field correction [195]: $b_z(r,T) = \Phi_0/2\pi(z+1.27\lambda(T))/(r^2+(z+1.27\lambda(T))^2)^{1.5}$ (see appendix C). The red line is the fit of $\lambda(T) = \lambda(0)/\sqrt{1-(T/T_c)^n}$, with parameters $n = 4.05$, $T_c = 517$ mK and $\lambda(0) = 2.2$ μm. In the right axis, the maximal field of the vortex is plotted as a function of the temperature. A phenomenological fit ($B_{max} = B_{max}(0)(1-t^n)$) is presented in cyan with parameters $n = 5.97$, $T_c = 525$ mK and $B_{max}(0) = 38$ μT.*

$\lambda(0)$ (μm)	n	Technique	Ref.
2.3	1<2	Ultrasounds	[218]
2	1	Mutual inductance	[222]
2	2.5-3.7	Tunnel Diode Oscillator	[222]
0.62	2	SQUID-magnetization	[223]
1.9	2	DC-magnetization	[224]
0.9	4	Tunnel Diode Oscillator	[227]
0.6	-	Small Angle Neutrons Scattering	[228]
0.78	1.3	Neutrons diffraction	[229]
0.57	1	Neutrons diffraction	[230]

Table 4.1: *Penetrations depths at $T = 0$ and the exponents n measured/estimated by the respective authors. Some of these authors measure various field directions or several samples, the values presented in this table correspond to the closest configuration to our experiment.*

red line in fig. 4.7(d)). The critical temperature is in good agreement with the the measurements of specific heat and susceptibility presented in fig. 4.2. The measured exponent is close to the ones reported by Signore *et al.* and Gannon *et al.*, both measured with the TDO technique (frequency of the order of MHz).

The literature reports a wide range of penetration depth: 0.6-2.3 μm, which strongly depends on the technique: 0.6-0.9 μm for μSR or neutron-based techniques [229], and 1.6-2.3 μm for inductive techniques [218, 222–224, 227]. The extrapolation of λ at $T = 0$ lays among the latter. This parameter can be also calculated from the lower critical field with $H_{c1} = \Phi_0/4\pi\lambda^2 \cdot \log \lambda/\xi$. Using $\mu_0 H_{c1}(0) = 13$ mT and $\xi(0) = 10$ nm from ref. [231], we estimate $\lambda(0) = 280$ nm, which is much lower than any value measured in the literature. This underestimation of $\lambda(0)$ was already reported by Vincent *et al.* [123]. The corresponding overestimation of H_{c1} could be related to strong resistance to vortex penetration due to the flux pinning at DWs, as it was already mentioned by some authors [206, 209].

4.4 Half-Φ_0 structures

Among the multiple scans, some structures with half of the field amplitude of single-Φ_0 vortex were detected, as presented in the scan of fig. 4.8(a). The profiles of a single-Φ_0

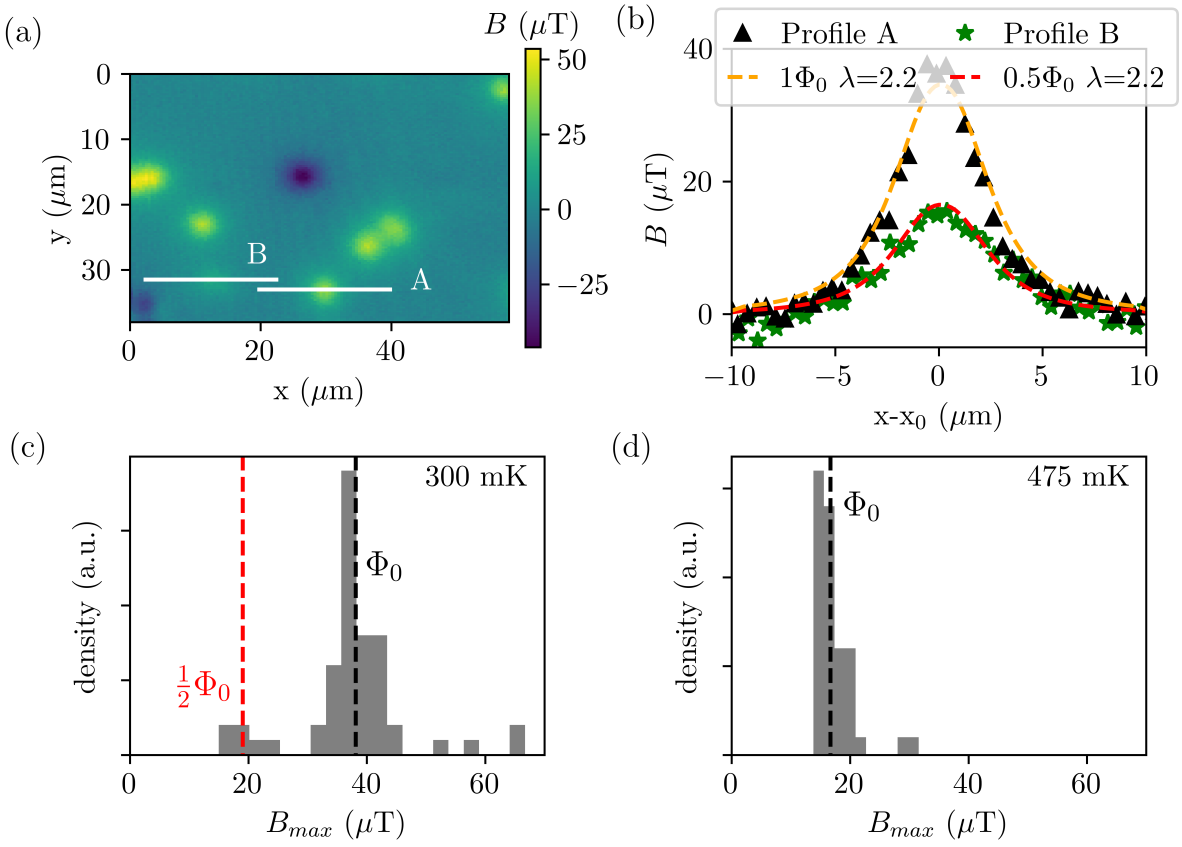

Figure 4.8: *In (a), a very low field cooling scan at 300 mK and a scanning height of 350 nm. We can observe an antivortex, some vortices and a half-Φ_0 structure. Lines A and B are profiles of one vortex and one half-Φ_0 structure, which are plotted in (b). They are presented along with a monopole profile with similar parameters, except for the flux contained in the structure. In (c) and (d), two histograms of the maximal field of structures at two different temperatures: 300 mK in (c) and 475 mK in (d). They correspond respectively to B- and A-phases.*

vortex (line A) and a half-Φ_0 structure (line B) are plotted in fig. 4.8(b), along with the curves of monopoles with the same penetration depth and same height.

In order to study this, some statistics were carried out: alternating scans at 300 mK (B-phase) and 475 mK (A-phase) after ZFC (field after compensation is $\sim$5 μT). The histograms collect the amplitude of every structure in the scans, and they are presented in fig. 4.8(c)-(d) for each temperature respectively. At 300 mK (fig. 4.8(c)), an important peak is present around 38 μT, which corresponds to the amplitude of single-Φ_0 vortices. Above this peak, we find overlapping vortices, and below there is a smaller group, with half the amplitude of the main peak (19 μT), i.e. a half-Φ_0 structure.

Thanks to the tracking of the maximal field of a vortex with the temperature (presented in fig. 4.7(d)), the peak centered 17 μT in the histogram at 475 mK (fig. 4.8(d)) corresponds to single-Φ_0 vortices at this temperature. There are some higher values, but no lower. This result tends to confirm the existence of half-Φ_0 structures in the B-phase.

Dynamics

In analogy with the vortex in fig. 4.7, I attempted to isolate one half-Φ_0 structure and

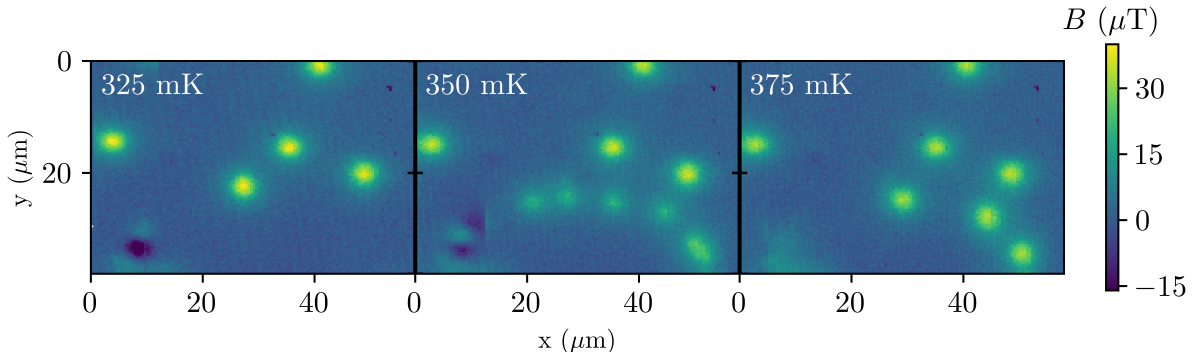

Figure 4.9: *Scans after very low field cooling. From 325 mK to 350 mK, one vortex splits into two half-Φ_0 structures and then, at 375 mK, they have recombined.*

follow the temperature behavior. This structure should not be stable in the A-phase, thus disappear/mixing into a single-Φ_0 vortex when crossing the A-B phase transition. Although this was not possible, I found the splitting of a vortex into two half-Φ_0 structures and the

later recombination into a single-Φ_0 (presented in fig. 4.9). The sample was cooled in zero field. I measured the evolution increasing the temperature, which was risen in steps of 25 mK without surpassing the set point more than 1 mK. At 325 mK (see fig. 4.9 left), we only have some vortices, but at 350 mK (see fig. 4.9 center), one of them is split in two structures, in addition of the new ones that entered our scanning range. At 375 mK (see fig. 4.9 right), the half-Φ_0 structures have reorganized in single-Φ_0 vortices again. Note that half-Φ_0 structures form a single line, and after merging vortices are align in the same line, while the other vortices didn't moved. This process of splitting-joining was already predicted by Sigrist *et al.* [208]. However, another possible scenario is that both structures are close enough that our SQUID cannot resolve them, nor detect any deformation of circular symmetry, typical for a vortex[3].

4.5 Measurement of chiral domains

In conventional type-II superconductors, vortices form a regular lattice when the vortex-vortex interaction is stronger than the vortex pinning. However in a chiral superconductor the energetic ground state is degenerate as introduced in sec. 4.1, thus, two domains can be expected. Within a given domain, superconductivity should behave as a typical type-II superconductor. The global superconducting state can either be formed by only one domain, or by domains of different chirality coexisting in the superconductor separated by DWs.

Formation of domains

The scans presented in fig. 4.10 were taken while cooling down with an applied field of -400 μT. In the A-phase, we observe irregular arrangement of flux, probably due to the small contrast. But as we cool down to the B-phase, the flux spontaneously forms a continuous line, which we attribute to be placed at the location of a DW. At the lowest temperature, the

[3] The simplest representation of a vortex in an isotropic superconductor has cylindrical symmetry, however, this is no longer true in more complex cases such as materials with anisotropy in the penetration depth or when the applied field is oblique with the surface [232]. UPt_3 shows round vortices.

DW becomes the best defined. Above and below this line, we identify individual vortices, small round flux structures which repel each other, as expected for a single ground state superconductor. On the other hand, in the vicinity of the DW the flux is more concentrated, forming accumulations and depressions (with respect to the mean field).

In particular, in fig. 4.10(e), we have that the mean field in the whole image and in the ROI inside the white box correspond to the applied field. This implies that the mean field in a single phase and in the vicinity of a DW correspond to the applied field, thus, the accumulation/depression of flux compensate themselves. Within the measurement error and within our field range, the single domains do not present a finite magnetization as theoretically expected [208].

From this figure, the currents at the origin of this field distribution could be deduced by applying the Ampère's circuital law ($\nabla \times \mathbf{B} = \mu_0 \mathbf{j}$). In fig. 4.10(f), j has two bright lobes, which seem separated by a line with no current. This line seems to define the DW, placing

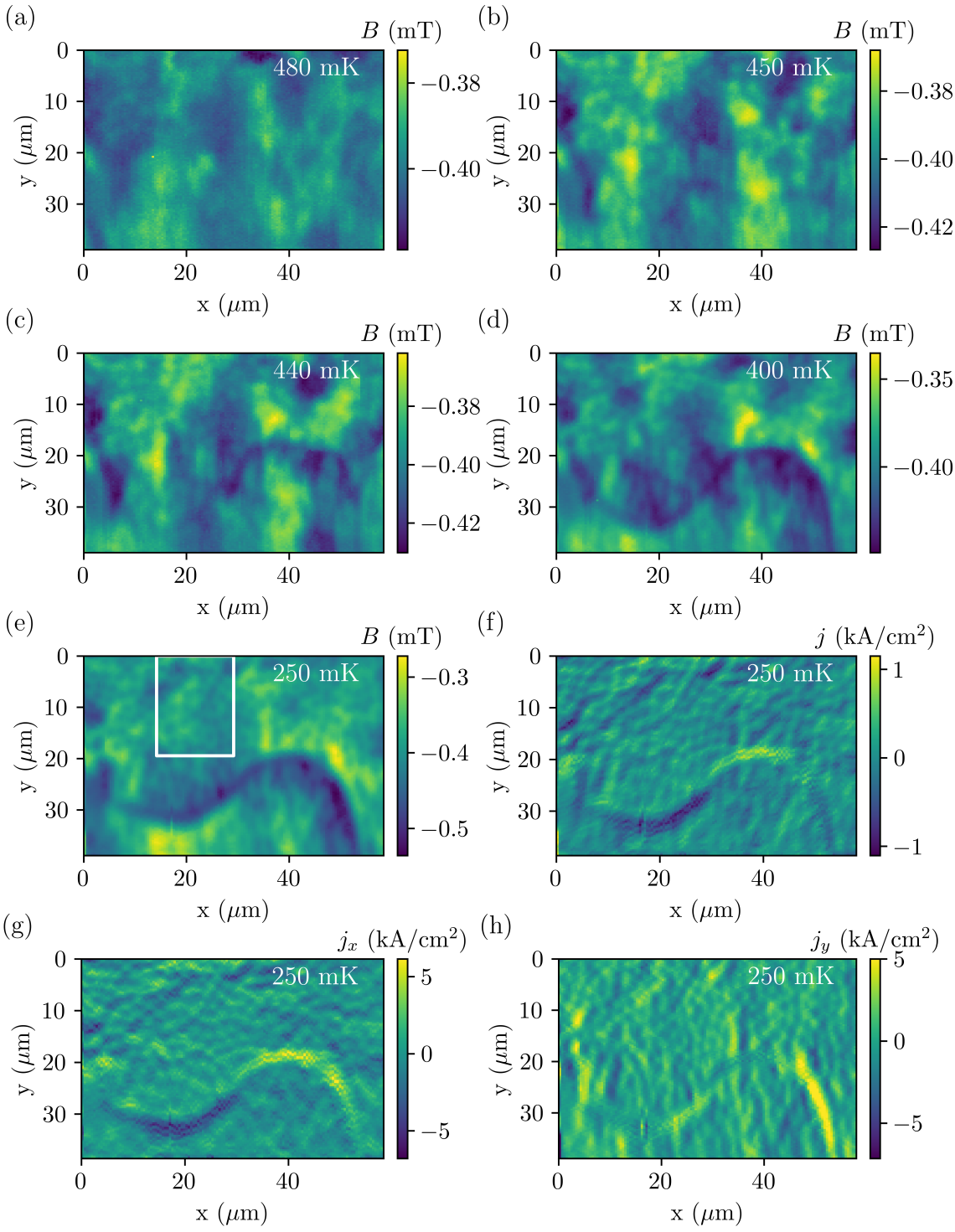

Figure 4.10: *Scans with -400 μT applied field before cooling down at a scanning height of 350 nm. The scans were taken decreasing the temperature (from the A-phase to the B-phase). Between 450 mK and 440 mK, a sinusoidal domain wall appears, which creates an unusual arrangement of the magnetic flux. At the coldest temperature (250 mK), the mean field of the whole scan matches the applied field, and the mean field of one of the two chiral phases (white ROI).*

one lobe of current density in each domain. This can be easily observed in the j_x map of fig. 4.10(g) and in the j_y map of fig. 4.10(h). The current in each lobe flows in a different direction, diverging from $(x, y) = (30, 25)$. This could be related to the change of relative phase at the domain wall, indicating that the currents flow depending of the gradient of the phase: chiral currents.

Most of the scans acquired after cooling in fields between in 0.1-1 mT present DWs and the domains sizes vary from 20 μm of diameter (see fig. 4.11(a)) to larger than our scanning range. This implies that the domains can be small enough to sometimes fit completely within our scanning window, thus, many domains are formed over the entire sample. This is in contradiction with remarks from several authors, who claim that samples of similar size are single domain [73, 74, 124, 135, 233]. Theoretically, the field should favor the domain with parallel magnetization [212], however, in our field range we only observe the magnetic decoration of the vicinity of the DW when $H > H_{c1}$ (see appendix D.1).

Domains at lower temperatures

In fig. 4.10, I show the arrangement of magnetic flux while crossing the A-B phase transition. However, this transition happens at relatively high temperatures $T/T_c \approx 0.9$, thus, the superconductivity is expected to evolve as the robustness of the superconducting state increases with decreasing the temperature. This can observed in fig. 4.11, where the temperature is increased in panels (a)-(b) and decreased in panels (c)-(d). At low temperatures UPt_3 seems to hold the flux in small domains, such as in fig. 4.11(a) and (d), while at higher temperatures domains may release it as observed in fig. 4.11(b)-(c). Each set of images (fig. 4.11(a)-(b) for increasing temperature and fig. 4.11(c)-(d) for decreasing temperature) are from independent cool downs and the presented scans were taken one after another one (one hour apart).

We could expect this to happen at the A-B phase transition, however, this happens at lower temperatures, which means that temperature plays an important role in the equilibrium between vortex repulsion and pining of vortices on the DW.

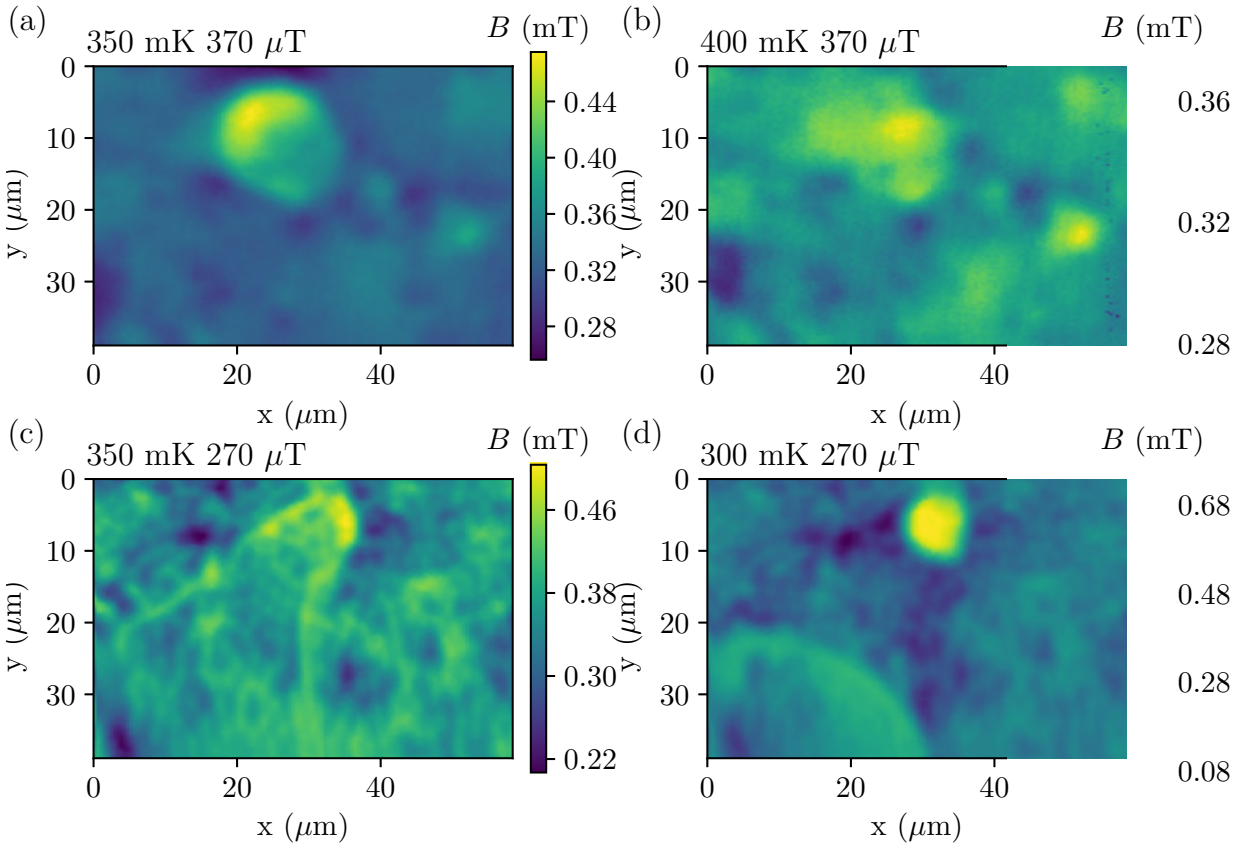

Figure 4.11: *Scans measured while warming up (at 350 mK in panel (a) and at 400 mK in panel (b)) after cooling down in 370 μT applied field . The flux is further reorganized: circular domain has opened.*

Interaction between domains

Theoretically, the energy of the DW is minimized for certain values of the relative phase between domains [208, 209]. In superconductivity we have rarely access to the phase of the order parameter, however, in the B-phase of UPt_3, the relative phase has a direct impact on the magnetic flux distribution, i.e. fractional flux structures. The measurements presented in fig. 4.12 suggest that the relative phase between domains may further define the flux organization on the DW.

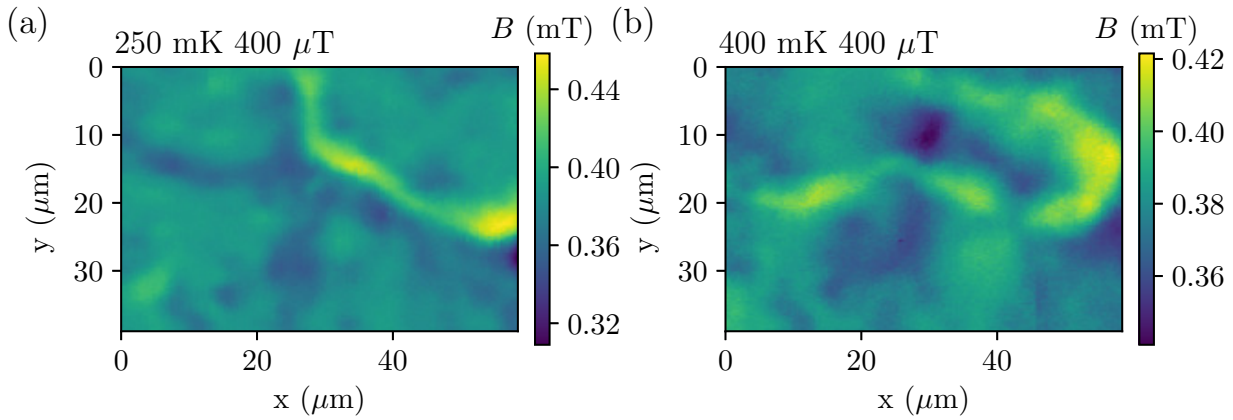

Figure 4.12: *Scans at 250 and 400 mK, after different 400 μT FC.*

In the two scans of this figure (the B-phase after different 400 μT FC), we can clearly observe that the amplitude of the flux decorating the DW oscillates within the DW. This can also be observed in fig. 4.10(e). This effect may be produced by the interaction of the domain's wavefunctions, which is reflected as an oscillation of the relative phase and its direct magnetic signature. In addition, we observe in the lobe of $(x, y) = (55, 13)$ that the period is noticeably longer, which may indicate that the oscillation depends on the curvature of the DW (domain compressibility). The periodicity of this modulation also depends on the magnetic field and probably on the temperature, however, this needs further study.

Hints for the domain wall

Fractional structures are expected to sit at the DWs, however, this link was not verified.

On the other hand, antivortices were also often found at very low fields, which sometimes they arrange with a vortex in a *dipole* such as the one presented at $(x,\ y) = (8,\ 31)$ in fig. 4.9 left. In fig. 4.9 center, half-Φ_0 structures and this *dipole* seem to form a line. In appendix D.1, I present the dependence of the field distribution at constant T after ZFC. These results also could indicate that coupled *dipoles* may hint the position of DWs at very low fields.

4.6 Conclusion and outlook

In the case of a superconductor with a complex order parameter, the ground state is degenerate with two possible states of different chirality, which individually break TRS. Using the microscope, I confirmed their coexistence in form of domains, revealed by flux decoration of DWs separating them. In the limit of the SQUID microscope's resolution, the flux is conserved in a single phase but also in the vicinity of a DW, this contradicts the local net magnetization of the domains predicted by some authors [208]. The heterogeneous distribution of magnetic flux can only be explained by the existence of an unusual current distribution flowing around domains: chiral currents.

Local magnetization measurements showed that $\mu_0 H_{c1}(T)$ is in good agreement with Vincent *et al.* [123], however, we could not observe the kink in the A-B phase transition.

The quantification of a single-Φ_0 vortex allowed us to study the temperature dependence of the penetration depth in the range from 300 to 500 mK. It follows the usual behavior $\lambda(T) = \lambda(0)/\sqrt{1-(T/T_c)^4}$ [23, 219]. The extrapolated value of $\lambda(0)$ lays within the range of reported values, but is one order of magnitude larger than the one deduced from H_{c1}.

Thanks to the quantification of a single-Φ_0 vortex, half-Φ_0 structures were detected in the B-phase. This confirms the broken TRS in the B-phase [209]. Other fractional values were not detected, but they're not excluded. Furthermore, the splitting and recombination of a single-Φ_0 vortex into two half-Φ_0 structures were observed to happen spontaneously or through minimal thermal activation. Fractional magnetic structures are expected to sit

at the DW, however, this link remains to be confirmed. Instead, the pinning of vortex-antivortex *dipoles* may hint the position of a DW.

The anomalous flux distribution around DWs and half-Φ_0 structures are first direct observations of predictions based on the interaction of two degenerate chiral domains in a TRS breaking superconductor.

In order to gain insight in the anomalous value of $H_{c1}(0)$, precise local susceptibility measurements could be performed at different spots of the sample, varying the distance to the sample's edge. If the overestimation of this parameter is caused by the magnetic flux pinning due to DWs, it would be reflected in the local susceptibility.

The measurements presented in this chapter correspond to scans above the *ab* crystallographic plane and $H \parallel c$. A similar analysis above an *ac* plane would shed light on the open question of the strength of the spin-orbit coupling of the order parameter. The application of the magnetic field in a different direction with respect to the crystallographic axis would also be instructive, as DWs may or may not follow the field. The corresponding results would be related to the question of pinning of the **d** vector to a given crystallographic axis, i.e. strong versus weak spin-orbit coupling.

The size of a domain is presumably very dependent on the quality of the crystal. The measurement of smaller samples, like whiskers, may be interesting, because they may harbor a single domain. However, this experiment is quite challenging in our setup.

The injection of electrical current would modify the dynamics of DWs at least due to the Lorentz force. The injection of currents in a setup such as the one from ref. [73] in addition of SSM would certainly reveal interesting DW dynamics.

Both STM and phase-sensitive transport measurements could explore the nature of the DW junction. However, STM experiments rely on the presence of the superconducting condensate at the very surface of the crystal and phase-sensitive transport measurements would need to control the DWs, which makes these experiments difficult. To our knowledge no

STM experiments have succeeded to image vortices in this compound.

Chapter 5

Shunted SQUIDs

Hysteretic SQUIDs (current aluminium SQUIDs) become normal whenever the current exceed the critical current. The current measurement method presented in sec. 2.1 switches off the current in a time of the order of the tens of ns. In this time, the high resistivity of the junctions combined with the bias current heat sufficiently to bring the whole SQUID in the normal state [234]. Therefore, for each measurement, the superconductivity is totally broken and in order to come back to the superconducting state, the bias current has to be set to zero. This method is rather ineffective and slow ($<$1 kHz).

The solution proposed are shunted SQUIDs (shSQUIDs) [235–240]. The general idea behind is redirecting the current when the junction becomes resistive in order to avoid the heating of the junction. More precisely, shunting the superconducting layer with a metal creates an alternative path for the current. When the applied current exceeds the critical current, it will rather go through the metal layer, which has lower resistance than the junction itself in the resistive state. This will reduce the heating and the transition will become smoother, thus, an alternating current (AC) could bias the SQUID in a quasistationary regime, i.e. each current period allows the SQUID to cool down enough so that the readout is not distorted from period to period [240]. Finally, the ideal situation would be a transition smooth enough so that we could bias with a voltage and measure the Josephson current.

5.1 State of the art

Up to today, only the hysteretic microbridge based Al SQUIDs have been used in our magnetic microscope. However some other groups succesfully fabricated non-hysteretic Nb SQUIDs with a restricted temperature range between 5 to 9 K [236–238]. Hao *et al.* [238] developped their shunted SQUIDs using Focused Ion Beam (FIB) and reached a noise level 0.2 $\mu\Phi_0/\sqrt{\text{Hz}}$. Other groups approached the problem by shunting the SQUID inductively, leading to non-hysteretic behaviors with intrisically hysteretic devices [241].

D. Hazra worked on the developpement of shunted Nb SQUIDs in our group, and achieved hysteretic SQUIDs but readable with a periodic signal, thus, the readout electronics can be greatly simplified to the use of a lock-in amplifier.

On a bare Si(100) wafer, a bilayer of 80 nm of W and 25 nm of Nb was deposited in-situ, using the magneto-sputtering technique. The SQUIDs were shaped using standard Electron Beam Lithography (EBL) and Reactive Ion Etching (RIE). SF_6 gas was used during RIE, which reacts with Nb and W, therefore, a mask of Al was previously deposited in order to protect the Nb and W of the SQUID pattern as sketched in fig. 5.1. By controlling the RIE time, one can control the thickness of the W layer, namely the shunting resistance. The SQUIDs were hysteretic at low temperatures, nevertheless, a clear and systematic $V(\Phi)$ modulation was found while biased with fixed currents above I_c. The devices could be operated within the temperature range of 230 mK to 1.5 K, and they modulated up to a field of at least 20 mT (limited by the power supply of the coil).

Fig. 5.1 shows the respective schematics of the SQUID where the W layer outside the structure has been etched partially (see fig. 5.1(a)) and where the layer has been completely etched (see fig. 5.1(b)). The reported devices had an inner size of 2x2 μm^2, the length and width of the bridges were $\sim$ 50 nm, as presented in fig. 5.1(c). He focused on SQUIDs with different W thickness, which were studied in a wide range of frequencies (13 Hz to 250 kHz). However, the data here reported were acquired at a reference frequency of 1117 Hz.

The resistance as function of the temperature were measured below 8 K for three samples

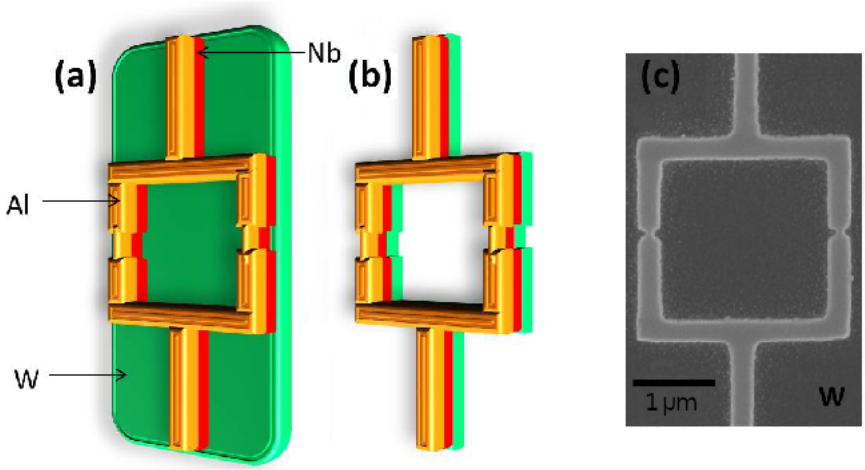

Figure 5.1: *A schema of the bilayer W-Nb SQUIDs with the mask of Al. (a) W layer is partially etched during RIE, i.e. it has some remanent W film outside the SQUID pattern, (b) W layer has been completely etched, i.e. it has no remanent W film outside the SQUID pattern. For simplicity the Si wafer is not shown in the drawing. (c) The Scanning Electron Microscope (SEM) image of a SQUID. Figure made by D. Hazra.*

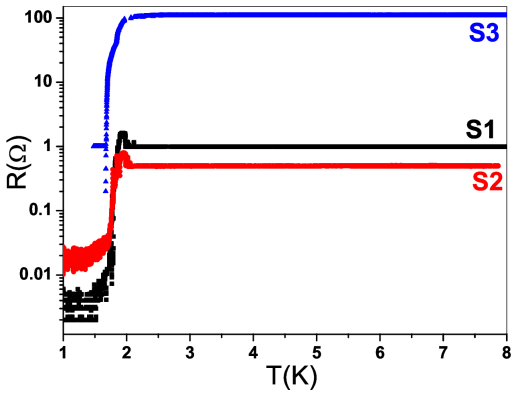

Figure 5.2: *The resistance as a function of the temperature below 8 K for three samples: partially etched (S1 and S2) and totally etched (S3). Figure is reused from ref. [242].*

with a lock-in amplifier and the results are presented in fig. 5.2. The onset of the superconducting transition for the microbridges occurred around 2 K. Samples with partially etched W layer (S1 and S2) had a lower resistance than the ones where the W layer was totally etched (S3). The transitions were quite sharp, but there's an unexplained peak just before the transition and a resistance floor of 10^{-2} Ω, which is not attributed to the noise limit of the given voltage range of the lock-in amplifier.

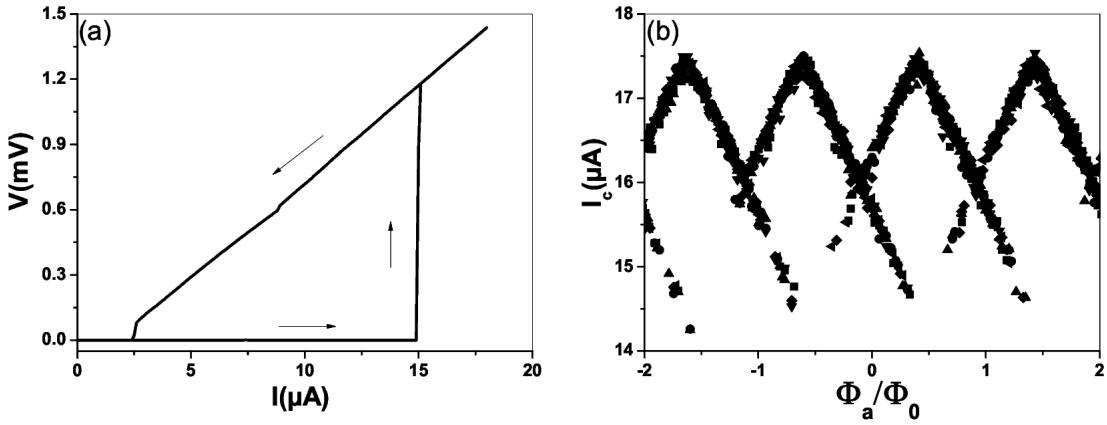

Figure 5.3: *(a) The characteristic $V(I)$ curve for S3 at 250 mK. The arrows show the direction of current sweeps, which confirm hysteresis. (b) The variation of the critical current as a function of applied magnetic flux. The Φ has been normalized with respect to Φ_0. Figure is reused from ref. [242].*

In fig. 5.3(a), we observe the hysteresis in the characteristic $V(I)$ curve of the SQUID S3 at 250 mK. The hysteresis is detected for every sample at low temperatures. For partially etched SQUIDs, the hysteresis disappears between 1-1.2 K, whereas for totally etched samples, the hysteresis remains present till 1.5 K. This confirms the role of W layer as good shunting material.

In fig. 5.3(b), the variation of the critical current of S3, I_c, as a function of magnetic flux, Φ, is observed. The crossing of the two branches of I_c and the triangular shape of $I_c(\Phi)$ indicate that the overall superconducting properties of the device are controlled by Nb and not by Al [243].

In shSQUIDs, the voltage output is also periodic in flux. In fig. 5.4(a), the modulation of S3 is presented for various bias currents at 250 mK. The sensitivity of the SQUID is given by the derivative of the curve $V(\Phi)$. The sensitivity with a bias of 11.2 μA can be observed in fig. 5.4(b). The maximum field sensitivity is around 1.5 mV/Φ_0.

The noise level was estimated using the Fast-Fourier-Transform (FFT) of the output voltage sequence. The experimental setup reaches the white noise floor at 5 Hz with a value of $S_V(f) = 10$ nV/$\sqrt{\text{Hz}}$, which is probably the limit of the room temperature bias resis-

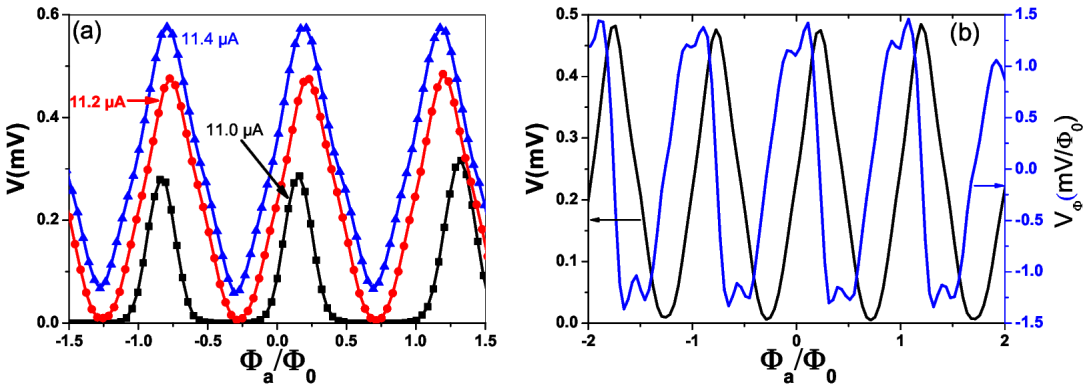

Figure 5.4: *(a) The voltage modulation as a function of externally applied flux Φ at 250 mK for S3 for three different bias currents. (b) In black (left axis), the curve $V(\Phi)$ for 11.2 μA of bias current presented in (a), along with the voltage sensitivity of the latter (blue curve in right axis). The current and voltage magnitudes referred here are in rms unit. Figure is reused from ref. [242].*

tor. The flux noise of a SQUID can be estimated using the sensitivity, presented in blue in fig. 5.4(b). With a maximal value of 1.5 mV/Φ_0 for the sample S3 at 1 K, the maximal flux sensitivity that could be reached in these conditions is $S_\Phi(f) = 6.7\ \mu\Phi_0/\sqrt{\text{Hz}}$, however the obtained sensitivity is more than one order of magnitude lower: $S_\Phi(f) = 50\mu\Phi_0/\sqrt{\text{Hz}}$ [242].

To sum up, we shall highlight the following results:

- SQUIDs present hysteresis at low temperatures, however, they are readable with an AC signal up to 250 kHz at least. This implies faster reading and great simplification of the electronics.
- The resistance of totally etched SQUIDs is around 100 Ω for his SQUID design. The sensitivity of the SQUIDs was measured to be 1.5 mV/Φ_0.
- The modulation is mainly governed by the Nb SQUID.

5.2 Points to consider

- Shunting a superconductor with a metal implies several things. (i) The current will go through the path of least resistance, thus when the superconductivity is broken, the current will go through the metal. (ii) The possible heat produced by the current and the non-zero resistance will spread out easier than without the shunting. (iii) Due to proximity effect, the superconductor electron density increases, which is directly related with the reduction of the critical superconducting parameters: I_c and T_c [244]. **Current Al SQUIDs have a $\mathbf{T_c = 1.2}$ K and $\mathbf{I_c(0) = 70}$ μA, shunting them would result in a lower $\mathbf{T_c}$ and $\mathbf{I_c}$, which is undesired for measuring. Nb SQUIDs, with a $\mathbf{T_c = 9}$ K and $\mathbf{I_c(0) \sim 1}$ mA, seem more propitious for being shunted, usually with tungsten**[1].

- The high resistance of the junctions cause enough heating to turn the whole hysteretic SQUID resistive. Current scanning SQUIDs have a junction resistance of 100 Ω. **The goal is shunting the junction to reach 1-10 Ω. However, as the SQUID is current-biased, a balance has to be determined because the higher the resistance the higher the voltage difference measured.**

- Another important task is to find the limiting factor of the sensitivity. The noise of the current Al SQUIDs is $S_I \sim 8$ nA/$\sqrt{\text{Hz}}$, which corresponds to a noise of 1 μV/$\sqrt{\text{Hz}}$ at the SQUID, whereas the Nb shSQUIDs from previous work were measured in a setup with a floor noise of $S_V = 10$ nV/$\sqrt{\text{Hz}}$. Therefore, **the analysis of noise is mandatory in order to improve the sensibility of our probes.**

  One of the most ubiquitous noise sources is the Johnson-Nyquist noise. The voltage

[1] The critical current depends on the flux going through the loop but also on the temperature. The lower $t = T/T_c$, the more insensible the critical current is to temperature variations. For example, given a Ginzburg-Landau dependence $I_c(t) \propto (1-t)^{3/2}$ [23, 145, 245], a variation of 1 mK at 300 mK in an Al SQUID would result in a variation in critical current of 0.1% of the modulation. In a Nb SQUID the same variation of temperature at the same temperature would give a variation in the current of ∼0.02% of the modulation.

noise, S_v^{th}, is given by

$$S_v^{th} = \sqrt{4k_B T R} \qquad (\mathrm{V}/\sqrt{\mathrm{Hz}}) \tag{5.1}$$

where R is a resistance and T its temperature. In the current scanning SQUIDs, the main source of thermal noise is the room temperature bias resistor ($R_{bias} = 25$ kΩ): $S_v^{th} = 20$ nV$/\sqrt{\mathrm{Hz}}$, which gives a current noise of $S_I^{th} = 0.8$ pA$/\sqrt{\mathrm{Hz}}$. Another known source of noise comes from discretization of the charge, called shot noise:

$$S_I^s = \sqrt{2eI} \qquad (\mathrm{A}/\sqrt{\mathrm{Hz}}) \tag{5.2}$$

where e is the electron charge and I the current. In our SQUIDs, this source contributes with $S_I^s = 5$ pA$/\sqrt{\mathrm{Hz}}$. Another source comes from temperature instabilities of the refrigerator, which impact the critical current of SQUID. Fluctuations of the order of 100 μK$/\sqrt{\mathrm{Hz}}$ at 300 mK gives an error of critical current of 7.5 nA$/\sqrt{\mathrm{Hz}}$ [2], which seems of the order of magnitude of the current noise found in the scanning SQUIDs. In order to fully take advantage of the low intrinsic noise of the SQUIDs, the temperature must be stabilized.

In order to transform it to flux noise we have to take into account the self-induction of the SQUID and the sensitivity of the SQUID (slope of the I_c modulation arcs). For the current scanning SQUIDs (see fig. 2.1 right), the self-induction is $L = 2$ pH and the slope is $\partial I_c/\partial\Phi = 43 - 125$ μA$/\Phi_0$. Therefore, considering a current noise of $S_I = 8$ nA$/\sqrt{\mathrm{Hz}}$, the noise in flux due to the self-induction is $S_\Phi^{si} = 8$ $\mu\Phi_0/\sqrt{\mathrm{Hz}}$ and due to the sensitivity of the SQUID is $S_\Phi^{sens} = 0.2 - 0.6$ m$\Phi_0/\sqrt{\mathrm{Hz}}$. The first one is negligible in front of the second one, which limits the whole sensitivity of the device.

One last noise source to consider is the magnetic noise, S_B, which comes from different sources such as bad-screened electronics, radio-frequency devices, coil driving current, etc. Although I didn't measure this noise in detail, the dispersion of measurements

[2] This value was estimated from a Ginzburg-Landau behavior: $I_c(T) = I_c(0)(1 - T/T_c)^{1.5}$ [23, 145, 245]. With the conditions mentioned, the obtained error is 0.01%, which for $I_c(0) = 70$ μA results in a noise of $S_I = 7.5$ nA$/\sqrt{\mathrm{Hz}}$.

above a superconductor and above a no superconductor are similar. Thus, magnetic noise is not an important contribution to the measured noise, at least in the low frequency regime. To transform it into S_Φ we would need to multiply S_B by the effective area of the SQUID loop.

5.3 Methods

5.3.1 Fabrication

Shunted SQUID samples consist of a bilayer of 80 nm of W and 25 nm of Nb, with an Al mask of 20 nm. The bilayer was grown in-situ by E. André (Néel Institut - CNRS, now LP3 - CNRS) using the magnetron sputtering technique. At a pressure of 10^{-3} mbar and 390°C, the tungsten was deposited at a rate of 1.1 Å/s and the niobium at 1.7 Å/s in the same vacuum.

The SQUID patterns were shaped using standard EBL and thermal evaporation for the deposition of the Al mask. Then, the RIE was applied to the trilayer and it was stopped at the beginning of the W layer. T. Crozes heavily worked in the analysis of the effects (etching speed, anisotropy, ...) of the different RIE programs (SF_6 with or without alternance of SiN, use or not of O_2 plasma, ...), which affect directly to the sizes and quality of the microbridges and the thickness of tungsten layer. The smallest microbrigdes were 25 - 30 nm large and the W layer thickness $\sim$75 nm. The rest of the lithography work was also done by T. Crozes (Néel Institut - CNRS).

Finally, in order to be closest to the scanning configuration, the SQUIDs were as deep etched as the scanning SQUIDs by A. Barbier (IRAM - Grenoble).

5.3.2 Measurements

Cryostat

Measurement of these SQUIDs were made in other cryostat than the one presented in sec. 2.2. The SQUIDs can be cooled down to 200 mK. The temperature is measured and

controlled by a TRMC2.

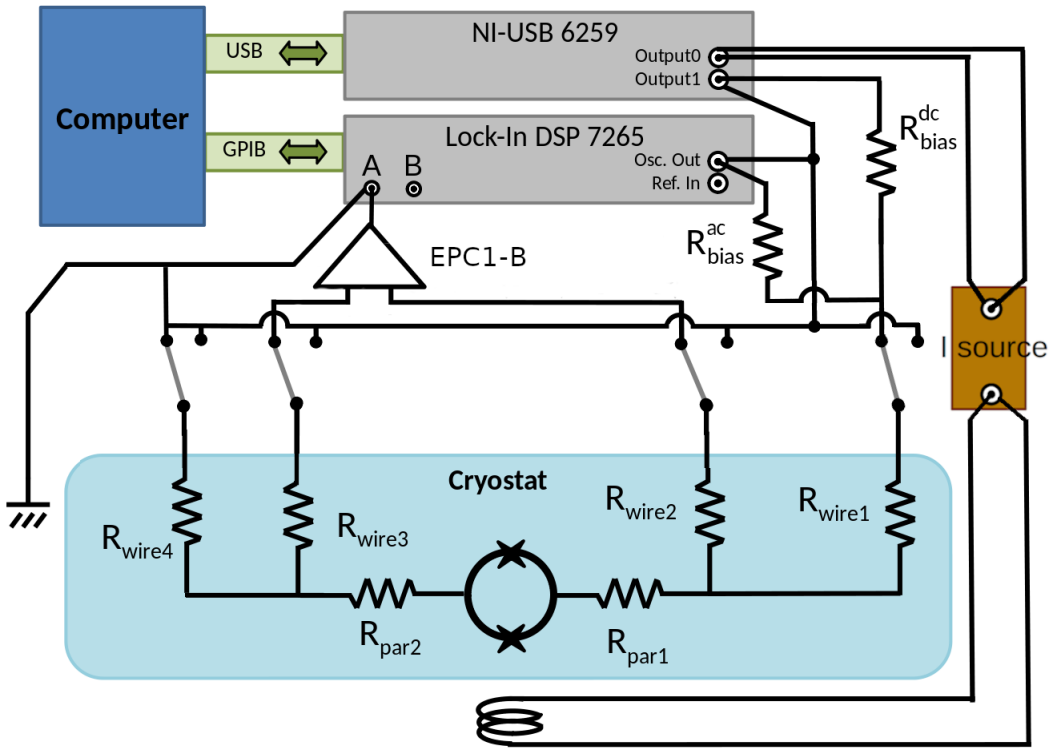

Figure 5.5: *The voltage sources are the NI-USB 6259 for the direct current (DC) and the Signal Recovery 7265 DSP lock-in amplifier for the AC signal. Each signal has a bias resistor before entering in the cryostat. There is also a switch for every wire before they go down to the SQUID chip. Samples are measured with the 4-point resistance method. The EPC1-B amplifies differentially the output signal before the lock-in amplifier. The control and read-out of both devices are made through the computer. Another output of the NI-USB drives the current source for the resistive coil.*

Electronics

There are 12 twisted pairs of wires for measurements with π filters [246] just before the connection to the sample holder. The sample holder has 24 golden pins to microbond the SQUID samples.

The field is applied by an external resistive coil controlled by a homemade current source, commanded with the NI-USB 6259. All the samples are placed on the center of the coil, so

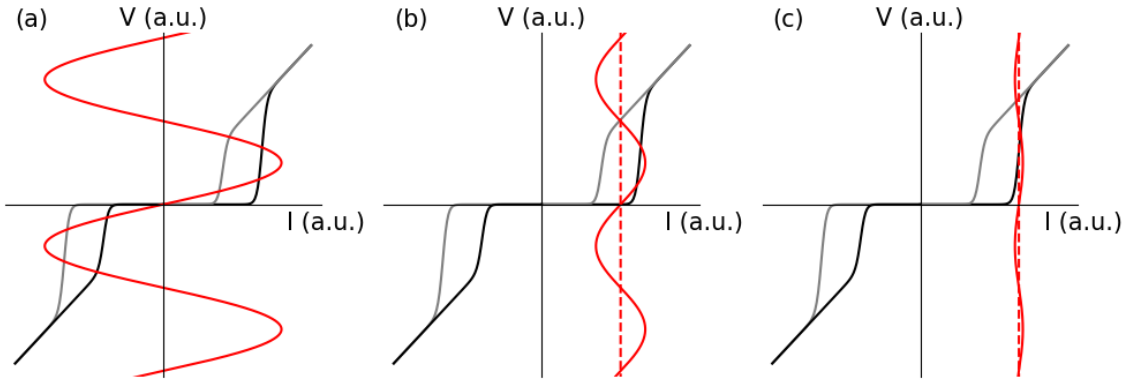

Figure 5.6: *Schema of the three AC methods: (a) DC is zero, and the AC covers the $I_c > 0$ and the $I_c < 0$ transitions resulting in a symmetric modulation. In (b) I^{DC} sits on the middle the $I_c(B)$ modulation, with an AC signal that covers the whole $I_c(B)$ modulation. In (c), I^{DC} sits just above the maximal $I_c(B)$ with an small AC, which results in the R^{AC} measurement.*

that they all see the same field.

All the measurements presented in this chapter were carried out in current bias, with the bias resistors at room temperature. The measurement circuit is presented in fig. 5.5:

1. The AC signal was created by the internal oscillator of the Signal Recovery 7265 DSP lock-in amplifier.

2. A direct current (DC) signal can be added, which is created by NI-USB 6259. This device also creates the voltage to control the current source driving the coil.

3. Room-temperature bias resistors convert the voltage signals into current.

4. The signal goes through the SQUIDs.

5. The output is connected to the ground and to the amplifier EPC1-B, which makes a differential amplification as sketched in fig. 5.5. For the first experiments the 4-point measurement is carried out at the microbonding pads level, and for the presented results, it is carried out within the chip.

6. The output of the amplifier enters the lock-in amplifier.

The lock-in, NI-USB and TRMC2 are controlled and read with the computer.

Depending on the DC and AC injected in the SQUID, we could imagine three different regimes sketched in fig. 5.6. The first method (a) consists of measuring with only an AC (see fig. 5.6(a)), the signal oscillates from negative to positive voltage and viceversa. As presented in appendix A, the $I_c(\Phi)$ arcs of these SQUIDs are tilted to one side (asymmetric modulation) and by permuting the injection and ground pads, the modulation curve tilts to the other side. In this case, the lock-in integrates the values of the critical current when is positive and when it's negative, therefore the asymmetry of the SQUID's modulation curve is averaged and the corresponding amplitude is reduced.

When I^{DC} is injected along with an I^{AC}, we have two scenarios. The method (b) consists of I^{DC} sitting on the middle the $I_c(B)$ modulation, with an AC signal that covers the whole $I_c(\Phi)$ modulation as sketched in fig. 5.6(b). This method preserves the asymmetry of the $I_c(\Phi)$ curve and is more sensitive than the method (a). In the method (c), I^{DC} sits just above the maximal $I_c(\Phi)$, with a small AC signal. The result is the slope of the $V(I)$ curve at I^{DC}, namely the resistance. It would be really sensitive at the transition, however, the modulation amplitude decreases rapidly when we move away from the transition. Furthermore, as the amplitude is proportional to the input signal, the output will be much smaller than previous methods.

The temperature dependence of the critical current was measured with AC amplitude of 1 μA. The measurements of $R(T)$ were done with $I^{DC} = 0$. The $V(I)$ curves presented in the sec. 5.4 were measured with $I^{AC} = 0$ and the modulation curves $R^{AC}(H)$ were measured with method (c). All of them were measured with a 4-point resistance method, in particular, for the results presented in next section the 4-point measurement happens within the chip.

5.4 Results

All the samples used in the following experiments have the same initial thicknesses of the recipe of D. Hazra: 80 nm W, 25 nm Nb and 20 nm Al. However, the W layer was left mainly untouched (70 - 80 nm of thickness).

Figure 5.7: *First set of shSQUIDs measured after they were RIEed and some of them FIBed. The clearest parts is the Al mask, the darker grey is the W layer. Even darker grey (all around Al masks in the left and right images) is the Si wafer. The size of each image is 120x90 μm^2.*

First shSQUIDs that I measured had a T_c around 7 K, but also a parasitic resistance in the superconducting state ($\sim 0.1\ \Omega$) and very low sensitivity ($\sim 0.1\ \mu V/\Phi_0$). A large shunt was suspected to be the reason. To resolve this problem, the shunting between the current lines in the chip was cut: the unshunting lines were fabricated with RIE until $\sim$15 μm from the SQUID loop and some of them were also continued with FIB until 300 nm of the SQUID loop. Results confirmed the hypothesis but FIBed SQUIDs couldn't be compared due to technical problems[3] (see fig. 5.7).

Next set of measurements were done with a new design of SQUID (see fig. 5.8). In previous measurements, the 4-point measurement was done in the microbonding pads, whereas now it is done in the device itself, at $\sim$450 μm of the loop (indicated with an arrow in fig. 5.8(a)). The goal of this modification is to remove the parasitic superconducting resistance, because we remove the microbonding resistance and the circuit between the 4 points

[3] The RIEed and FIBed SQUIDs were the same SQUIDs as previous measurements. The edges of the deep etching prevented the lithography resist to spread uniformly, which is directly related to the low controllability of the RIE. In next SQUID fabrication, the separation of the current lines with RIE was carried out before the deep etching step.

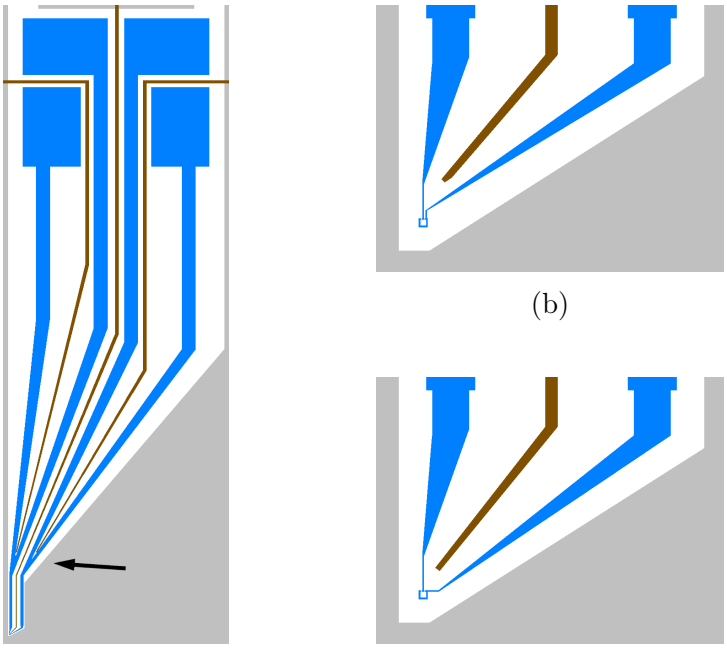

Figure 5.8: *The two versions of a chip of shSQUID with inner loop surface of 1 μm^2. In (a) we observe the 4 pads (blue) to measure with the 4-point probes method. They joint into 2 current lines at $\sim$ 450 μm of the loop (indicated with an arrow). Brown lines are the paths of the RIE for unshunting the current lines. White is the W layer. The light grey is the Si wafer after deep etching. In (b), the pattern of the parallel current lines (PaCL) and in (c) the pattern of perpendicular current lines (PeCL). They differ only in the part presented in (b) and (c), the rest of the chip is similar. In (a), the width of the W layer is 640 μm and the length of the same is 2.25 mm. In (b) and (c), the W layer width is 50 μm and length to the contact-tip 39 μm.*

is superconducting. Furthermore, in order to gain insight into the shunting behavior close to the loop, two different patterns for the current lines were studied: parallel current lines (PaCL) sketched in fig. 5.8(b) and perpendicular current lines (PeCL) sketched in fig. 5.8(c). For these new patterns, the unshunting lines etch with RIE (see brown zones in fig. 5.8) were carried out after the Nb etching and before the deep etching.

Numerical analysis performed on COMSOL Multiphysics[4] show the importance of the

[4] The electrodynamics equations were solved in the stationary state for the SQUID geometries presented in fig. 5.8(b)-(c). Blue paths were considered superconducting (square resistance of 1 mΩ for sake of the simulation) and white regions had a square resistance of 3 Ω. In the simulation I took the situation where the junction already transited, thus the resistance of the normal state is extremely large compared with the W layer resistance that was not considered in the simulation. I examined the case with and without

current lines separation, by comparing the cases with and without shunting lines. The resistance of the latter is half the one with shunting lines (see figs. 5.9(a)-(d)). Therefore, we can infer that the lack of unshunting lines in the whole chip has shunted excessively the SQUID.

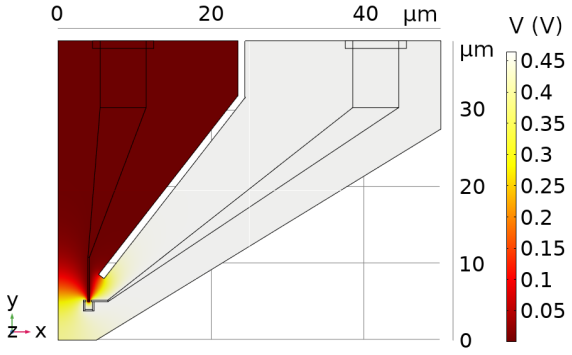

(a) *PeCL separated with RIE.*

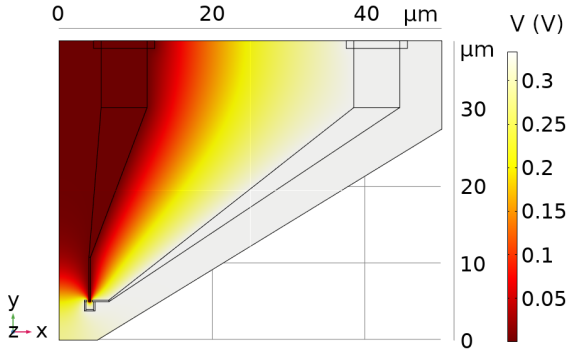

(b) *PeCL not separated with RIE.*

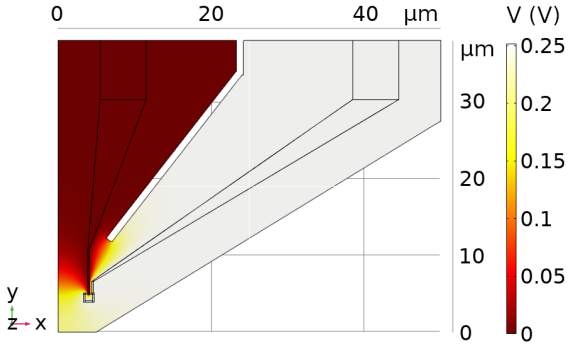

(c) *PaCL separated with RIE.*

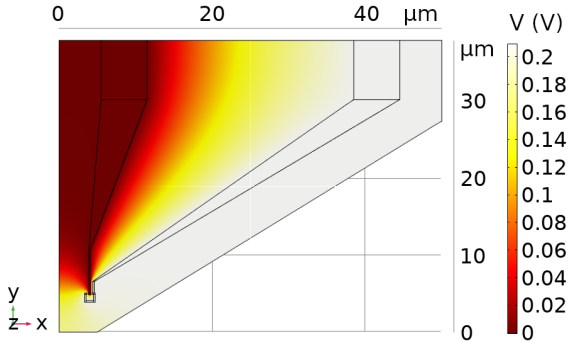

(d) *PaCL not separated with RIE.*

Figure 5.9: *Stationary simulations in COMSOL Multiphysics of the voltage decay in the two different configurations with or without unshunting lines. The square resistance of the W layer was taken as 3 Ω. The superconducting layer square resistance was taken as 1 mΩ for numerical sake. The dimensions are the same of the real SQUIDs. The input current is 1 A.*

The resistive transition as a function of the temperature presents a very large transition (1 K) in several steps as we can observe in fig. 5.10. This probably corresponds to inhomo-

unshunting lines (brown lines in fig. 5.8(b)-(c)) for each geometry. As the parameters are constant in the simulation, an ampere of current was injected in one superconducting path and the other one was connected to ground. I considered a realistic square resistance of 3 Ω for the W layer (at room temperature it is 5 Ω and previous experiments measured a RRR of 1-2 for similar layers).

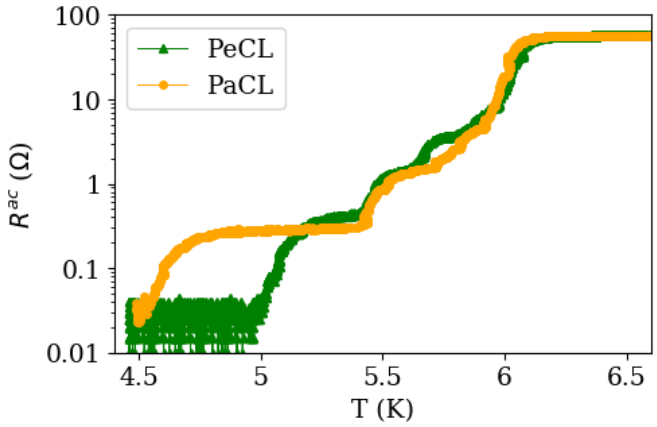

Figure 5.10: *Dynamic resistance as a function of the temperature for two shSQUIDs of different geometry.* $I^{AC} = 1\ \mu A$ *was applied while the samples were cooled with no applied field.*

geneities in the shunting layer or due to anisotropy of the etching below the Al mask. At high temperatures the resistance is similar in both devices (∼65 Ω), at lower temperatures (around 5.4 K) a plateau of resistance is measured with values of 0.4 and 0.3 Ω for the PeCL and PaCL devices respectively. At lower temperatures, a last transition to the superconducting state happens, which is attributed to the microbridge transition. The residual resistance of 40 mΩ probably corresponds to the thermal noise level of the room temperature bias resistor (100 kΩ, however it is close to the digital noise of the lock-in amplifier (10mΩ). Furthermore, the width of the transition is well reproducible as all the studied samples (with different patterns and from different wafers) present the same smooth transition in several steps, however, the microbridges transition temperature varies from SQUID to SQUID without relation to the geometry nor the wafer.

The characteristic $V(I)$ curve of each SQUID was measured with a DC signal for different fields[5]. One example of each geometry is presented: PeCL in fig. 5.11(a) and for PaCL in fig. 5.11(b). For each SQUID, the $V(I)$ curve is plotted for 4 different fields, which correspond to the maximal and minimal critical current for positive and negative currents.

[5] The amplifier for DC add itself an offset and a slope to the measured signal. For the results presented in fig. 5.11, the offset and slope were subtracted so that the resistance is zero when superconducting.

The critical currents lay between 100-200 μA and the results don't show any I_c difference between the geometries. Furthermore, both devices show small hysteresis of $\sim$2 μA. On the other hand, the resistance in the normal state (0.45 Ω for PeCL and 0.25 Ω for PaCL) distinguishes both geometries. These values are in good agreement with the simulations presented in fig. 5.9. This confirms that the resistance measured in the SQUID is mainly due to the W layer and it can be easily controlled by the proximity of the unshunting line to the SQUID loop.

From the $V(I)$ curves, we can estimate the modulation amplitude for current and voltage bias. For the PeCL device, a DC bias at 210 μA results in voltage oscillation with amplitude of 10 μV, and a direct voltage bias of 10 μV would result in current oscillation of amplitude 25 μA. For the PaCL device, a current bias of 155 μA results in voltage oscillations of 5 μV and a direct voltage bias of 5 μV would result in current oscillations of amplitude 20 μA.

If they were measured with the method (c) (see fig. 5.6(c)), the amplitude in voltage is the difference of dynamic resistances between the maximal and minimal $I_c(B)$ times the I^{AC}: $\Delta V = I^{AC}_{bias}\Delta R^{AC}$. For the device with PeCL with bias currents of $I^{DC} = 210$ μA and $I^{AC} = 1$ μA, the resistance varies from 0.9 Ω to 0.35 Ω, resulting in a voltage amplitude of $\Delta V = 550$ nV. Similarly for SQUIDs with PaCL: with $I^{DC} = 155$ μA and $I^{AC} = 1$ μA, the resistance varies from 0.6 Ω to 0.25 Ω, resulting in a voltage amplitude of $\Delta V = 350$ nV.

The field modulation, $R^{AC}(H)$, of both geometries is presented in fig. 5.12 for different DC bias, along with the respective sensitivities. The AC amplitude was fixed at 1 μA [6]. For the device with PeCL presented in fig. 5.12(a), the field modulation has an amplitude of 270 nV for $I^{DC} = 220$ μA [7]. We observe that the amplitude and sensitivity (see right of fig. 5.12(a)) importantly decrease as increasing the I^{DC} bias. The maximal sensitivity for this SQUID is 1.6 $\mu V/\Phi_0$ for 220 μA, three orders of magnitude smaller than the results of

[6] The I^{AC} bias is relatively large, however, I verified that the value of $R^{AC}(B)$ does not change for AC values from 100 nA to 1 μA. As the signal is proportional to the I^{AC}, I measured with 1 μA.

[7] The amplitude of modulation depends on the proximity of the bias current to the maximal critical current, which for this device is 208 μA. The estimation of the amplitude made in the previous paragraph was 550 nV for 210 μA of DC bias. The same estimation for a bias of 220 μA is $\Delta V = I^{AC}_{bias}\Delta R^{AC} \approx 1000 \cdot (0.65 - 0.35) = 650 - 350 = 300$ nV, which correspond with upper and lower limit of the modulation.

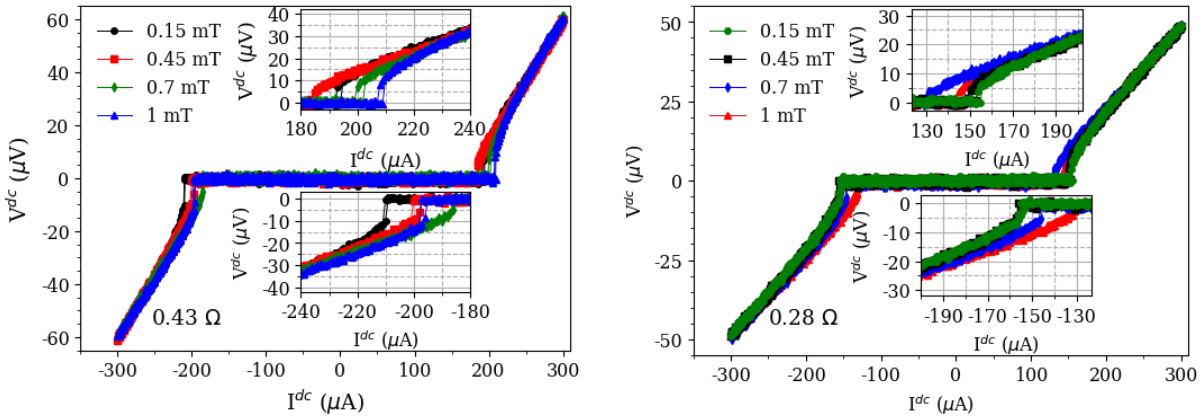

(a) *Perpendicular current lines (PeCL).* (b) *Parallel current lines (PaCL).*

Figure 5.11: *Characteristic $V(I)$ curves measured with a DC bias at 250 mK for different fields and for both geometries. The fields were chosen in order to minimize and maximize the critical current for $I_c > 0$ and $I_c < 0$.*

D. Hazra.

For the device with PaCL presented in fig. 5.12(b), 160 μA bias results in a modulation with amplitude of 235 nV [8]. For this SQUID, the maximal sensitivity is 0.9 $\mu V/\Phi_0$ for a bias of 160 μA as we can observe on the right of fig. 5.12(b).

5.5 Conclusion

In the first place we identified the excessive shunting between the current lines. Consequently I designed the new configuration where the 4-point measurement occurs in the chip and all the current lines are separated with RIE grooves. Two geometries of current lines were fabricated in order to modify the shunting resistance with the same W layer thickness.

Measurements have shown that the normal resistance of the microbridges is 0.25-0.45 Ω depending on the pattern of the current lines. These values were reproduced with sim-

[8] The amplitude of modulation depends on the proximity of the bias current to the maximal critical current, which for this device is 154 μA. The estimation of the amplitude made in the previous paragraph was 350 nV for 155 μA of DC bias. The same estimation for a bias of 160 μA is $\Delta V = I^{AC}_{bias}\Delta R^{AC} \approx 1000 \cdot (0.45 - 0.225) = 450 - 200 = 250$ nV, which correspond with upper and lower limit of the modulation.

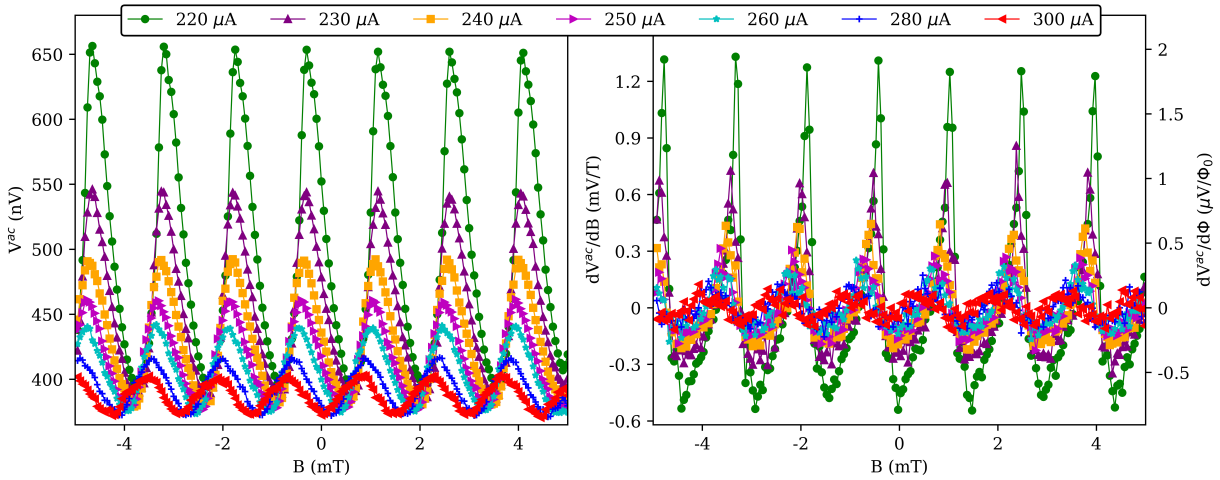

(a) *Perpendicular current lines (PeCL).*

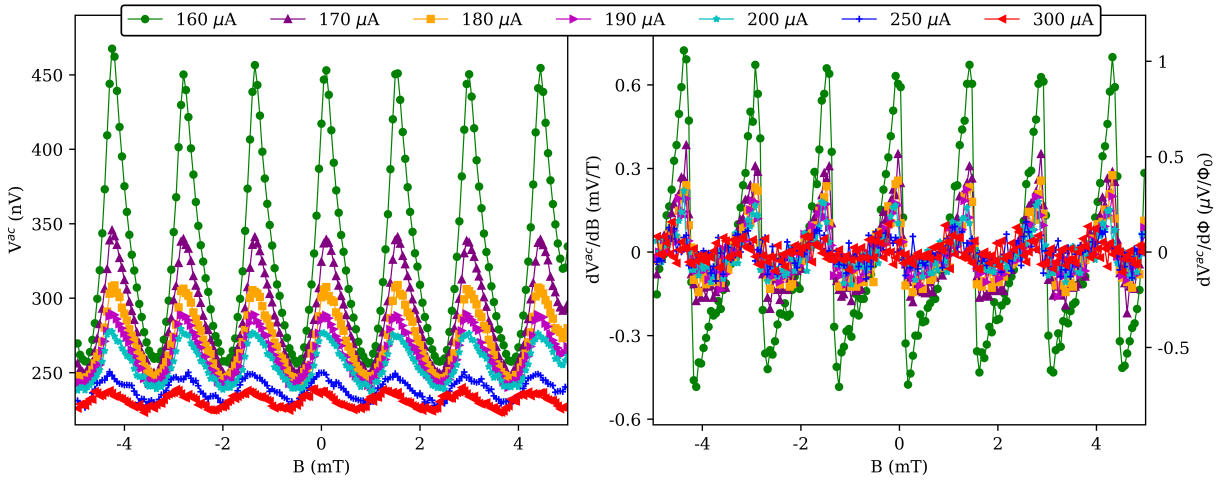

(b) *Parallel current lines (PaCL).*

Figure 5.12: *Characteristic $V^{AC}(H)$ curves measured with $I^{AC} = 1\ \mu A$ and for different I^{DC} bias at 250 mK for both geometries. The minimal I^{DC} was chosen as the first one to modulate measuring every 10 μA.*

ulations. Without fine-tuning the bias I^{DC}, the maximal sensitivities achieved with these SQUIDs are 0.9 and 1.6 $\mu V/\Phi_0$ respectively. Hazra's SQUIDs had shorter junctions and totally etched W layer. He measured a normal-state resistance of 100 Ω (200 times our SQUID's resistance), obtaining a sensitivity of more than two orders of magnitude. Furthermore, $V(I)$ characteristic curves present critical current of 100 - 200 μA, with a small hysteresis, however, he had critical currents of 10 - 20 μA but larger hysteresis. These results

compare SQUIDs with fully-etched and almost-not-etched W layers, which encourage the further study of these devices in order to maximize the sensibility as a function of the shunt.

5.6 Outlook

Development of SQUIDs

The modulation amplitude of the measured devices (method (c)) is rather small, and it's directly related to the difference between the normal-state resistances of the maximal and minimal $I_c(B)$. A normal-state resistance of $\sim$ 10 - 100 Ω should be fabricated so as to obtain a sensitivity of 100-1000 $\mu V/\Phi_0$. This resistance can be easily increased by more etching of the W layer. Previous work of D. Hazra [242] support this hypothesis, however, a balance between sensitivity and dissipation must be found.

Right now, some hysteresis is present as observed in $V(I)$ curves from fig. 5.11, however, we are able to measure quasistatically with current bias at $f \approx 1$ kHz. Faster signals should be studied to find the high-frequency limit for reading these SQUIDs.

Another important modification that must be done in Nb SQUIDs is shortening the junctions. The modulation amplitude strongly depends on the ratio length of the microbridge, S, over coherence length, ξ. As this ratio approaches 1, the modulation amplitude increases [243]. Aluminium has a clean (dirty) limit coherence length of 1.2 (0.1) μm and the Nb's respective is 39 (17) nm [243, 247, 248]. As indicated in sec. 2.1, our microbridges are 200 nm long and the ratios S/ξ are 0.5 for Al and 10 for the Nb, resulting in modulations $\Delta I_c/2I_0$ of 44% for Al and 5% for Nb. Another possibility of reducing this ratio is to grow thicker Nb films, however, the critical current would increase too. A balance of sensibility and dissipation should be studied, nonetheless, the latter shall not be examined right away.

Measurement of SQUIDs

In fig. 5.6 we have seen 3 differents methods to measure the SQUID. They should be compared as they have advantages and inconveniences.

- Method (a) loses the asymmetry of the SQUID's modulation, the setup is the simplest as we don't need a DC source, but the amplitude of modulation depends strongly on I_c.

- Method (b) keeps the asymmetry of the SQUID's modulation and the amplitude of modulation does not depend on the critical current.

- Method (c) keeps the asymmetry of the SQUID's modulation and the amplitude of modulation does not depend on the critical current. This method tries to exploit the sharpness of the $R^{AC}(I)$ transition, however, the readout signal is proportional to the I^{AC}, usually small.

Another open question is whether to use current or voltage for biasing the SQUIDs. So far, the current bias works fine for testing. If this bias is chosen for the scanning setup, the implementation of a low temperature bias resistors should be considered in order to reduce the thermal voltage noise at least $S_v^{300K}/S_v^{1K} = \sqrt{300} \sim 17$ times.

In order to bias in voltage, a small bias resistor should be placed in parallel with the measuring shSQUID. The current amplifier should be put in series with the SQUID but in parallel with the bias resistor as sketched in fig. 5.13. As current amplifier, a SQUID array amplifier (SAA) is often used [238, 249, 250], because of the low impedance input and low current noise (<10 pA/$\sqrt{\text{Hz}}$ at 4 K [251]). A SAA consists of an array of SQUIDs in series which are magnetically coupled to a coil, through which the current-to-amplify flows, in our case the SQUID current (see fig. 5.13). The SQUID series can also be coupled to a compensating coil, which forces the SQUID array to work in the most effective point of the modulation curve. However, they must placed at a low temperatures and the control of the device depends on several parameters (compensation coils, bias currents, ...), on which the gain depends [251]. In order to reach the best sensitivity and being able to measure the actual intrinsic noise of the SQUIDs, a direct coupling of the SQUID with low temperature flux transformer like the SAA is essential [237, 238].

A quick estimation of signal-to-noise ratio shall shed light in this question. In the sec. 5.4, the PaCL SQUID had an amplitude of 5 μV for 155 μA of bias. The EPC1-B voltage amplifier has a floor noise around 0.6 nV/$\sqrt{\text{Hz}}$, which gives a signal-to-noise ratio of 5 μV/0.5 nV = 10^4. The estimation for 5 μV of voltage bias was 20 μA, which gives a ratio of 20 μA/10 pA = $2 \cdot 10^6$. Furthermore, with voltage bias, the dissipation power is limited ($P = V_{bias}^2/R$). Thus, from these estimations voltage biased SQUIDs seem promising.

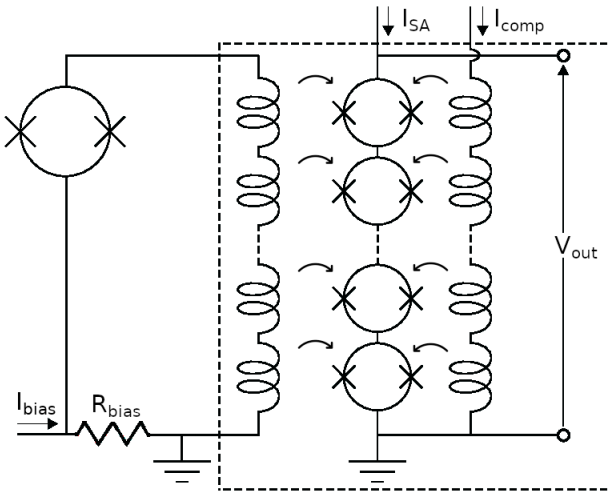

Figure 5.13: *Electric circuit proposed for voltage bias the measuring SQUID. The single SQUID (left) is the scanning SQUID, which is shunted with the bias resistor. In series with the scanning SQUID and inside the SAA device (dashed line), there is the input coil. This coil is magnetically coupled to the SQUID array, which is current biased. The SQUID array is also coupled to a compensation coil in order to operate always in the most effective point of the SQUID's modulation. The output is the voltage drop in the SQUID array. Such amplifiers are used in several groups [238, 249–251].*

Chapter 6

Conclusion

In this manuscript I have described the new results of my work. I used a scanning SQUID microscope to shed light on the nature of the superconducting state of UPt_3 and $PdTe_2$ measuring the magnetic field distribution with a sub-micron spatial resolution and a sub $m\Phi_0/\sqrt{Hz}$ magnetic resolution.

I used micro SQUIDs as probe of the magnetic flux. These SQUIDs are very simple and robust, they consists of a monolayer of aluminum structured using high resolution e-beam lithography. Current biased they show thermal hysteresis which results in a slow read-out. For this reason I made progress in the development and characterization of shunted SQUIDs. These new SQUIDs are composed of a bilayer of W-Nb which show small or no hysteresis. These probes can be read continuously with an AC drive using a low noise preamplifier and a lock-in amplifier.

$PdTe_2$ is a type-I superconductor presenting intermediate state. We measured the field distribution and the temperature and field dependence, revealing magnetic tubes at low field and laminae at higher fields. We also observed superconducting tubes enclosed in intermediate state regions. These observations were compared with the model of Clem *et al.* and Goren and Tinkham, which allowed us to deduce the interface width, an important parameter of the energetic description of this state. The results here presented support type-I superconductivity and give a possible explanation for the observation of vortices, claimed by some groups.

UPt_3 is a type-II superconductor well known for his three superconducting phases. After having acquired a substantial set data I analyzed the magnetic field distribution in UPt_3 when it is cooled to the low field region of the phase diagram. Thus I could reveal the magnetic decoration of the chiral domains in the B-phase. The currents generating the magnetic field distribution at the domain walls flow in different directions depending on the domain, confirming the chiral currents. Furthermore, I was able to identify spontaneous half-Φ_0 structures in a monocrystal, the first observed in these conditions. Due to the interaction between domains, these structures were expected to appear at the domain walls. Vortex seem to decay to half-Φ_0 structures and the corresponding recombination seem to happen with minimal thermal activation. Further evidence of the interaction between domains is the modulation of amplitude of the field pinned at the domain wall. The results presented in this manuscript reveal important features of the chiral superconductor UPt_3, most of them predicted by theory but never observed before. My observations and analysis open a new field for the study of chiral superconductivity.

Bibliography

[1] K. Onnes *Leiden Comm.*, vol. 120b, 1911.

[2] W. Meissner and R. Ochsenfeld *Naturwissenschaften*, vol. 21, p. 787, 1933.

[3] F. London and H. London *Proc. Roy. Soc. Lond.*, vol. A149, p. 71, 1935.

[4] L. Landau *J. Exp. Theor. Phys.*, vol. 7, pp. 19–32, 1937. from "Collected Papers of L.D. Landau".

[5] V. L. Ginzburg and L. D. Landau *J. Exp. Theor. Phys.*, vol. 20, p. 1064, 1950.

[6] A. A. Abrikosov *J. Exp. Theor. Phys.*, vol. 32, p. 1141, 1957.

[7] J. Bardeen, L. N. Cooper, and J. Schrieffer *Phys. Rev.*, vol. 106, pp. 162–164, 1957.

[8] J. Bardeen, L. N. Cooper, and J. Schrieffer *Phys. Rev.*, vol. 108, p. 1175, 1957.

[9] H. Fröhlich *Proc. Phys. Soc.*, vol. A63, p. 778, 1950.

[10] E. Maxwell *Phys. Rev.*, vol. 78, p. 477, 1950.

[11] C. Reynolds, B. Serin, W. Wright, and L. Nesbitt *Phys. Rev.*, vol. 78, p. 487, 1950.

[12] L. Cooper *Phys. Rev.*, vol. 104, pp. 1189–1190, 1956.

[13] W. A. Little and R. D. Parks *Phys. Rev. Lett.*, vol. 9, pp. 9–12, July 1962.

[14] B. Josephson *Phys. Lett.*, vol. 1, no. 7, pp. 251–253, 1962.

[15] P. W. Anderson and J. M. Rowell *Phys. Rev. Lett.*, vol. 10, pp. 230–232, Mar 1963.

[16] F. Steglich, J. Aarts, C. D. Bredl, W. Lieke, D. Meschede, W. Franz, and H. Schäfer *Phys. Rev. Lett.*, vol. 43, pp. 1892–1896, Dec 1979.

[17] P. J. Ray. Master's thesis. Niels Bohr Institute, University of Copenhague, Feb. 2016.

[18] M. Somayazulu, M. Ahart, A. K. Mishra, Z. M. Geballe, M. Baldini, Y. Meng, V. V. Struzhkin, and R. J. Hemley *Phys. Rev. Lett.*, vol. 122, p. 027001, Jan. 2019.

[19] A. P. Drozdov, P. P. Kong, V. S. Minkov, S. P. Besedin, M. A. Kuzovnikov, S. Mozaffari, L. Balicas, F. F. Balakirev, D. E. Graf, V. B. Prakapenka, E. Greenberg, D. A. Knyazev, M. Tkacz, and M. I. Eremets *Nature*, vol. 569, pp. 528–531, Feb. 2019.

[20] E. Snider, N. Dasenbrock-Gammon, R. McBride, M. Debessai, H. Vindana, K. Vencatasamy, K. V. Lawler, A. Salamat, and R. P. Dias *Nature*, vol. 586, pp. 373–377, 2020.

[21] E. Snider, N. Dasenbrock-Gammon, R. McBride, X. Wang, N. Meyers, K. V. Lawler, E. Zurek, A. Salamat, and R. P. Dias *Phys. Rev. Lett.*, vol. 126, p. 117003, Mar. 2021.

[22] L. Landau *J. Phys. U.S.S.R.*, vol. 11, no. 129, 1937.

[23] M. Tinkham, *Introduction to Superconductivity.* Dover Publications, Mineola, New York, 2004.

[24] P. G. de Gennes, *Superconductivity of metals and alloys.* W. A. Benjamin, 1966.

[25] M. Oettinger, "http://oettinger-physics.de."

[26] A. A. Abrikosov *J. Exp. Theor. Phys.*, vol. 5, no. 6, p. 1174, 1957.

[27] J. Clarke and A. I. Braginski, *The SQUID Handbook Fundamentals and Technology of SQUIDs and SQUID Systems*, vol. 1. Weinheim: Wiley-VCH, 2006.

[28] L. P. Gor'kov *J. Exp. Theor. Phys.*, vol. 36, p. 1918, 1959.

[29] P. L. Richards and M. Tinkham *Phys. Rev.*, vol. 119, pp. 575–590, Jul 1960.

[30] G. M. Eliashberg *J. Exp. Theor. Phys.*, vol. 38, p. 966, 1960.

[31] W. L. McMillan *Phys. Rev.*, vol. 167, p. 331–344, 1968.

[32] G. R. Stewart *Adv. Phys.*, vol. 66, pp. 75–196, Apr. 2017.

[33] P. Mangin and R. Kahn, *Superconductivity: an introduction*. Springer, 2017.

[34] D. Manske, *Theory of Unconventional Superconductors*. Springer, 2004.

[35] G. E. Volovik and L. P. Gor'kov *J. Exp. Theor. Phys.*, vol. 61, pp. 843–854, 1985.

[36] D. Tilley and J. Tilley, *Superfluidity and superconductivity*. Adam Hilger Ltd, 1986.

[37] Y. Maeno, S. Kittaka, T. Nomura, S. Yonezawa, and K. Ishida *J. Phys. Soc. Jpn*, vol. 81, no. 1, p. 011009, 2012.

[38] V. P. Mineev and K. V. Samokhin, *Introduction to Unconventional Superconductivity*. Gordon and Breach Science Publishers, 1999.

[39] J. Bednorz and K. Mueller *Z. Phys. B*, vol. 64, p. 189, 1986.

[40] M. K. Wu, J. R. Ashburn, C. J. Torng, P. H. Hor, R. L. Meng, L. Gao, Z. J. Huang, Y. Q. Wang, and C. W. Chu *Phys. Rev. Lett.*, vol. 58, pp. 908–910, Mar 1987.

[41] H. Maeda, Y. Tanaka, M. Fukutomi, and T. Asano *Japanese J. Appl. Phys.*, vol. 27, pp. L209–L210, feb 1988.

[42] P. Dai, B. Chakoumakos, G. Sun, K. Wong, Y. Xin, and D. Lu *Physica C: supercond.*, vol. 243, no. 3, pp. 201–206, 1995.

[43] L. Gao, Y. Y. Xue, F. Chen, Q. Xiong, R. L. Meng, D. Ramirez, C. W. Chu, J. H. Eggert, and H. K. Mao *Phys. Rev. B*, vol. 50, pp. 4260–4263, Aug 1994.

[44] A. Lebed, *The Physics of Organic Superconductors and Conductors*. Springer, 2008.

[45] D. Jérome, A. Mazaud, M. Ribault, and K. Bechgaard *J. Phys. Lett.*, vol. 41, no. 4, pp. 95–98, 1980.

[46] C. Pennington and V. Stenger *Rev. Mod. Phys.*, vol. 68, p. 885, 1996.

[47] Z. K. Tang, L. Zhang, N. Wang, X. X. Zhang, G. H. Wen, G. D. Li, J. N. Wang, C. T. Chan, and P. Sheng *Science*, vol. 292, p. 2462, 2001.

[48] Y. Cao, V. Fatemi, S. Fang, K. Watanabe, T. Taniguchi, E. Kaxiras, and P. Jarillo-Herrero *Nature*, vol. 556, pp. 43–50, Avr. 2018.

[49] Y. Kamihara, H. Hiramatsu, M. Hirano, R. Kawamura, H. Yanagi, T. Kamiya, and H. Hosono *J. Am. Chem. Soc.*, vol. 128, no. 31, pp. 10012–10013, 2006.

[50] F. Hunte, J. Jaroszynski, A. Gurevich, D. C. Larbalestier, R. Jin, A. S. Sefat, M. A. McGuire, B. C. Sales, D. K. Christen, and D. Mandrus *Nature*, vol. 453, pp. 903–905, June 2008.

[51] H. R. Ott, H. Rudigier, Z. Fisk, and J. L. Smith *Phys. Rev. Lett.*, vol. 50, pp. 1595–1598, May 1983.

[52] Y. Shimizu, D. Braithwaite, D. Aoki, B. Salce, and J.-P. Brison *Phys. Rev. Lett.*, vol. 122, p. 067001, Feb 2019.

[53] G. R. Stewart, Z. Fisk, J. O. Willis, and J. L. Smith *Phys. Rev. Lett.*, vol. 52, pp. 679–682, Feb 1984.

[54] T. T. M. Palstra, A. A. Menovsky, J. v. d. Berg, A. J. Dirkmaat, P. H. Kes, G. J. Nieuwenhuys, and J. A. Mydosh *Phys. Rev. Lett.*, vol. 55, pp. 2727–2730, Dec 1985.

[55] C. Geibel, C.and Schank, S. Thies, H. Kitazawa, C. D. Bredl, A. Böhm, M. Rau, A. Grauel, R. Caspary, R. Helfrich, U. Ahlheim, G. Weber, and F. Steglich *Z. Phys. B Condens. Matter*, vol. 84, pp. 1–2, Feb. 1991.

[56] C. Geibel, S. Thies, D. Kaczorowski, A. Mehner, A. Grauel, B. Seidel, U. Ahlheim, R. Helfrich, K. Petersen, C. D. Bredl, and F. Steglich *Z. Phys. B Condens. Matter*, vol. 83, pp. 305–306, Oct. 1991.

[57] D. Jaccard, K. Behnia, and J. Sierro *Phys. Lett. A*, vol. 163, no. 5, pp. 475–480, 1992.

[58] N. Huy, A. Gasparini, D. de Nijs, Y. Huang, J. Klaasse, T. Gortenmulder, A. de Visser, A. Hamann, T. Goerlach, and H. Loehneysen *Phys. Rev. Lett.*, vol. 99, p. 067006, 2007.

[59] S. S. Saxena, P. Agarwal, K. Ahilan, F. M. Grosche, R. K. W. Haselwimmer, M. J. Steiner, E. Pugh, I. R. Walker, S. R. Julian, P. Monthoux, G. G. Lonzarich, A. Huxley, I. Sheikin, D. Braithwaite, and J. Flouquet *Nature*, vol. 406, pp. 587–592, Aug. 2000.

[60] C. Petrovic, P. G. Pagliuso, M. F. Hundley, R. Movshovich, J. L. Sarrao, J. D. Thompson, Z. Fisk, and P. Monthoux *J. Phys. Condens. Matter*, vol. 13, pp. L337–L342, apr 2001.

[61] F. Steglich, C. Geibel, K. Gloos, G. Olesch, C. Schank, C. Wassilew, A. Loidl, A. Krimmel, and G. R. Stewart *J. Low Temp. Phys.*, vol. 95, pp. 3–22, Apr. 1994.

[62] H. H. Hill *Nucl. Met., Met. Soc.*, vol. 17, pp. 2–19, 1 1970.

[63] S. Doniach *Physica B+C*, vol. 91, pp. 231–234, 1977.

[64] G. Aeppli, E. Bucher, C. Broholm, J. K. Kjems, J. Baumann, and J. Hufnagl *Phys. Rev. Lett.*, vol. 60, pp. 615–618, Feb. 1988.

[65] R. Joynt and L. Taillefer *Rev. Mod. Phys.*, vol. 74, pp. 235–294, Mar 2002.

[66] E. Thuneberg, "Superfluid ^{3}He." `http://ltl.tkk.fi/research/theory/he3.html`, Aug. 2003.

[67] A. Huxley, P. Rodière, D. M. Paul, N. van Dijk, R. Cubitt, and J. Flouquet *Nature*, vol. 406, pp. 160–164, July 2000.

[68] J. A. Sauls *Adv. Phys.*, vol. 43, no. 1, pp. 113–141, 1994.

[69] M. Sigrist *Physica B Condens. Matter*, vol. 280, no. 1, pp. 154–158, 2000.

[70] Y. Tsutsumi, K. Machida, T. Ohmi, and M. Ozaki *J. Phys. Soc. Jpn*, vol. 81, no. 7, p. 074717, 2012.

[71] P. D. de Réotier, A. Huxley, A. Yaouanc, J. Flouquet, P. Bonville, P. Imbert, P. Pari, P. C. M. Gubbens, and A. M. Mulders *Phys. Lett. A*, vol. 205, pp. 239–243, Sept. 1995.

[72] N. Keller, J. L. Tholence, A. Huxley, and J. Flouquet *Phys. Rev. Lett.*, vol. 73, pp. 2364–2367, Oct. 1994.

[73] J. D. Strand, D. J. Bahr, D. J. van Harlingen, J. P. Davis, W. J. Gannon, and W. P. Halperin *Science*, vol. 328, pp. 1368–1369, June 2010.

[74] Y. Machida, A. Itoh, Y. So, K. Izawa, Y. Haga, E. Yamamoto, N. Kimura, Y. Onuki, Y. Tsutsumi, and K. Machida *Phys. Rev. Lett.*, vol. 108, p. 157002, Apr. 2012.

[75] B. S. Shivaram, T. F. Rosenbaum, and D. G. Hinks *Phys. Rev. Lett.*, vol. 57, pp. 1259–1262, Sept. 1986.

[76] H. Suderow, J. P. Brison, A. Huxley, and J. Flouquet *J. Low Temp. Phys.*, vol. 108, pp. 11–30, Jul 1997.

[77] T. Sakakibara, S. Kittaka, and K. Machida *Rep. Prog. Phys.*, vol. 79, p. 094002, Aug. 2016.

[78] Y. Kohori, M. Kyogaku, T. Kohara, K. Asayama, H. Amitsuka, and Y. Miyako *Physica B Condens. Matter*, vol. 165-166, pp. 381–382, Aug. 1990.

[79] K. A. Park and R. Joynt *Phys. Rev. Lett.*, vol. 74, pp. 4734–4737, June 1995.

[80] W. O. Putikka and R. Joynt *Phys. Rev. B*, vol. 37, pp. 2372–2375, Feb 1988.

[81] W. O. Putikka and R. Joynt *Phys. Rev. B*, vol. 39, pp. 701–704, Jan 1989.

[82] C. H. Choi and J. A. Sauls *Phys. Rev. Lett.*, vol. 66, pp. 484–487, Jan 1991.

[83] G. Haran, P. J. Hirschfeld, and M. Sigrist *J. Low Temp. Phys.*, vol. 111, pp. 73–98, Apr. 1998.

[84] K. Machida and M. Ozaki *J. Phys. Soc. Jpn.*, vol. 58, pp. 2244–2247, July 1989.

[85] E. D. Isaacs, P. Zschack, C. L. Broholm, C. Burns, G. Aeppli, A. P. Ramirez, T. T. M. Palstra, R. W. Erwin, N. Stücheli, and E. Bucher *Phys. Rev. Lett.*, vol. 75, pp. 1178–1181, Aug. 1995.

[86] K. Machida and M. Ozaki *Phys. Rev. Lett.*, vol. 66, pp. 3293–3296, June 1991.

[87] S. Kittaka, K. An, T. Sakakibara, Y. Haga, E. Yamamoto, N. Kimura, Y. Ōnuki, and K. Machida *J. Phys. Conf. Ser.*, vol. 391, p. 012031, Dec. 2012.

[88] R. Joynt *J. Phys. Condens. Matter*, vol. 2, pp. 3415–3420, Apr 1990.

[89] D.-C. Chen and A. Garg *Phys. Rev. Lett.*, vol. 70, pp. 1689–1692, Mar 1993.

[90] M. E. Zhitomirsky and K. Ueda *Phys. Rev. B*, vol. 53, pp. 6591–6604, Mar 1996.

[91] J. P. Brison, N. Keller, P. Lejay, A. Huxley, L. Schmidt, A. Buzdin, N. R. Bernhoeft, I. Mineev, A. N. Stepanov, J. Flouquet, D. Jaccard, S. R. Julian, and G. G. Lonzarich *Physica B Condens. Matter*, vol. 199-200, pp. 70 – 75, 1994.

[92] D. Coffey and C. J. Pethick *Phys. Rev. B*, vol. 33, pp. 7508–7513, June 1986.

[93] J. J. M. Franse, P. H. Frings, A. de Visser, A. Menovsky, T. T. M. Palstra, P. H. Kes, and J. A. Mydosh *Physica B+C*, vol. 126, pp. 116–125, Nov. 1984.

[94] K. Hasselbach, A. Lacerda, K. Behnia, L. Taillefer, J. Flouquet, and A. de Visser *J. Low Temp. Phys.*, vol. 81, pp. 299–315, Dec. 1990.

[95] F. Pobell, *Matter and Methods at Low Temperatures.* Springer-Verlag Berlin Heidelberg, 2007.

[96] G. R. Stewart *Rev. Mod. Phys.*, vol. 56, pp. 755–787, Oct 1984.

[97] G. J. McMullan, P. M. C. Rourke, M. R. Norman, A. D. Huxley, N. Doiron-Leyraud, J. Flouquet, G. G. Lonzarich, A. McCollam, and S. R. Julian *New J. Phys.*, vol. 10, p. 053029, May 2008.

[98] T. Ito, H. Kumigashira, H.-D. Kim, T. Takahashi, N. Kimura, Y. Haga, E. Yamamoto, Y. Ōnuki, and H. Harima *Phys. Rev. B*, vol. 59, pp. 8923–8929, Apr. 1999.

[99] L. Taillefer, R. Newbury, G. G. Lonzarich, Z. Fisk, and J. L. Smith *J. Magn. Magn. Mater.*, vol. 63-64, pp. 372 – 376, 1987.

[100] L. Taillefer and G. G. Lonzarich *Phys. Rev. Lett.*, vol. 60, pp. 1570–1573, Apr 1988.

[101] N. Kimura, R. Settai, Y. Ōnuki, H. Toshima, E. Yamamoto, K. Maezawa, H. Aoki, and H. Harima *J. Phys. Soc. Jpn*, vol. 64, no. 10, pp. 3881–3889, 1995.

[102] N. Kimura, R. Settai, Y. Ōnuki, K. Maezawa, H. Aoki, and H. Harima *Physica B Condens. Matter*, vol. 216, pp. 313–315, Jan. 1996.

[103] G. Zwicknagl, A. N. Yaresko, and P. Fulde *Phys. Rev. B*, vol. 65, p. 081103, Feb 2002.

[104] C. Kallin and J. Berlinsky *Rep. Prog. Phys.*, vol. 79, p. 054502, May 2016.

[105] R. C. Albers, A. M. Boring, and N. E. Christensen *Phys. Rev. B*, vol. 33, pp. 8116–8129, June 1986.

[106] M. R. Norman, R. C. Albers, A. M. Boring, and N. E. Christensen *Solid State Commun.*, vol. 68, no. 2, pp. 245 – 249, 1988.

[107] A. de Visser, J. J. M. Franse, and A. Menovsky *J. Magn. Magn. Mater.*, vol. 43, pp. 43 – 47, June 1984.

[108] P. H. Frings, J. J. M. Franse, F. R. de Boer, and A. Menovsky *J. Magn. Magn. Mater.*, vol. 31-34, pp. 240 – 242, Feb 1983.

[109] H. Tou, Y. Kitaoka, K. Asayama, N. Kimura, Y. Ōnuki, E. Yamamoto, and K. Maezawa *Phys. Rev. Lett.*, vol. 77, pp. 1374–1377, Aug 1996.

[110] G. Aeppli, E. Bucher, A. I. Goldman, G. Shirane, C. Broholm, and J. K. Kjems *J. Magn. Magn. Mater.*, vol. 76-77, pp. 385 – 390, 1988.

[111] R. H. Heffner, D. W. Cooke, A. L. Giorgi, R. L. Hutson, M. E. Schillaci, H. D. Rempp, J. L. Smith, J. O. Willis, D. E. MacLaughlin, C. Boekema, R. L. Lichti, J. Oostens, and A. B. Denison *Phys. Rev. B*, vol. 39, pp. 11345–11357, June 1989.

[112] S. M. Hayden, L. Taillefer, C. Vettier, and J. Flouquet *Phys. Rev. B*, vol. 46, pp. 8675–8678, Oct 1992.

[113] R. J. Keizer, A. de Visser, A. A. Menovsky, J. J. M. Franse, B. Fåk, and J.-M. Mignot *Phys. Rev. B*, vol. 60, pp. 6668–6677, Sept. 1999.

[114] T. Aoyama, H. Kotegawa, H. Tou, N. Kimura, Y. Haga, E. Yamamoto, and Y. Ōnuki *Physica B Condens. Matter*, vol. 570, pp. 349–351, Oct. 2019.

[115] A. Sulpice, P. Gandit, J. Chaussy, J. Flouquet, D. Jaccard, P. Lejay, and J. L. Tholence *J. Low Temp. Phys.*, vol. 62, pp. 39–54, Feb. 1986.

[116] K. Hasselbach, L. Taillefer, and J. Flouquet *Phys. Rev. Lett.*, vol. 63, pp. 93–96, July 1989.

[117] V. Müller, C. Roth, D. Maurer, E. W. Scheidt, K. Lüders, E. Bucher, and H. E. Bömmel *Phys. Rev. Lett.*, vol. 58, pp. 1224–1227, Mar 1987.

[118] R. A. Fisher, S. Kim, B. F. Woodfield, N. E. Phillips, L. Taillefer, K. Hasselbach, J. Flouquet, A. L. Giorgi, and J. L. Smith *Phys. Rev. Lett.*, vol. 62, pp. 1411–1414, Mar 1989.

[119] S. Adenwalla, S. W. Lin, Q. Z. Ran, Z. Zhao, J. B. Ketterson, J. A. Sauls, L. Taillefer, D. G. Hinks, M. Levy, and B. K. Sarma *Phys. Rev. Lett.*, vol. 65, pp. 2298–2301, Oct. 1990.

[120] J. W. Chen, S. E. Lambert, M. B. Maple, Z. Fisk, J. L. Smith, G. R. Stewart, and J. O. Willis *Phys. Rev. B*, vol. 30, pp. 1583–1585, Aug 1984.

[121] B. S. Shivaram, J. J. Gannon, and D. G. Hinks *Phys. Rev. Lett.*, vol. 63, pp. 1723–1726, Oct. 1989.

[122] Z. Zhao, F. Behroozi, J. B. Ketterson, Y. Guan, B. K. Sarmat, and D. G. Hinks *Physica B Condens. Matter*, vol. 165-166, pp. 345–346, Aug. 1990.

[123] E. Vincent, J. Hammann, L. Taillefer, K. Behnia, N. Keller, and J. Flouquet *J. Phys. Condens. Matter*, vol. 3, pp. 3517–3525, May 1991.

[124] E. R. Schemm, W. J. Gannon, C. M. Wishne, W. P. Halperin, and A. Kapitulnik *Science*, vol. 345, no. 6193, 2014.

[125] H. Tou, Y. Kitaoka, K. Ishida, K. Asayama, N. Kimura, Y. Ōnuki, E. Yamamoto, Y. Haga, and K. Maezawa *Phys. Rev. Lett.*, vol. 80, pp. 3129–3132, Apr. 1998.

[126] T. Trappmann, H. van Löhneysen, and L. Taillefer *Phys. Rev. B*, vol. 43, pp. 13714–13716, June 1991.

[127] H. van Löhneysen, T. Trappmann, and L. Taillefer *J. Magn. Magn. Mater.*, vol. 108, no. 1, pp. 49 – 50, 1992.

[128] D. S. Jin, S. A. Carter, B. Ellman, T. F. Rosenbaum, and D. G. Hinks *Phys. Rev. Lett.*, vol. 68, pp. 1597–1600, Mar 1992.

[129] M. Greiter, G. G. Lonzarich, and L. Taillefer *Phys. Lett. A*, vol. 169, pp. 199–204, Sept. 1992.

[130] A. Kapitulnik *Physica B Condens. Matter*, vol. 460, pp. 151–158, 2015.

[131] S. B. Etter, W. Huang, and M. Sigrist *New J. Phys.*, vol. 22, p. 093038, sep 2020.

[132] W. J. Gannon, W. P. Halperin, M. R. Eskildsen, P. Dai, U. B. Hansen, K. Lefmann, and A. Stunault *Phys. Rev. B*, vol. 96, July 2017.

[133] T. Aoyama, H. Kotegawa, N. Kimura, E. Yamamoto, Y. Haga, Y. Ōnuki, and H. Tou *J. Phys. Soc. Jpn.*, vol. 88, p. 064706, May 2019.

[134] Y. Kitaoka, H. Tou, K. Ishida, N. Kimura, Y. Ōnuki, E. Yamamoto, Y. Haga, and K. Maezawa *Physica B Condens. Matter*, vol. 281-282, pp. 878–881, 2000.

[135] M. J. Graf, S.-K. Yip, and J. A. Sauls *Phys. Rev. B*, vol. 62, pp. 14393–14402, Dec 2000.

[136] H. Suderow, J. P. Brison, A. Huxley, and J. Flouquet *Phys. Rev. Lett.*, vol. 80, pp. 165–168, Jan. 1998.

[137] B. Lussier, B. Ellman, and L. Taillefer *Phys. Rev. B*, vol. 53, pp. 5145–5148, Mar. 1996.

[138] S. Kittaka, K. An, T. Sakakibara, Y. Haga, E. Yamamoto, N. Kimura, Y. Ōnuki, and K. Machida *J. Phys. Soc. Jpn.*, vol. 82, p. 024707, Jan. 2013.

[139] J. R. Kirtley *Rep. Prog. Phys.*, vol. 73, p. 126501, nov 2010.

[140] A. Frinkler, *Scanning SQUID Microscope for Studying Vortex Matter in Type-II Superconductors*. Springer-Verlag Berlin Heidelberg, 2012.

[141] H. Courtois, M. Meschke, J. T. Peltonen, and J. P. Pekola *Phys. Rev. Lett.*, vol. 101, p. 067002, Aug 2008.

[142] J. R. Kirtley, B. Kalisky, J. A. Bert, C. Bell, M. Kim, Y. Hikita, H. Y. Hwang, J. H. Ngai, Y. Segal, F. J. Walker, C. H. Ahn, and K. A. Moler *Phys. Rev. B*, vol. 85, p. 224518, June 2012.

[143] W. Rabaud, *Courants permanents dans des anneaux mésoscopiques connectés*. Thesis, Université Joseph-Fourier - Grenoble I, Nov. 2001.

[144] Y. M. Blanter and M. Buttiker *Phys. Rep.*, vol. 336, no. 1, pp. 1 – 166, 2000.

[145] D. Dew-Hughes *J. Low Temp. Phys.*, vol. 27, no. 9, pp. 713–722, 2001.

[146] G. M. Luke, A. Keren, L. P. Le, W. D. Wu, Y. J. Uemura, D. A. Bonn, L. Taillefer, and J. D. Garrett *Phys. Rev. Lett.*, vol. 71, pp. 1466–1469, Aug. 1993.

[147] O. V. Lounasmaa and R. D. Parks, *Experimental Principles and Methods Below 1 K*. Academic Press, 1974.

[148] W. A. Bosch, "High Development Leiden (HDL)." `https://hdleiden.home.xs4all.nl/`. Online; accessed 28 May 2018.

[149] C. Veauvy, *Imagerie magnétique par micro-SQUID à basse température*. Thesis, Université Joseph-Fourier - Grenoble I, Jan. 2002.

[150] D. Hykel, *Magnetic imaging of unconventional superconductors by scanning SQUID microscopy*. Thesis, Université de Grenoble, Feb. 2011.

[151] Z.-S. Wang, *The superconducting properties research of iron based-122 by transport and scanning micro-squid measurements*. Thesis, Université de Grenoble; Chinese Academy of Sciences, May 2012.

[152] S. H. Pan, *Piezo-electric motor*. International Bureau, World Intellectual Property Organization, 1993.

[153] Y. Ando and L. Fu *Annu. Rev. Condens. Matter Phys.*, vol. 6, no. 1, pp. 361–381, 2015.

[154] M. Sato and S. Fujimoto *J. Phys. Soc. Jpn*, vol. 85, p. 027001, 2016.

[155] M. Sato and Y. Ando *Rep. Progr. Phys.*, vol. 80, no. 7, p. 076501, 2017.

[156] Amit and Y. Singh *Phys. Rev. B*, vol. 97, p. 054515, Feb 2018.

[157] M. V. Salis, P. Rodière, H. Leng, Y. K. Huang, and A. de Visser *J. Phys. Condens. Matter*, vol. 30, p. 505602, Nov. 2018.

[158] S. Teknowijoyo, N. H. Jo, M. S. Scheurer, M. A. Tanatar, K. Cho, S. L. Bud'ko, P. P. Orth, P. C. Canfield, and R. Prozorov *Phys. Rev. B*, vol. 98, p. 024508, July 2018.

[159] Y. Liu, J.-Z. Zhao, L. Yu, C.-T. Lin, A.-J. Liang, C. Hu, Y. Ding, Y. Xu, S.-L. He, L. Zhao, G.-D. Liu, X.-L. Dong, J. Zhang, C.-T. Chen, Z.-Y. Xu, H.-M. Weng, X. Dai, Z. Fang, and X.-J. Zhou *Chin. Phys. Lett.*, vol. 32, p. 067303, June 2015.

[160] O. J. Clark, M. J. Neat, K. Okawa, L. Bawden, I. Marković, F. Mazzola, J. Feng, V. Sunko, J. M. Riley, W. Meevasana, J. Fujii, I. Vobornik, T. K. Kim, M. Hoesch, T. Sasagawa, P. Wahl, M. S. Bahramy, and P. D. C. King *Phys. Rev. Lett.*, vol. 120, p. 156401, Apr 2018.

[161] M. S. Bahramy, O. J. Clark, B.-J. Yang, J. Feng, L. Bawden, J. M. Riley, I. Markovic, F. Mazzola, V. Sunko, D. Biswas, S. P. Cooil, M. Jorge, J. W. Wells, M. Leandersson, T. Balasubramanian, J. Fujii, I. Vobornik, J. E. Rault, T. K. Kim, M. Hoesch, K. Okawa, M. Asakawa, T. Sasagawa, T. Eknapakul, W. Meevasana, and P. D. C. King *Nature Mat.*, vol. 17, p. 21, 2018.

[162] A. A. Soluyanov, D. Gresch, Z. Wang, Q. Wu, M. Troyer, X. Dai, and B. A. Bernevig *Nature*, vol. 257, p. 495, 2015.

[163] S. Das, Amit, A. Sirohi, L. Yadav, S. Gayen, Y. Singh, and G. Sheet *Phys. Rev. B*, vol. 97, p. 014523, Jan 2018.

[164] A. Sirohi, S. Das, P. Adhikary, R. R. Chowdhury, A. Vashist, Y. Singh, S. Gayen, T. Das, and G. Sheet *J. Phys. Condens. Matter*, vol. 31, p. 085701, jan 2019.

[165] T. Le, L. Yin, Z. Feng, Q. Huang, L. Che, J. Li, Y. Shi, and X. Lu *Phys. Rev. B*, vol. 99, p. 180504, May 2019.

[166] T. Kurumaji, S. Seki, S. Ishiwata, H. Murakawa, Y. Kaneko, and Y. Tokura *Phys. Rev. B*, vol. 87, 01 2013.

[167] A. E. Dunsworth *J. Low Temp. Phys.*, vol. 19, pp. 51–57, Apr. 1975.

[168] H.-J. Noh, J. Jeong, E.-J. Cho, K. Kim, B. I. Min, and B.-G. Park *Phys. Rev. Lett.*, vol. 119, p. 016401, Jul 2017.

[169] J. Guggenheim, F. Hulliger, and J. Müller *Helv. Phys. Acta*, vol. 34, no. V, p. 408, 1961.

[170] H. Leng, C. Paulsen, Y. K. Huang, and A. de Visser *Phys. Rev. B*, vol. 96, Dec. 2017.

[171] J. D. Livingston and W. DeSorbo, *21. The intermediate state in type-I superconductors.* R. D. Parks, *Superconductivity*, Marcel Bekker, 1969.

[172] H. Leng, J.-C. Orain, A. Amato, Y. Huang, and A. de Visser *Phys. Rev. B*, vol. 100, p. 224501, 2019.

[173] F. Fei, X. Bo, R. Wang, B. Wu, J. Jiang, D. Fu, M. Gao, H. Zheng, Y. Chen, X. Wang, H. Bu, F. Song, X. Wan, B. Wang, and G. Wang *Phys. Rev. B*, vol. 96, p. 041201, July 2017.

[174] P. Garcia-Campos, Y. K. Huang, A. de, and K. Hasselbach *Phys. Rev. B*, vol. 103, p. 104510, Mar 2021.

[175] R. P. Huebener, *Magnetic flux structures in superconductors*. Springer-Verlag Berlin Heidelberg, 1979.

[176] L. Lyard, T. Klein, J. Marcus, R. Brusetti, C. Marcenat, M. Konczykowski, V. Mosser, K. H. Kim, B. W. Kang, H. S. Lee, and S. I. Lee *Phys. Rev. B*, vol. 70, p. 180504, Nov 2004.

[177] D. Shoenberg, *Superconductivity*. Cambridge, 1952.

[178] L. Landau *J. Phys. U.S.S.R.*, vol. 7, no. 99, 1943.

[179] G. Lasher *Phys. Rev.*, vol. 154, pp. 345–348, Feb 1967.

[180] E. M. Lifschitz and Y. V. Sharvin *Dokl. Akad. Nauk SSSR*, vol. 79, p. 783, 1951. through ref. [252].

[181] A. Hubert *Phys. Stat. Sol. B*, vol. 24, no. 2, pp. 669–682, 1967.

[182] T. E. Faber and D. Shoenberg *Proc. R. Soc. Lond. A*, vol. 248, pp. 460–481, Dec. 1958.

[183] B. M. Balashova and I. V. Sharvin *J. Exp. Theor. Phys.*, vol. 4, February 1957.

[184] W. Desorbo and W. Healy *Cryogenics*, vol. 4, p. 324, Oct 1964.

[185] A. Meshkovsky and A. Shalnikov *Zh. Eksp. i Teor. Fiz.*, vol. 11, no. 1, 1947.

[186] D. J. Hykel, Z. S. Wang, P. Castellazzi, T. Crozes, G. Shaw, K. Schuster, and K. Hasselbach *J. Low Temp. Phys.*, vol. 175, pp. 861–867, 2014.

[187] J. R. Clem, R. Prozorov, and R. J. Wijngaarden *Phys. Rev. B*, vol. 88, p. 104504, Sep 2013.

[188] A. L. Schawlow and G. E. Devlin *Phys. Rev.*, vol. 110, pp. 1011–1016, June 1958.

[189] F. Haenssler and L. Rienderer *Helv. Phys. Acta*, vol. 38, no. 448, 1965.

[190] J. Allen and R. Lerski, *Observation of Landau-Type Branching in the Intermediate State*. Timmerhaus K.D., O'Sullivan W.J. and Hammel E.F. *Low Temperature Physics-LT 13*, Springer, Boston, MA, 1974.

[191] R. N. Goren and M. Tinkham *J. Low Temp. Phys.*, vol. 5, pp. 465–494, Oct 1971.

[192] A. Fortini and E. Paumier *Phys. Rev. B*, vol. 5, pp. 1850–1858, Mar 1972.

[193] A. Aharoni *J. Appl. Phys.*, vol. 83, no. 6, pp. 3432–3434, 1998.

[194] V. G. Kogan *Phys. Rev. B*, vol. 68, p. 104511, 2003.

[195] G. Carneiro and E. H. Brandt *Phys. Rev. B*, vol. 61, pp. 6370–6376, Mar. 2000.

[196] D. E. Farrel, R. P. Huebener, and R. T. Kampwirth *J. Low Temp. Phys.*, vol. 19, pp. 99–112, Apr 1975.

[197] A. Bodmer, U. Essmann, and H. Träuble *Phys. Stat. Sol. A*, vol. 13, pp. 471 – 481, 10 1972.

[198] R. Prozorov, R. W. Giannetta, A. A. Polyanskii, and G. K. Perkins *Phys. Rev. B*, vol. 72, p. 212508, Dec 2005.

[199] V. Kozhevnikov, R. J. Wijngaarden, J. de Wit, and C. Van Haesendonck *Phys. Rev. B*, vol. 89, p. 100503, Mar 2014.

[200] R. F. Broom and E. H. Rhoderick *Proc. Phys. Soc.*, vol. 79, pp. 586–593, mar 1962.

[201] Y. V. Sharvin *J. Exp. Theor. Phys.*, vol. 6, p. 1031, 1958.

[202] Y. V. Sharvin *J. Exp. Theor. Phys.*, vol. 11, p. 216, 1960.

[203] M. V. Salis, Y. K. Huang, and A. de Visser *Phys. Rev. B*, vol. 103, p. 104502, Mar. 2021.

[204] B. Tiwari, R. Goyal, R. Jha, A. Dixit, and V. Awana *Supercond. Sci. Technol.*, vol. 28, p. 055008, 03 2015.

[205] X. Chen, J. G. Guo, C. S. Gong, J. Deng, T. P. Ying, E. J. Cheng, S. Y. Li, and X. L. Chen *J. Phys. Comm.*, vol. 3, p. 095008, Sep 2019.

[206] A. Amann, P. Visani, K. Aupke, A. C. Mota, M. B. Maple, Y. Dalichaouch, P. E. Armstrong, and Z. Fisk *EPL*, vol. 33, pp. 303–308, feb 1996.

[207] G. E. Volovik and M. M. Salomaa *J. Exp. Theor. Phys.*, vol. 61, pp. 986–990, 1985. J. Exp. Theor. Phys. 88, 1656-1663 (May 1985)].

[208] M. Sigrist, T. M. Rice, and K. Ueda *Phys. Rev. Lett.*, vol. 63, pp. 1727–1730, Oct 1989.

[209] M. Sigrist, D. B. Bailey, and R. B. Laughlin *Phys. Rev. Lett.*, vol. 74, pp. 3249–3252, Apr 1995.

[210] G. E. Volovik *Proc. Natl. Acad. Sci. U.S.A.*, vol. 97, no. 6, pp. 2431–2436, 2000.

[211] M. A. Silaev *Phys. Rev. B*, vol. 83, p. 144519, Apr 2011.

[212] M. Ichioka, Y. Matsunaga, and K. Machida *Phys. Rev. B*, vol. 71, p. 172510, May 2005.

[213] J. Goryo *International Journal of Modern Physics B*, vol. 15, pp. 1617–1620, May 2001.

[214] C. C. Tsuei, J. R. Kirtley, C. C. Chi, L. S. Yu-Jahnes, A. Gupta, T. Shaw, J. Z. Sun, and M. B. Ketchen *Phys. Rev. Lett.*, vol. 73, pp. 593–596, Jul 1994.

[215] J. R. Kirtley, C. C. Tsuei, M. Rupp, J. Z. Sun, L. S. Yu-Jahnes, A. Gupta, M. B. Ketchen, K. A. Moler, and M. Bhushan *Phys. Rev. Lett.*, vol. 76, pp. 1336–1339, Feb 1996.

[216] D. Jaccard, J. Flouquet, P. Lejay, and J. L. Tholence *J. Appl. Phys.*, vol. 57, no. 8, pp. 3082–3083, 1985.

[217] T. T. M. Palstra, P. H. Kes, J. A. Mydosh, A. de Visser, J. J. M. Franse, and A. Menovsky *Phys. Rev. B*, vol. 30, pp. 2986–2988, Sep 1984.

[218] G. Bruls *Physica B Condens. Matter*, vol. 206-207, pp. 580–582, Feb 1995.

[219] B. Shivaram, J. Gannon, and D. Hinks *Physica B Condens. Matter*, vol. 163, no. 1, pp. 141–143, 1990.

[220] E. H. Brandt *Physica C: supercond.*, vol. 369, no. 1, pp. 10–20, 2002.

[221] E. A. Schuberth, S. Schöttl, K. Flachbart, and T. Sasaki *J. Magn. Magn. Mater.*, vol. 226-230, pp. 372–373, May 2001.

[222] P. J. C. Signore, B. Andraka, M. W. Meisel, S. E. Brown, Z. Fisk, A. L. Giorgi, J. L. Smith, F. Gross-Alltag, E. A. Schuberth, and A. A. Menovsky *Phys. Rev. B*, vol. 52, no. 6, pp. 4446–4461, 1995.

[223] F. Gross, B. Chandrasekhar, K. Andres, U. Rauchschwalbe, E. Bucher, and B. Lüth *Physica C: supercond.*, vol. 153-155, pp. 439–440, June 1988.

[224] F. Gross-Alltag, B. S. Chandrasekhar, D. Einzel, P. J. Hirschfeld, and K. Andres *Zeitschrift für Physik B Condensed Matter*, vol. 82, pp. 243–255, June 1991.

[225] S. Schöttl, E. Schuberth, K. Flachbart, J. Kycia, and A. Menovsky *Physica B Condens. Matter*, vol. 259-261, pp. 672–673, 1999.

[226] S. Brown, H. Li, M. Meisel, J. Smith, A. Giorgi, and J. Thompson *Physica B: Condensed Matter*, vol. 165-166, pp. 377–378, 1990. Proceedings of the 19th International Conference on Low Temperature Physics.

[227] J. J. Gannon, B. S. Shivaram, and D. G. Hinks *EPL*, vol. 13, pp. 459–464, Nov 1990.

[228] W. J. Gannon, W. P. Halperin, C. Rastovski, K. J. Schlesinger, J. Hlevyack, M. R. Eskildsen, A. B. Vorontsov, J. Gavilano, U. Gasser, and G. Nagy *New Journal of Physics*, vol. 17, p. 023041, feb 2015.

[229] C. Broholm, G. Aeppli, R. N. Kleiman, D. R. Harshman, D. J. Bishop, E. Bucher, D. L. Williams, E. J. Ansaldo, and R. H. Heffner *Phys. Rev. Lett.*, vol. 65, pp. 2062–2065, Oct 1990.

[230] A. Yaouanc, P. Dalmas de Réotier, A. Huxley, J. Flouquet, P. Bonville, P. C. M. Gubbens, and A. M. Mulders *Journal of Physics: Condensed Matter*, vol. 10, pp. 9791–9798, nov 1998.

[231] R. N. Kleiman, C. Broholm, G. Aeppli, E. Bucher, N. Stücheli, D. J. Bishop, K. N. Clausen, K. Mortensen, J. S. Pedersen, and B. Howard *Phys. Rev. Lett.*, vol. 69, pp. 3120–3123, Nov 1992.

[232] J. R. Kirtley, V. G. Kogan, J. R. Clem, and K. A. Moler *Phys. Rev. B*, vol. 59, pp. 4343–4348, Feb. 1999.

[233] J. D. Strand, D. J. van Harlingen, J. B. Kycia, and W. P. Halperin *Phys. Rev. Lett.*, vol. 103, p. 197002, Nov 2009.

[234] W. J. Skocpol, M. R. Beasley, and M. Tinkham *J. Appl. Phys.*, vol. 45, no. 9, pp. 4054–4066, 1974.

[235] R. F. Voss *J. Low Temp. Phys.*, vol. 42, pp. 151 – 163, 1981.

[236] S. K. H. Lam and D. L. Tilbrook *Appl. Phys. Lett.*, vol. 82, no. 7, pp. 1078–1080, 2003.

[237] A. G. P. Troeman, H. Derking, B. Borger, J. Pleikies, D. Veldhuis, and H. Hilgenkamp *Nano Lett.*, vol. 7, no. 7, pp. 2152–2156, 2007.

[238] L. Hao, J. C. Macfarlane, J. C. Gallop, D. Cox, J. Beyer, D. Drung, and T. Schurig *Appl. Phys. Lett.*, vol. 92, no. 19, p. 192507, 2008.

[239] R. Russo, E. Esposito, C. Granata, A. Vettoliere, M. Russo, C. Cannas, D. Peddis, and D. Fiorani *Phys. Procedia*, vol. 36, pp. 293–299, 2012.

[240] C. Granata and A. Vettoliere *Phys. Rep.*, vol. 614, pp. 1–69, Feb 2016.

[241] S. Biswas, C. B. Winkelmann, H. Courtois, T. Dauxois, H. Biswas, and A. K. Gupta *Phys. Rev. B*, vol. 101, p. 024501, Jan 2020.

[242] D. Hazra, J. R. Kirtley, and K. Hasselbach *Appl. Phys. Lett.*, vol. 103, p. 093109, Aug. 2013.

[243] K. Hasselbach, D. Mailly, and J. R. Kirtley *J. Appl. Phys.*, vol. 91, pp. 4432–4437, Apr. 2002.

[244] N. Kumar, T. Fournier, H. Courtois, C. B. Winkelmann, and A. K. Gupta *Phys. Rev. Lett.*, vol. 114, p. 157003, Apr 2015.

[245] J. Romijn, T. M. Klapwijk, M. J. Renne, and J. E. Mooij *Phys. Rev. B*, vol. 26, pp. 3648–3655, Oct 1982.

[246] API Technologies - Spectrum Control, *Resin Sealed Bolt-in EMI Filters*.

[247] M. D. Maloney, F. de la Cruz, and M. Cardona *Phys. Rev. B*, vol. 5, pp. 3558–3572, May 1972.

[248] E. Harris and R. Laibowitz *IEEE Trans. Magn.*, vol. 13, no. 1, pp. 724–730, 1977.

[249] A. Finkler, Y. Segev, Y. Myasoedov, M. L. Rappaport, L. Ne'eman, D. Vasyukov, E. Zeldov, M. E. Huber, J. Martin, and A. Yacoby *Nano Lett.*, vol. 10, pp. 1046–1049, Feb. 2010.

[250] Y. Shperber, N. Vardi, E. Persky, S. Wissberg, M. E. Huber, and B. Kalisky *Review of Scientific Instruments*, vol. 90, no. 5, p. 053702, 2019.

[251] Magnicon GmbH, *High-performance low-noise dc SQUID sensors*, Mars 2011.

[252] R. D. Parks, *Superconductivity.* Marcel Bekker, 1969.

[253] D. E. McCumber *J. Appl. Phys.*, vol. 39, no. 7, pp. 3113–3118, 1968.

[254] V. J. de Waal, P. Schrijner, and R. Llurba *J. Low Temp. Phys.*, vol. 54, pp. 215–232, Feb. 1984.

[255] F. London *Phys. Rev.*, vol. 74, pp. 562–573, Sep 1948.

[256] L. Onsager *Il Nuovo Cimento (1943-1954)*, vol. 6, pp. 279–287, Mar 1949.

[257] J. Pearl *J. Appl. Phys.*, vol. 37, no. 11, pp. 4139–4141, 1966.

[258] J. R. Kirtley, C. C. Tsuei, K. A. Moler, V. G. Kogan, J. R. Clem, and A. J. Turberfield *Appl. Phys. Lett.*, vol. 74, no. 26, pp. 4011–4013, 1999.

[259] H. Kleykamp *Pure and App. Chem.*, vol. 63, no. 10, pp. 1401–1408, 1991.

[260] J. J. Park and D. P. Fickle *J. Res. Natl. Bur. Stand. (U. S.) - A*, vol. 64, pp. 107–117, Jan 1960.

[261] B. A. S. Ross and D. E. Peterson *Bull. Allow Phase Diagr.*, vol. 11, pp. 240–243, 1990.

[262] W. Schneider and C. Laubschat *Physica B+C*, vol. 102, no. 1, pp. 111–113, 1980.

[263] W.-D. Schneider and C. Laubschat *Phys. Rev. B*, vol. 23, pp. 997–1005, Feb 1981.

Appendix A

RCSJ model

SQUIDs are superconducting loops with two Josephson junctions as already presented in sec. 1.2.3. The weakening of the superconductivity in the Josephson junction can be achieved with an insulating layer, a normal metal layer and a constriction of the superconducting layer.

The first two junctions present an intrinsic capacitance due to the geometry of the junction. In addition, these junctions are intrinsically hysteretic, which means that once I is greater than I_c, I has to be reduced to a value much lower than I_c [27]. In order to reduce the hysteresis of the SQUIDs, they are often shunted with a resistor. This is the approach taken in ch. 5. The current-voltage characteristics of such junctions are well-explained by the resistively- and capacitively-shunted junction (RCSJ) model. It assumes point-like junctions, with no spatial dependence.

Within this model a Josephson junction shunted with a capacitance C and a resistance R is described by:

$$C\dot{U} + U/R + I_0 \sin\varphi = I + I_N(t) \tag{A.1}$$

where φ is the phase difference across the junction and $I_N(t)$ is a noise that I'll neglect in the following. Using the phase-voltage relation deduced by Josephson (eq. 1.19), we find:

$$\frac{\Phi_0}{2\pi} C\ddot{\varphi} + \frac{\Phi_0}{2\pi}\frac{1}{R}\dot{\varphi} = I - I_0 \sin\varphi = -\frac{2\pi}{\Phi_0}\frac{\partial U_J}{\partial \varphi} \tag{A.2}$$

where U_J is the so-called titled washboard potential of the Josephson junction.

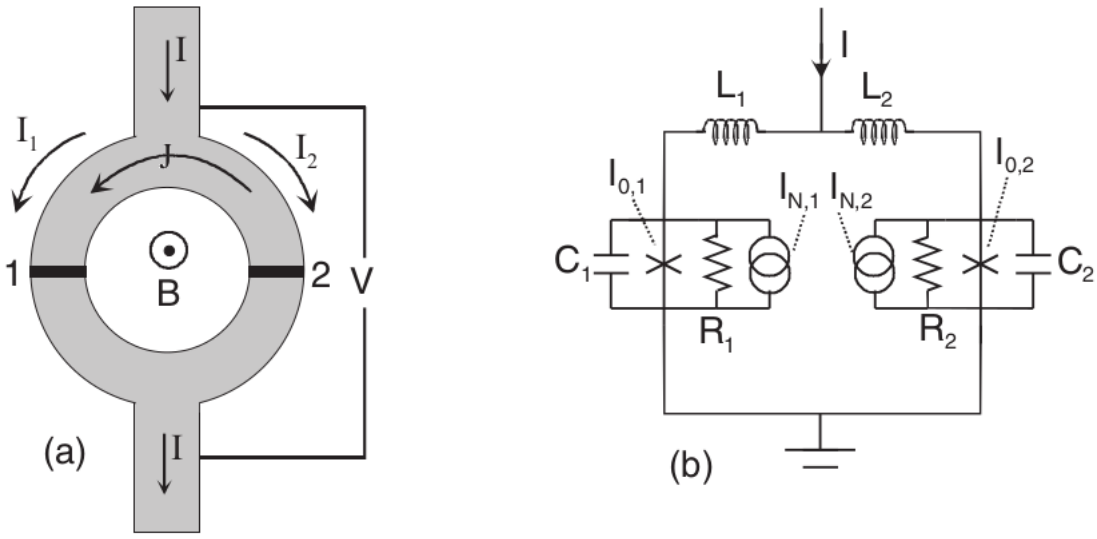

Figure A.1: *In (a), the schema on a SQUID. The input current is I, the voltage difference is V. There are two branches, each has a part of the input current I_k and the screening current J. A magnetic field is applied perpendicular to the SQUID loop. In (b), the electronic schema of a SQUID according to the RCSJ model. Each branch has an inductance L_k, a capacitance C_k, a resistance, R_k, the junction with critical current I_{ck} and a noise source I_{Nk} for completeness. Figure modified from ref. [27].*

A SQUID has two branches as sketched in fig. A.1(a), with an inductance L_k and a RCSJ junction with parameters: φ_k, I_{0k}, R_k and C_k. The schema of the whole SQUID is presented in fig. A.1(b). With an input current I, the dynamics of the phase in each junction are described by:

$$\frac{I}{2} \pm J = I_{0k} \sin \varphi_k + \frac{\Phi_0}{2\pi R_k}\dot{\varphi}_k + \frac{\Phi_0}{2\pi} C_k \ddot{\varphi}_k \tag{A.3}$$

for each of the junctions: $k = 1, 2$. As already presented in sec. 1.2.3, the phases are related by:

$$\varphi_2 - \varphi_1 = \frac{2\pi}{\Phi_0}(\Phi_{ext} + L_1 I_1 - L_2 I_2) = \frac{2\pi}{\Phi_0}\Phi_T \tag{A.4}$$

where $L = L_1 + L_2$, $\Phi_{ext} = B_{ext} \cdot S_{SQUID}$ and Φ_T is the total flux going through the SQUID including the external flux and the circulating current.

We shall introduce the following factors: the average critical current, $I_0 = (I_{01} + I_{02})/2$, (twice) the equivalent resistance $R = 2R_1R_2/(R_1 + R_2)$, (half) the equivalent capacitance

$C = (C_1 + C_2)/2$ and characteristic time $\tau = \Phi_0/2\pi I_0 R$, so that the currents are normalized to I_0, resistances to R, capacitances to C, time to τ and magnetic flux to Φ_0. Adimensionalizing eq. A.3, we obtain:

$$\frac{i}{2} + j = (1 - \alpha_I)\sin\varphi_1 + (1 - \alpha_R)\dot{\varphi}_1 + \beta_c(1 - \alpha_C)\ddot{\varphi}_1 \tag{A.5}$$

$$\frac{i}{2} - j = (1 + \alpha_I)\sin\varphi_2 + (1 + \alpha_R)\dot{\varphi}_2 + \beta_c(1 + \alpha_C)\ddot{\varphi}_2 \tag{A.6}$$

and

$$\varphi_2 - \varphi_1 = 2\pi(\phi_{ext} + \frac{1}{2}\beta_L j - \frac{1}{4}\alpha_L\beta_L i) \tag{A.7}$$

where α_L, α_I, α_R and α_C represent respectively the asymmetry of the inductance, of the junction critical current, of the resistance and of the capacitance, which are defined as $\alpha_L = (L_2 - L_1)/(L_1 + L_2)$, $\alpha_I = (I_{02} - I_{01})/(I_{01} + I_{02})$, $\alpha_R = (R_2 - R_1)/(R_1 + R_2)$ and $\alpha_C = (C_2 - C_1)/(C_1 + C_2)$. Currents I and J are normalized to i and j. The flux Φ_{ext} is normalized to ϕ_{ext}. Two new parameters were introduced: $\beta_c = 2\pi I_0 R^2 C/\Phi_0$ is the Stewart-McCumber parameter [253] and $\beta_L = 2LI_0/\Phi_0$ is the screening parameter (proportional to g in eq. 1.23).

The static solution of the SQUID with negligible inductance gives the already known eq. 1.24:

$$I_c(\Phi_{ext}) = 2I_0\left|\cos\pi\frac{\Phi_{ext}}{\Phi_0}\right| \tag{A.8}$$

In the case of non negligible inductance, the modulation is reduced as showed in fig. 1.7. At $\beta_L = 1$, the modulation $\Delta I_c/2I_{c0}$ modulates only 50%, for $\beta_L \gg 1$, the modulation decreases as $1/\beta_L$ [27]. For low β_C values, this models show no hysteresis in the I-V characteristics, however, for larger values ($\beta_C > 0.8$) small hysteresis is present, which depends on β_L and ϕ_{ext} [254].

The scanning SQUID

Here, I will briefly analyze the scanning SQUID modulation in terms of the RCSJ model in order to estimate the asymmetries and the inductance. The Josephson junctions of the

SQUIDs consists of constrictions in the superconductor, therefore, for their description we will consider that they have no capacitance ($C_1 = C_2 = 0$). The lithography of the SQUIDs is well controlled thus I assume that the junctions of the same SQUID are reproducible and with no asymmetry of the critical currents ($\alpha_I = 0$). Furthermore, the junction of Al SQUIDs are deposed directly over the Si wafer, thus, the shunting resistance (in parallel to the junction) is large enough to not consider the resistive term ($R_1 = R_2 \to \infty$). After this three assumptions, the system of equations coincides to the static case:

$$\frac{i}{2} + j = (1 - a_I)\sin\varphi_1 \tag{A.9}$$

$$\frac{i}{2} - j = (1 + a_I)\sin\varphi_2 \tag{A.10}$$

$$\varphi_2 - \varphi_1 = 2\pi(\phi_{ext} + \frac{1}{2}\beta_L j - \frac{1}{4}\alpha_L\beta_L i) \tag{A.11}$$

thus, cleaning the currents the system becomes:

$$i = \sin\varphi_1 + \sin\varphi_2 - a_I(\sin\varphi_1 - \sin\varphi_2) \tag{A.12}$$

$$j = \frac{1}{2}(\sin\varphi_1 - \sin\varphi_2) - \frac{1}{2}a_I(\sin\varphi_1 + \sin\varphi_2) \tag{A.13}$$

$$\varphi_2 - \varphi_1 = 2\pi(\phi_{ext} + \frac{1}{2}\beta_L j - \frac{1}{4}\alpha_L\beta_L i) \tag{A.14}$$

Now, we shall resolve the phase equation for every value of flux, and from the possible solutions (φ_1, φ_2), find the ones that maximizes the current: the critical current. As a free parameters for the fitting we have β_L and α_L.

The parameters β_L and α_L describe the reduction of modulation (ΔI_c) and the tilt of the arc respectively. For the scanning SQUIDs, $\beta_L = 1.2$ and $a_L = 0.46$ describe well the modulation. The curve of the RCSJ model with these parameters is presented in fig. A.2 along with an experimental modulation curve. The effective inductance of the SQUID is $L = 35$ pH, with $L_1 = 9.5$ pH and $L_2 = 25.5$ pH. These inductances include the kinetic and geometrical contributions. The RCSJ model allows us to fit the modultion curves of the micro-SQUIDs, however, it does not take into account the physics in the microbridges [243].

Furthermore, we can deduce that changing permuting the injection and ground lead can be described by permutation of junctions 1 and 2. This causes that the modulation arcs

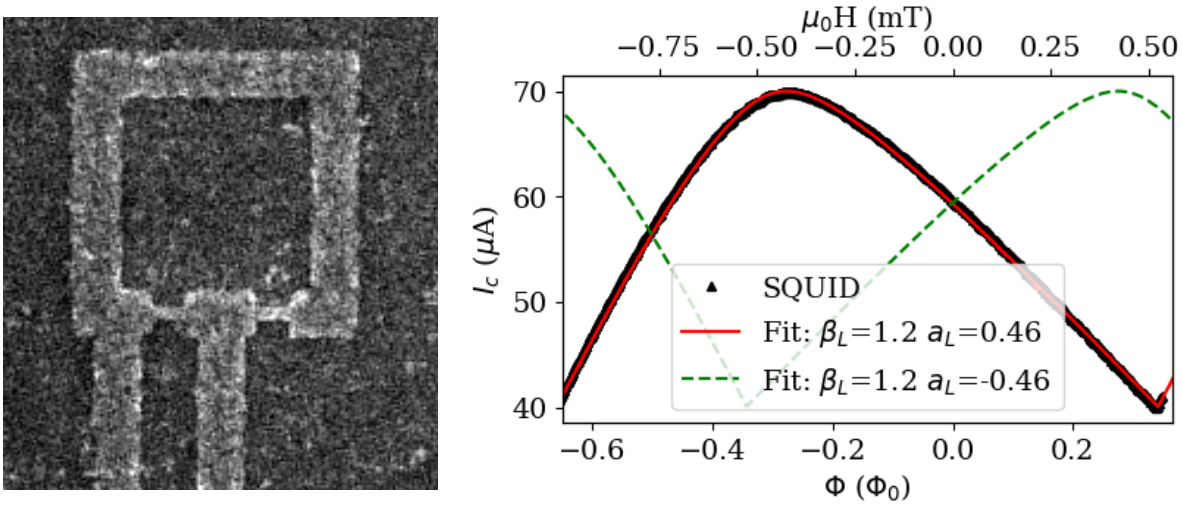

Figure A.2: *On the left, the scanning SQUID made of aluminium. The inner square is 1 μm^2, the width of the current lines are 200 nm and junctions are 200 nm long and 50 nm width. On the right the $I_c(\Phi)$ modulation arcs of the previous SQUID. In black, the experimental $I_c(\Phi)$ curve. Top axis is the corresponding applied field and bottom axis to the magnetic flux ($\Phi = \mu_0 H S_{eff}$, where S_{eff} is the effective SQUID loop size). The red line represents the modulation curve of a SQUID according to the RCSJ model with the following parameters: $I_0 = 35\ \mu A$, $\beta_L = 1.2$, $a_L = 0.46$, $a_I = C_1 = C_2 = 0$, $R_1 = R_2 \to \infty$.*

tilt to the other side. At $H = 0$, the solution of eqs. A.12 does not depend on the labeling, because the flux going through the loop is also zero. Therefore, the modulation arcs of both current injection possibilities must cross at $H = 0$. This means that if we have a field offset due to the calibration of the coil or due to other field such as the Earth one, the crossing of modulations won't happen at the $H = 0$ but shifted to the field offset. This allows us to find the zero field. This is represented in fig. A.2. The green curve corresponds to the same SQUID but with permuted current injection: it is tilted to the other side and it crosses the red curve in $H = 0$. For this reason, SQUID calibration needs of permuting the injection and ground leads.

Appendix B

Translation: I_c to H

The critical current of the SQUID is periodic with the magnetic flux going through the loop (see sec. 1.2.3). As I already mentioned, for a measured I_c multiple values of flux are possible, therefore, it is essential knowing in which modulation arc and in which side of the arc we are. During my thesis I analyzed the field distribution of two samples: UPt_3 and $PdTe_2$. The study of the first one was carried out at low fields and the measured fields are of the order of 0.1 mT while the images of $PdTe_2$ have fields of the order of 5 mT. This difference of fields leads to some differences in the setup and in the data analysis.

UPt_3

For the measurement of this compound we have used SQUIDs of 1 μm^2 of inner loop. The $I_c(B)$ modulation has a periodicity of 1.5 mT, which corresponds to an effective area around 1.3 μm^2. Compared to the period, the usual field variations of the measured data ($\sim$ 0.1 mT) are small enough to consider that it will happen in a single side (branch) of a single arc (see fig. B.1). In this figure I represent the critical current measurement of fig. 4.9 left and the calibration curve for this scan. This curve is the modulation of critical current of the SQUID when is not affected by the superconductivity of the sample ($T_{sample} > T_c$). As we know that we are close to zero field, we are sure in which arc and branch we are working: the thick line represents the range of critical currents of the scan. This line falls in a single branch of the arc, around zero field. A 4th order polynomial fit, $B(Ic)$, is locally calculated

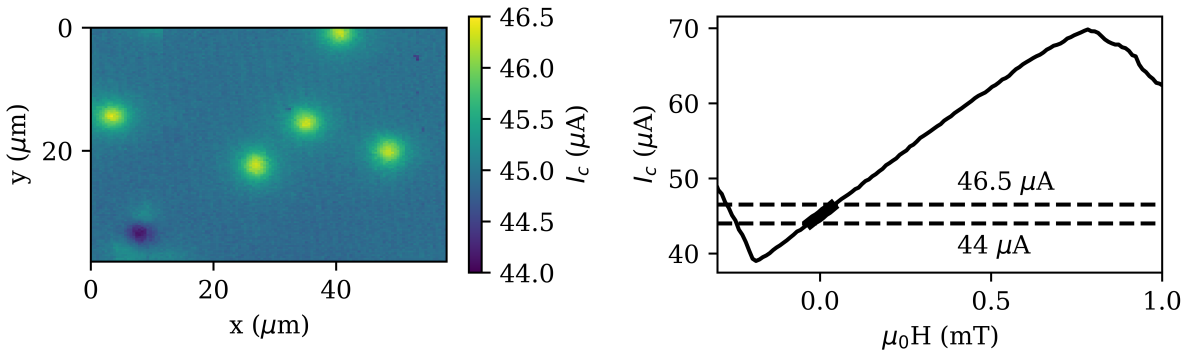

Figure B.1: *On the left, the critical current image of a UPt_3 measurement at 325 mK after ∼5 μT field cooling. It the same data than in fig. 4.9 left. On the right, a part of the modulation arc of the SQUID when non affected by the superconductivity of the sample. The thick line is the critical current range of the scan presented in left (the maximum and minimum of the color bar of this scan are marked with dashed lines).*

in order to translate the whole scan. This method can be used because we are sure that the magnetic field of the scan does not pass through insensitive points (see fig. 2.3).

Magnetization measurements

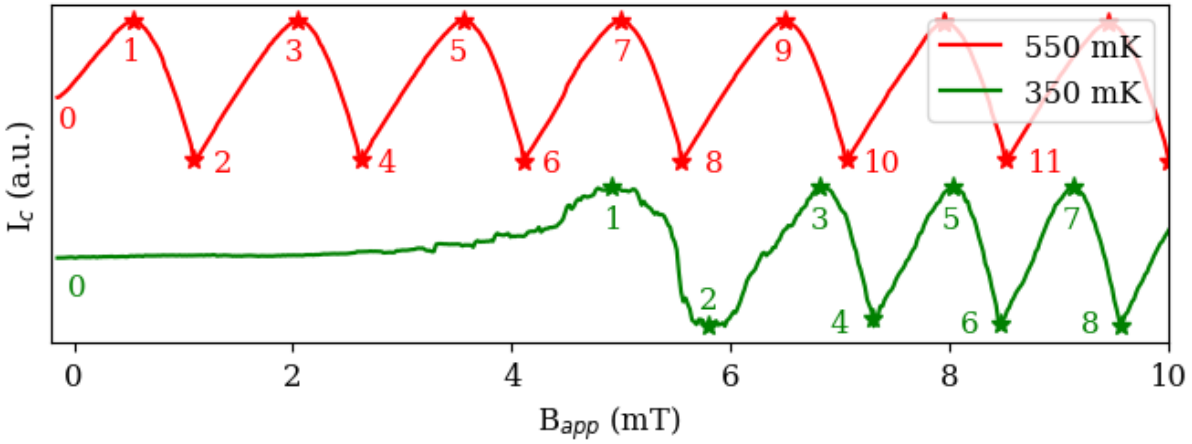

Figure B.2: *Translation one magnetization curve of UPt_3. In red the calibration curve and in blue the magnetization one. The insensitive points of respective curves are marked with stars and are labeled according to the correspondence between the curves.*

Magnetization measurements are sweeps of magnetic field that usually cross several modulation arcs (see fig. B.2). When in the SQUID response we can clearly identify the insensitive points (marked stars), we may be able to translate the SQUID critical current to field.

In the case of UPt_3, the $I_c(H)$ curves are quite smooth (not large jumps) and we can detect the insensitive points. In fig. B.2, I have marked the insensitive points as stars for the calibration curve (in red) and for the magnetization one (in blue). We need to identify the initial point and know in what side of what modulation arc it is. In the curve presented in the figure (virgin magnetization curve at 350 mK) the initial point is around zero (because it is measured after ZFC). In order to translate the curve, we only have to interpolate the magnetization curve between insensitive points of the calibration one, making the correspondence between the insensitive points (range of values between insensitive points 1 and 2 corresponds to the calibration and to the magnetization curve). For this reason, the insensitive point 1 in the calibration curve at $\mu_0 H = 0.55$ mT corresponds to the insensitive point 1 of the magnetization curve at $\mu_0 H = 5$ mT: $B(5) = 0.55$ mT. To convert it to magnetization we just have make the subtraction: $\mu_0 M = B - \mu_0 H = -4.45$ mT. In the case of continuing sweeping (up or down), the new initial point would correspond to the latest value of the precedent sweep.

Otherwise, if the $I_c(H)$ curves are not smooth, like those of $PdTe_2$, the identification of insensitive points may not be evident and the translation may not be possible.

$PdTe_2$

$PdTe_2$ fields are much greater than UPt_3, therefore it's natural to use a smaller SQUID. However the smallest available scanning SQUID is 0.25 μm^2 of inner loop. Its periodicity is about 4 times the one of the 1 μm^2 SQUID: 6.2 mT, which corresponds to an effective area around 0.33 μm^2.

In fig. B.3, I present the critical current scan of this compound corresponding to fig. 3.5(a),

the calibration curve of this scan and the $I_c \rightarrow H$ translation of one line of the scan. We are sure that the blue part of fig. B.3 top left is $B = 0$ (Meissner effect), therefore, we know in which arc and in which branch we are working. In fig. B.3 top right, the thick line in the calibration curve represents the range of critical currents of the scan. Now we observe that they do not fall in a single branch, but they pass through an insensitive point. For making possible the translation we have to notice the insensitive point and fit $B(Ic)$ for each branch around the insensitive point. Like this we know that each branch of each arc has a possible field translation. As example, this method is applied to the line $y = 6.4$ μm of the scan, which is represented for the branch 0 (around the zero field) and branch 1 (next branch) in the bottom of fig. B.3. The translation difficulty here is to choose the modulation branch for a given pixel. In the example presented in the figure, we are sure that for $x < 30$ μm the field is around zero, i.e. the branch 0. In the tip of the structure, we go through the maxima of the modulation arc: we change to branch 1. Because of coherence of the scan, the field for $x > 45$ μm must come back to zero, i.e. the branch 0. The chosen field for each pixel is marked by the dotted red line, forming a more usual field distribution.

In order to translate the data using this method we have to know at least the approximated field value of a pixel, that constitutes the starting point for the coherent translation. For this reason we have to take into account the magnetic history of the sample for each scan. Therefore we know what critical current value corresponds to the superconducting state and which are superconducting/IS domains, which will shrink/grow respectively with increasing the field. It happens that the field value may not vary much around the insensitive point, in this case, we may not be able to translate this measurement.

In the case of the superconducting islands inside the IS domains (see fig. 3.5.(b)), we detected them because the change of the slope of the critical current between the outside and the inside of the dip happens smoothly and far from the insensitive points.

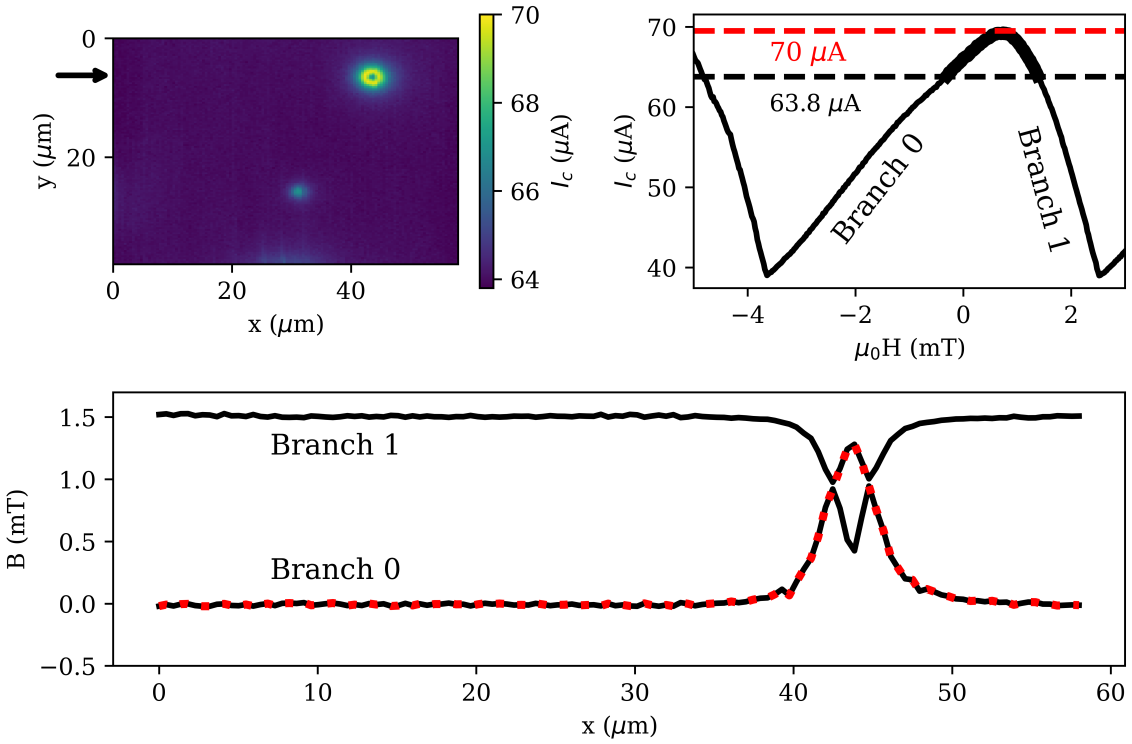

Figure B.3: *In the top left, the critical current image of a $PdTe_2$ measurement at 300 mK and 1 mT after zero field cooling. It is the same data than in fig. 3.5.(a). In the top right, a part of the calibration arc of the SQUID when non affected by the superconductivity of the sample. The thick line is the critical currents of the scan presented in top left (the maximum and minimum of the colorbar are marked with dashed lines). We notice that we go through the maxima, marked with the red dashed line. In the bottom, the field profile for branches 0 and 1 of the line $y = 6.4$ μm of the scan in the top left (line marked with an arrow). The field translation of the profile is marked with a dotted red line.*

Appendix C

Vortex: field distribution

The field distribution of a vortex at the surface is a question of matter for our studies. The description comes from combining the solution of F. London for a vortex [255] and the concept of core of quantum vortex by Onsager [256]. The supercurrents circulate around the core of the vortex, which is in the normal state. The core has a size of the superconducting coherence length, ξ and far from the core the supercurrents decay exponentially with the penetration depth, λ. The field in the z-axis is described by

$$B_z(r) = \frac{\Phi_0}{2\pi\lambda^2} K_0\left(\frac{r}{\lambda}\right) \tag{C.1}$$

where $K_0(x)$ is th zeorth-order modified Bessel function [23]. At small distances from the core, the field diverges logarithmic however in reality the field at the core is approximately given by $B(0) \approx \Phi_0 \log \kappa / 2\pi\lambda^2$ where $\kappa = \lambda/\xi$. Far from the core, $B(r) \propto \sqrt{\lambda/r}\exp(r/\lambda)$.

The materials we study usually have $\lambda \gg \xi$, therefore the core is never observed with magnetic measurements. Furthermore, the study of this structures happens at a given scanning height z above the surface, so spreading due to the scanning height must be also taken into account. I will present the two models that are often presented in vortex analysis: magnetic monopole and the Pearl's description.

The first description consists of a magnetic monopole placed at a certain distance below the surface. This distance is usually taken as the penetration depth resulting in:

$$B_z(r) = \frac{\Phi_0}{2\pi} \frac{z+\lambda}{(r^2 + (z+\lambda)^2)^{3/2}} \tag{C.2}$$

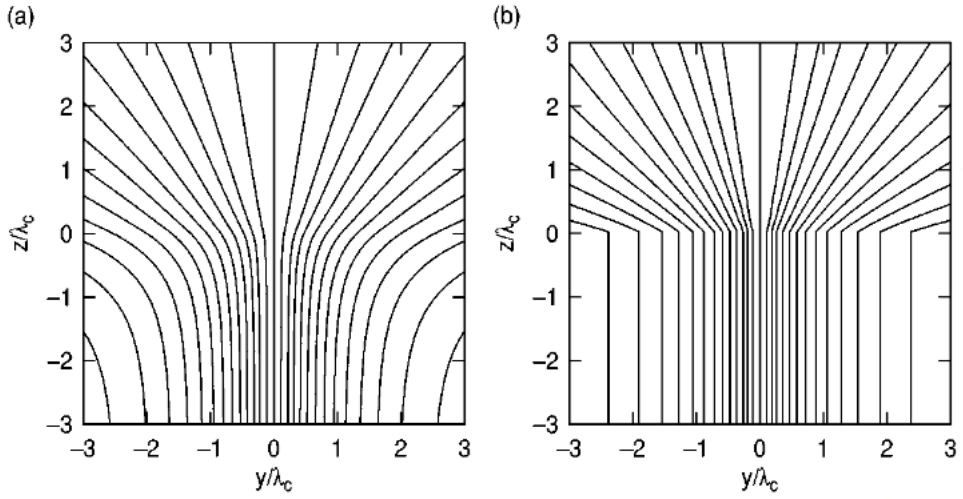

Figure C.1: *In (a) the field distribution of a vortex considering the spreading of magnetic field below the surface and in (b) the field distribution but without considering the spreading. Figure modified from ref. [232].*

where r is the radius centered at the vortex core. However, some authors remark that the near-field distribution of superconducting vortices may be better described by a monopole depth of 1.27λ [195]:

$$B_z(r) = \frac{\Phi_0}{2\pi} \frac{z + 1.27\lambda}{(r^2 + (z + 1.27\lambda)^2)^{3/2}} \tag{C.3}$$

Pearl [257] described the magnetic field of a vortex for an isotropic material. It was later extended to layered materials by Kirtley *et al.* [258]. Pearl considered that (i) the field distribution well inside of the superconductor was described by the critical field at the core and the supercurrents screening and that (ii) the field well outside of the sample is homogeneous and equal to the applied field. He then deduced the vortex field distribution from Maxwell equations. The model was later improved taking into account the thickness of the sample, d [258]:

$$B_z(r) = \frac{\Phi_0}{(2\pi\lambda)^2} \int d^2\mathbf{k} \exp{(i\mathbf{k}\cdot\mathbf{r})} \frac{e^{-kz}}{\alpha(\alpha + k\coth(\alpha d/2))} \tag{C.4}$$

where $\mathbf{k}$ is the 2D Fourier vector, $\mathbf{r} = (x, y)$ is the 2D space vector, k is the modulus of $\mathbf{k}$ and $\alpha = \sqrt{k^2 + \lambda^{-2}}$.

In addition to the field spreading due to the scanning height, the monopole description and the Pearl model consider that the magnetic field starts spreading below the sample surface (see fig. C.1). Furthermore, the field distribution is further modified by our probe. The field going through the loop of the SQUID is not necessarily homogeneous, but we measure the averaged field going through the SQUID. Therefore, our measurement is a convolution of the real field distribution. This tends to make the vortex larger than they really are but it does not change total flux.

Another important detail is that field distribution of every model is proportional to the flux contained by the vortex. Therefore, the field distribution of a half-Φ_0 structure is given by half of the previous expressions.

Appendix D

Further data of UPt_3

The amount of data gathered is considerable and the translation of critical current to field is not always evident. Here, I present some scans that were not translated to field units. The problem for I_c-B translation is the periodicity of the critical current, which becomes troublesome close to the insensitive points (see sec. 2.1).

D.1 Field distribution at T_{fixed}

I have already introduced the magnetic distribution at low fields, that we can observe again at fig. D.1(a) (300 mK and 5 μT FC), in which some vortices and antivortices are present. In the same cool down, the 3 mT were applied (see fig. D.1(b)), the antivortex that was at (x, y) = (6, 12) is no longer coupled to the vortex in a *dipole* form, but we have a new *dipole* at (x, y) = (46, 15). At higher field (4 mT in fig. D.1(c)), many more structures have entered the scanning range and some are aligned with the latter *dipole*, which seems pinned at the same position. When further applying field, $\mu_0 H_{c1}$ is crossed and the flux easily penetrates the sample (see fig. D.1(d)). Now, the DW is well decorated with flux[1]. The DW is thus revealed at the same position as the *dipole*. This may indicate that the DW is defined when cooled down and the magnetic field only decorates it. Furthermore, vortices sitting at DWs do not seem to be distorted due to chiral currents as could be expected [208].

[1] The critical current goes through the minimal I_c at (x, y) = (43, 36), the light blue region enclosed by the dark blue region corresponds to another modulation arc.

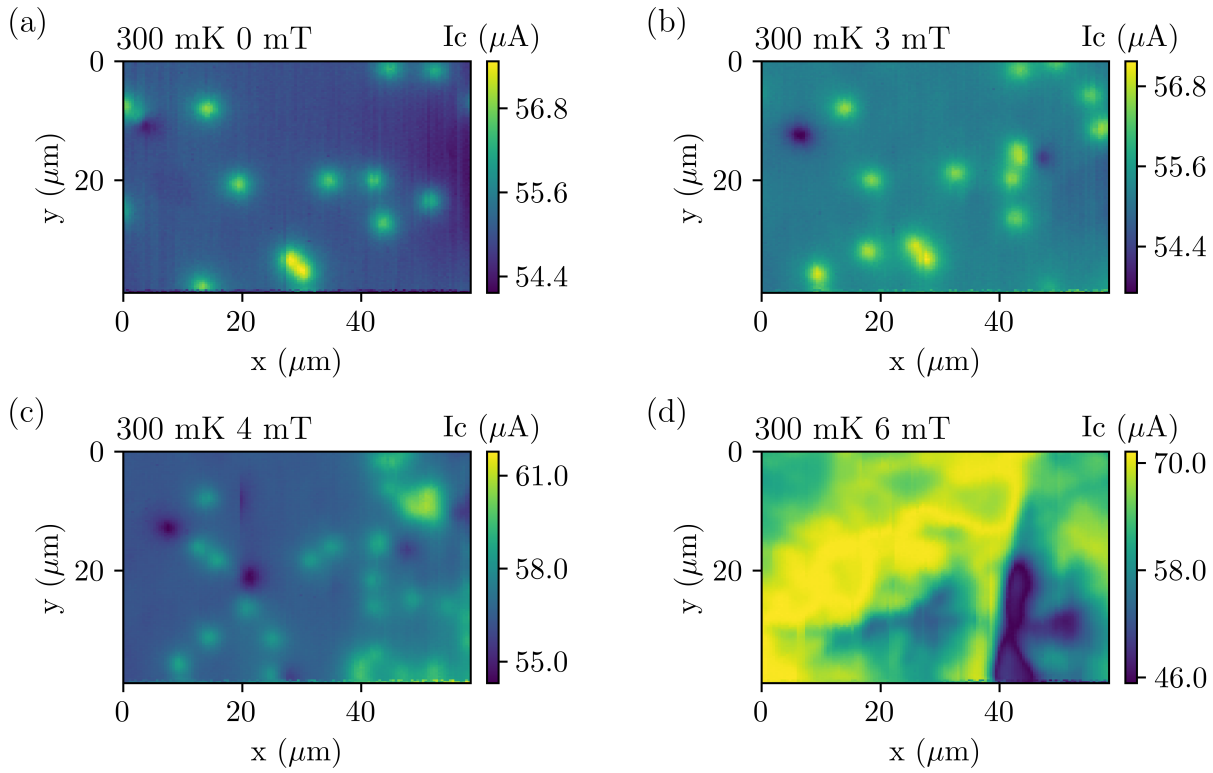

Figure D.1: *Scans (a)-(d) were measured at 300 mK and magnetic fields of 0, 3, 4, 6 mT applied after ZFC.*

D.2 Extraneous magnetic signals

Some scans revealed extraneous magnetic signals above T_c. In fig. D.2(a), a magnetic image of the sample at 550 mK (above T_c). The yellow spot at (19, 23) presents an amplitude of around 100 μT with respect to the background. Images obtained scanning at lower temperatures show that the spot persists at 500 mK (see fig. D.2(b)), but we don't longer see it at 490 mK or lower temperatures (see fig. D.2(c)-(d)). Below 500 mK, the superconductivity is robust enough to overcome the pinning effects. Furthermore, the placement of DWs is unaffected by these impurities (see top right of fig. D.2(d)).

In order to study the quality of the sample surface, it was observed with Scanning Elec-

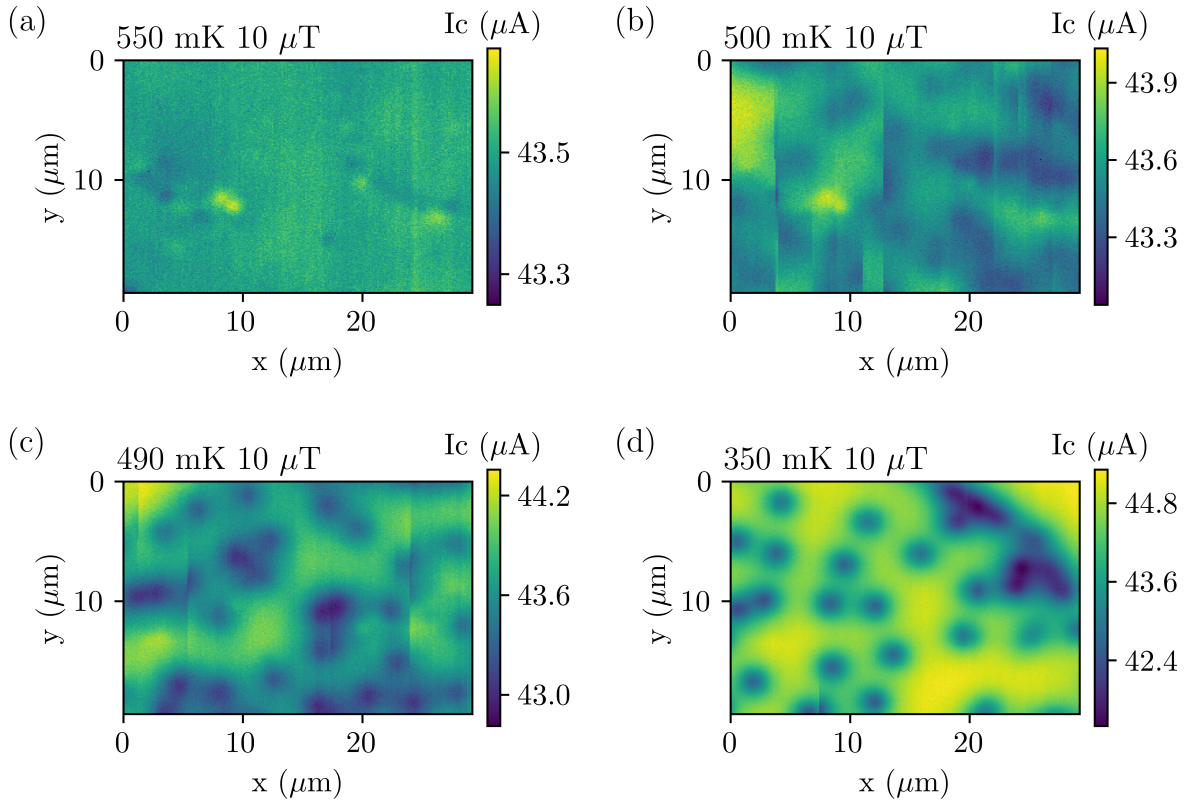

Figure D.2: *Magnetic images after cooling down at low field. The (a) scan (at 550 mK) presents an unexpected magnetic signal. As we lower the temperature, we observe that the effect of this impurity disappears around 490 mK, in scan (c). The DW placement doesn't seem affected by this defect.*

tron Microscope (SEM), revealing needles inserted in the face and crystallographic defaults as shown in fig. D.3 left. This has already been reported in other groups [132]. Further Electron Backscattering diffraction (EBSD) and Energy-dispersive X-ray spectroscopy (EDXS) measurements were carried out on the scanning face. EBSD revealed a poor surface quality, with a lot of scratches and a possible amorphous layer at the surface. These results were likely caused by the polishing of the sample. EDXS confirmed the global composition of the sample, however, the needles inserted on the surface layer presented lower concentrations of platinum (30% of U and 70% of Pt in atomic percentages) [259–261], which strongly suggests the presence of UPt_2 (see fig. D.3 right). However, this compound is paramagnetic

below $\sim$ 10 K [262, 263] and the observed signals are ferromagnetic as they don't follow the applied field. SEM, EBSD and EDXS techniques were performed by S. Pairis in the laboratory.

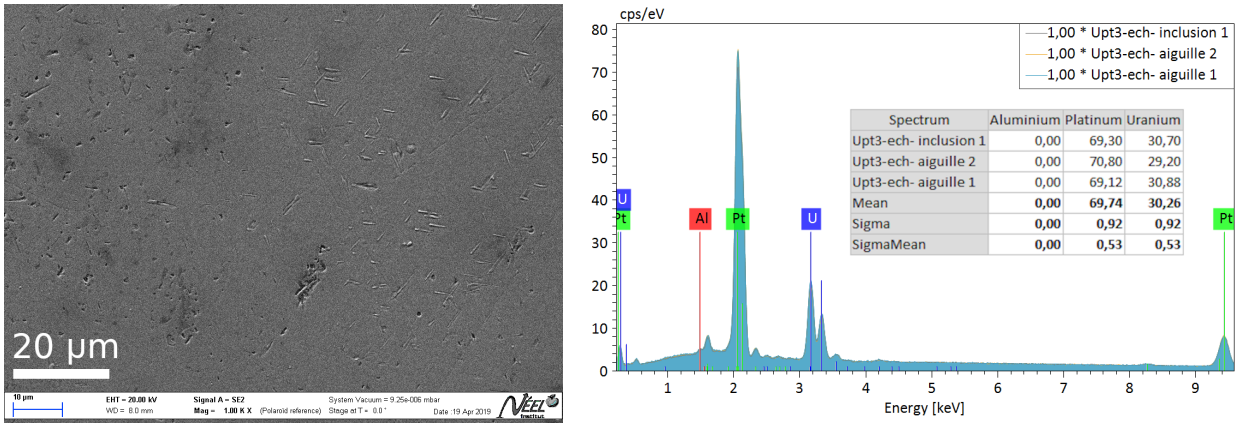

Figure D.3: *In (a), a SEM image of the scanning surface of the sample. Some whiskers are inserted on the ab plane. The EDXS analysis in three crystallographic defaults is presented in (b), with the atomic percentage of each element. Work by S. Pairis.*

In order to verify the quality of the crystal at the scanning face, Laue diffraction was also measured (see fig. D.4). The hexagonal symmetry was well observed, however, spots were doubled, which means that two *ab* planes are present in the sample, slightly tilted with respect to each other. This effect was not observed at the bottom of the sample (unpolished). Thus, it is likely caused by the polishing and reannealing of the sample. Furthermore, polycrystalline rings can be observed in polished and unpolished faces, which cannot be explained by the amorphization induced by polishing. Laue diffraction was performed by P. Lejay in the laboratory.

For any further magnetic work, a crystal of even higher quality should be studied, with no impurities on the surface, with sharper specific heat transitions and a critical temperature closer to 550 mK. D. Aoki prepared us such a crystal, showing perfect Laue pattern, but was lost while polishing.

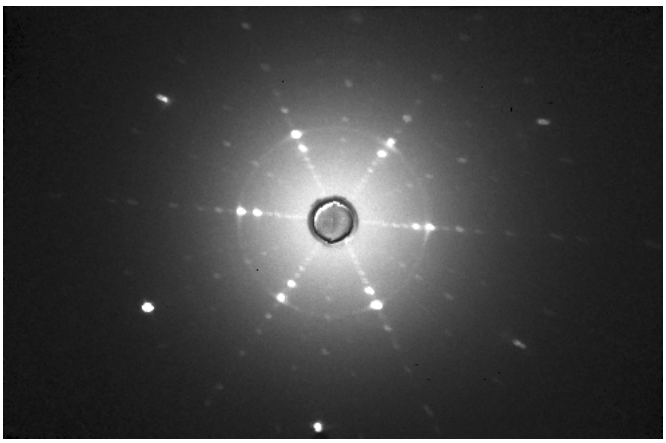

Figure D.4: *Laue diffraction of the polished surface that was imaged. Work by P. Lejay.*